ORNL/TM-2015/633

Fusion Materials Research at Oak Ridge National Laboratory in Fiscal Year 2015

Compiled by:

F.W. Wiffen
Y. Katoh
S. Melton

December 2015

OAK RIDGE NATIONAL LABORATORY
MANAGED BY UT-BATTELLE FOR THE US DEPARTMENT OF ENERGY

Materials Science and Technology Division

FUSION MATERIALS RESEARCH AT OAK RIDGE NATIONAL LABORATORY IN FISCAL YEAR 2015

Compiled by:

F. W. Wiffen
Y. Katoh
S. Melton

Date Published: December 2015

Prepared by
OAK RIDGE NATIONAL LABORATORY
Oak Ridge, TN 37831-6283
managed by
UT-BATTELLE, LLC
for the
US DEPARTMENT OF ENERGY
under contract DE-AC05-00OR22725

CONTENTS

LIST OF FIGURES

LIST OF TABLES

1. INTRODUCTION

Yutai Katoh (katohy@ornl.gov) and Bill Wiffen

The realization of fusion energy is a formidable challenge with significant achievements resulting from close integration of the plasma physics and applied technology disciplines. Presently, the most significant technological challenge for the near-term experiments such as ITER, and next generation fusion power systems, is the inability of current materials and components to withstand the harsh fusion nuclear environment. The overarching goal of the Oak Ridge National Laboratory (ORNL) fusion materials program is to provide the applied materials science support and understanding to underpin the ongoing Department of Energy (DOE) Office of Science fusion energy program while developing materials for fusion power systems. In doing so the program continues to be integrated both with the larger United States (US) and international fusion materials communities, and with the international fusion design and technology communities.

This long-running ORNL program on materials continues to pursue development of low activation structural materials such as the Reduced Activation Ferritic/Martensitic Steels, the higher strength/higher creep resistant Nano Composited Ferritic Steels, and Silicon Carbide Composites. New steel tasks are exploratory work on Bainitic steels and a helium-effects experiment using isotopically separated iron-54. A recent change is the increased emphasis on high heat flux testing and the development of refractory metals. This includes using an ORNL Plasma Arc Lamp facility adapted for the thermal testing of irradiated materials, the development and evaluation of new tungsten materials, and the study and understanding of the irradiation performance of tungsten. In each case the materials are being developed in a design-informed fashion where properties improvements are led by fusion-relevant design studies and directed at advancing the Technology Readiness Level of the material systems. A limited effort is directed towards diagnostic materials and high-temperature superconductors. This includes basic irradiation materials science of ceramics for diagnostic systems and quantifying the irradiation sensitivity of the most recently developed high-temperature superconductors tape materials. Finally, this program integrates fundamental modeling into the development efforts as much as practicable.

This program makes heavy reliance on neutron irradiation in the High Flux Isotope Reactor (HFIR) at ORNL. This is complemented by use of the ORNL-University of Tennessee ion irradiation facility and other available accelerator facilities when these are better suited to explore fundamental aspects of materials behavior under irradiation.

This document provides a summary of Fiscal Year (FY) 2015 activities supporting the Office of Science, Office of Fusion Energy Sciences Materials Research for Magnetic Fusion Energy (AT-60-20-10-0) carried out by ORNL. The organization of this report is mainly by material type, with sections on specific technical activities. Four projects selected in the Funding Opportunity Announcement (FOA) solicitation of late 2011 and funded in FY2012-FY2014 are identified by "FOA" in the titles. This report includes the final funded work of these projects, although ORNL plans to continue some of this work within the base program. Activity on "Materials Engineering in Support of the Fusion Nuclear Science Facility Program" is reported in Chapter 10.

The fusion materials effort includes collaborations within the US and with international partners. The major continuing international collaborating partners are the Japan Atomic Energy Agency (JAEA) (the US DOE-JAEA collaboration, focused on structural materials), the Japanese National Institute for Fusion Sciences [the PHENIX collaboration, emphasizing plasma facing materials and tritium fuel issues] and the Karlsruhe Institute of Technology in Germany (examining tungsten materials). New in FY2015 is a domestic collaboration, designed to provide specimens from the archive of HFIR-irradiated material to

other Office of Fusion Energy Sciences funded researchers to further their studies. Status of this work is reported in Section 11.1.

2. FUSION MATERIAL IRRADIATION TEST STATION

M. W. Wendel (wendelmw@ornl.gov), and P. D. Ferguson

OBJECTIVE

The Fusion Materials Irradiation Test Station (FMITS) is a proposed irradiation facility for the Spallation Neutron Source (SNS). This design and planning effort aims to develop the proposal and to minimize risk to SNS normal operations and safety. Because of the uncertainties associated with both modeling and ion irradiation experiments, there is a clear need for a fusion materials irradiation facility that can provide neutron irradiations with near-prototypic levels of helium- and hydrogen-production, along with displacement damage, for screening candidate fusion materials. A modest range of helium/displacements per atom (He/dpa) ratios is desirable to help calibrate and verify the studies using modeling and other simulation irradiation methods. Development of such a facility would provide the opportunity for the United States program to take the scientific lead in this critical area of fusion structural materials development.

SUMMARY

The FMITS is proposed as a modification to the SNS target station in order to promote advances in fusion materials studies. The feasibility of the FMITS was confirmed in Fiscal Year (FY) 2014 based on a Feasibility Study Report, a 30% Design Review, and a Preliminary Safety Assessment. Funding was provided in FY2015 to substantially reduce the project risks that were identified in the FY14 project plan. The technical risks were reduced by strengthening the preliminary safety assessment, securing the operational reliability case by computational simulation and remote handling mockup, and demonstrating the functionality of critical hardware based on the review committee recommendations. The efforts have been successful in all of the targeted areas.

PROGRESS AND STATUS

A fully loaded FMITS test section with tungsten material specimens was shown to be inherently safe from high-temperature interactions with water/hydrogen. A bounding estimate was made for a maximum release of activated tungsten from FMITS. By assuming previously calculated activities at beam shut-down the bounding offsite dose was estimated to be 0.45 rem. A credible accident case was not identified which could cause this high of a release. Detonations should not be possible since two hydrogen boundaries for the moderator are safety-credited and not enough hydrogen can be produced in the FMITS tungsten to cause a deflagration or detonation. Even if there was a deflagration it would be a low pressure discharge with respirable fractions of about 2% giving a much lower site boundary dose.

Computations were completed for off-normal cooling incidents in the FMITS test section with a detailed three-dimensional model to show that the thermocouple response is sufficient to protect SNS operations. Based on the 2014 review committee recommendation the case for operational reliability was strengthened by understanding how the proposed FMITS sensor array could be used to detect off-normal events before damage occurs to any components. These concerns were addressed by three-dimensional thermal modeling of a proposed FMITS experiment with inclusion of realistic thermocouple details. The sensitivity of each thermocouple to the changing thermal conditions was quantified, thus providing the necessary information to optimize a machine protection voting logic that would be effective to protect the SNS facility against power excursions and flow excursions. In general, the characteristic response time for all internal components varied between 8 s and 16 s. All the thermocouples showed an easily-measured 10°C increase within the first three seconds following the power increase. The centrally located

thermocouples showed a slightly faster response time than those on the ends of the experiment. Because of the relatively high mass flow, the coolant temperature was relatively insensitive to the power increase. These simulations will be completed in FY2016.

Remote handling mockup tests were completed that proved functional hardware configurations for connecting and disconnecting an FMITS harness. A wooden mockup was created of the electrical connector pocket that is located at the front of the SNS target carriage. Implementing FMITS would require a second connector in this region, and perhaps a third, so the mockup was developed using the proposed electrical connectors. Initial tests showed the first mockup configuration was manageable, but a lower connector location within the pocket could enhance the ability to remotely manipulate the connectors. Because the proposed FMITS-style electrical connectors have more pins than the current connector, the insertion force required to mate the connectors will increase. The successful completion of this mock-up means that the design of the FMITS-specific vent-line shield block can proceed.

Construction and testing of a double-inflatable pillow seal confirmed the capability in the FMITS design to sufficiently seal target and harness against the core vessel. FMITS-type (double-pillow) seal hardware was fabricated and successfully tested at bellows manufacturer KSM, Inc. The assembly was delivered to SNS and waits more extensive testing at ORNL. These tests will be completed during FY2016.

Design and testing of rupture tubes that could be used to protect safety-credited components at SNS from an over-pressurization of the FMITS test section was completed. The subcontract was awarded to Fike Corporation where initial testing was unsuccessful in producing repeatable results. Early results from a new design are positive. The final tests of twenty rupture tubes and subsequent report will be completed in FY2016.

Fabrication and testing of RTD-based miniature water flow sensor was begun at Delta M Corporation in Oak Ridge, TN. Such a sensor will bolster the FMITS instrumentation array thus protecting the operational reliability of SNS. The design and prototype are complete and the testing is underway, with the sensor to be delivered by January 1, 2016.

FUTURE PLANS

Completion of the double-inflatable seal testing and water flow sensor testing remain for FY2016. Also, the finite-element modeling of the FMITS test section transients will be completed. There are no plans for additional funding of this effort in FY2016. Future work will depend on the DOE's decision to move ahead with the project.

3. FOA – STRUCTURAL MATERIALS OF POTENTIALLY UNIQUE IRRADIATION RESISTANCE

Steve Zinkle, (zinklesj@ornl.gov)

This project is exploring the basic radiation resistance of three unique structural materials [high entropy crystalline alloys, bulk metallic glass, and MAX phase alloys] that may have the potential for very good resistance to neutron-induced property degradation.

3.1 PROPERTIES OF NEUTRON IRRADIATED MAX PHASE Ti-Al-C AND Ti-Si-C

Caen Ang, Chinthaka Silva, Takaaki Koyanagi, Chunghao Shih, Anne Campbell, Nesrin Cetiner, Yutai Katoh and Steven J. Zinkle

OBJECTIVE

The MAX phase materials are candidates for future nuclear reactor systems due to their expected radiation resistance and promising damage tolerance. This is due to their alternating ceramic/metal crystal structure, which not only offers high sink strength for mitigation of radiation induced defects but also a reported reversible deformation mechanism that promises pseudo-ductility. The objective of the program is to determine the viability of MAX phase materials and to understand their response to neutron radiation.

SUMMARY

This year completed the majority of post-irradiation testing of the MAX phase materials purchased from 3-ONE-2, LLC. Neutron irradiation was conducted at the High Flux Isotope Reactor (HFIR) to a neutron fluence of 2 x 10^{25} n/m^2 (E > 0.1 MeV), with an estimated atomic displacement damage of ~2 dpa based on silicon carbide (SiC). The irradiation temperature (T_{irr}) was determined by SiC temperature monitors inserted in the capsules. The T_{irr} values were determined to be 382-438°C and 629-718°C.

PROGRESS AND STATUS

Figure 1 shows the irradiation-induced lattice swelling of the Ti_3SiC_2 materials including data from other ion and neutron irradiation campaigns since 2011. It indicates that between room temperature and 300°C, irradiation induced lattice swelling is significant. In these materials, c-axis lattice swelling was 1.5% and the total volume swelling was measured as 0.7%. As noted in a previous report, the strength of Ti_3SiC_2 was retained after irradiation. At T_{irr} of 629-718°C, minimal lattice swelling was observed, but volume swelling had increased to ~1.5%, indicating additional volume from events such as phase changes or micro-cracking.

Figure 2 shows the irradiation induced swelling of the Ti_3AlC_2 materials including data from other ion and neutron irradiation campaigns. While similar trends are observed, the swelling is substantially larger by ~50%, resulting in 3-4% volume swelling that saturates at about ~2 dpa. Lattice swelling in this work reached values of 3.1% for c-axis expansion and a-axis shrinkage was 1.0%, indicative of a highly anisotropic swelling. As noted in a previous report, after low T_{irr}, the strength of the Ti_3AlC_2 material was 10% of the pre-irradiation strength, which was explained by extensive micro-cracking observed throughout the specimens at this temperature. T_{irr} of 629-718°C, minimal swelling was observed. Although cracks appeared in specimens irradiated at these temperatures, Ti_3AlC_2 maintained adequate strength.

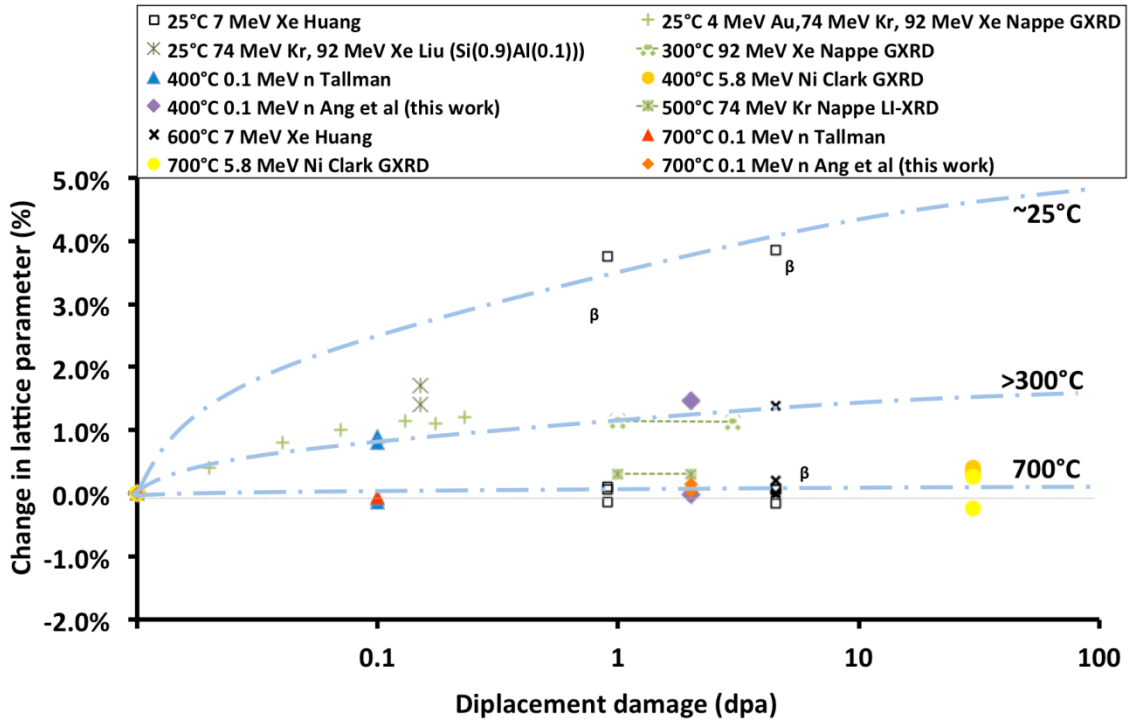

Figure 1. Irradiation induced swelling measured by GXRD (Grazing incidence X-ray Diffraction) or XRD on predominantly Ti_3SiC_2 materials. Positive values denote c-axis swelling, while negative values denote the a-axis shrinkage.

Other properties of the two MAX phase materials were investigated. Reduced thermal and electrical conductivity in both materials at the irradiation temperature of 382-438°C was observed. Thermal analysis indicated that once temperatures reached 600°C, these properties recovered to pre-irradiation values. This suggests that below this temperature, defects or defect clusters are immobile; above this temperature, thermal mobility dissipates defect clusters. This suggests better potential of these materials at the operational range of at least 629-718°C.

FUTURE PLANS

Analysis is continuing on MAX phase materials. While defect analysis may be restricted on Ti_3AlC_2 due to limits in phase analysis, damage tolerance and morphology of observed plastic deformation provides insight into purported pseudo-ductility and load transfer despite the presence of substantial cracking that should represent stress concentrations. In Ti_3SiC_2 analysis will focus on the viability of these materials, particularly the reduced swelling compared to the Al-containing counterpart. Finally, access to higher irradiation dose specimens should be available in late 2016.

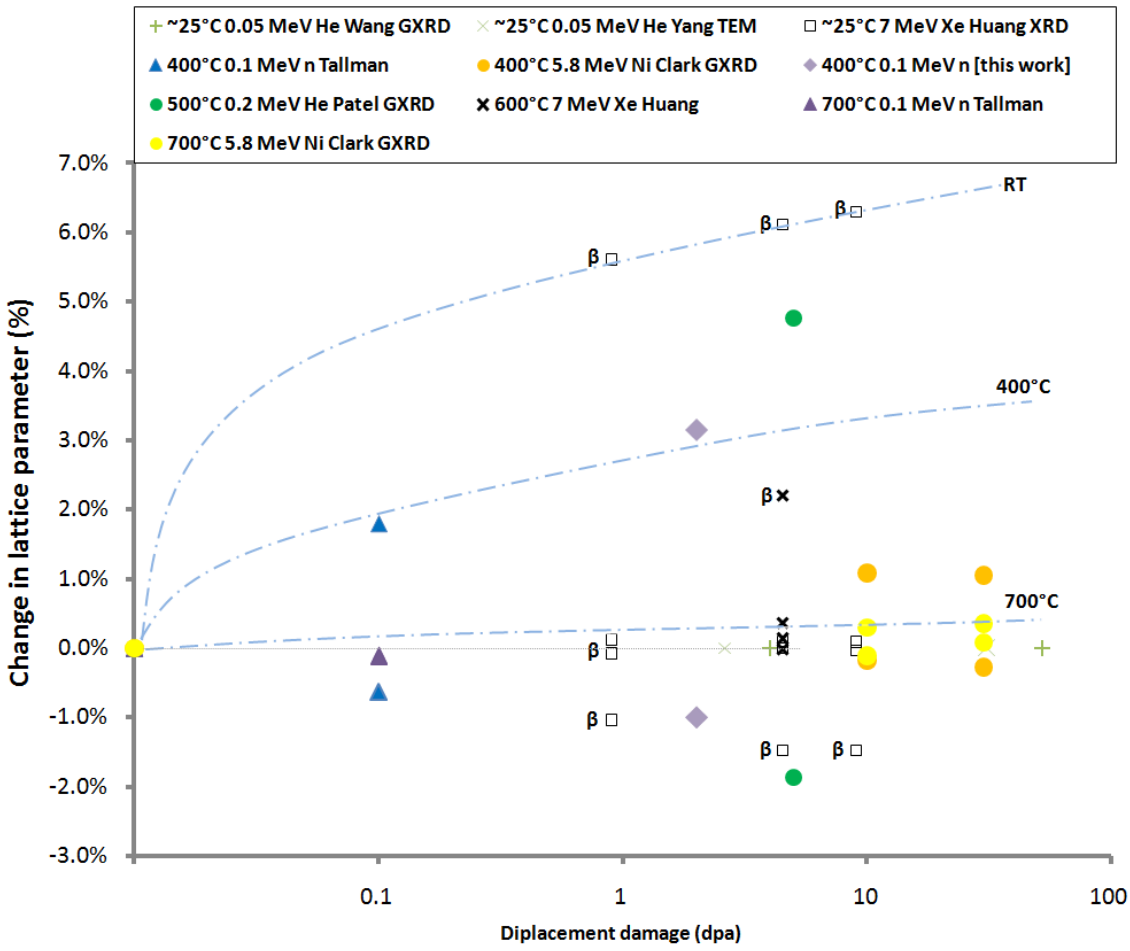

Figure 2. Irradiation induced swelling measured by GXRD, TEM or XRD on predominantly Ti_3AlC_2 materials. Positive values denote c-axis swelling, while negative values denote the a-axis shrinkage.

4. ADVANCED STEELS

4.1 FOA - DEVELOPMENT OF HIGH-Cr ODS ALLOYS WITH Zr ADDITIONS FOR FUSION REACTOR APPLICATIONS

B. A. Pint (pintba@ornl.gov), S. Dryepondt, D. T. Hoelzer, and K. A. Unocic

OBJECTIVE

The goal of this project is to develop an oxide dispersion strengthened (ODS) FeCrAl alloy with improved compatibility with Pb-Li and excellent mechanical properties.

BACKGROUND

The initial focus was on alloys with a base composition of Fe -12wt.% Cr-5Al and mechanical properties, microstructure and Pb-Li compatibility were evaluated. The Cr and Al contents were selected based on initial screening studies of cast and wrought FeCrAl where it was found that Al contents near 5%Al showed the best Pb-Li compatibility. The Cr content was decreased from the typical ~20%Cr to 12%Cr to reduce the tendency for radiation induced embrittlement due to Cr-rich α´ formation.

PROGRESS AND STATUS

The two new alloys were fabricated this year, designated 125YF (Y_2O_3 and FeO additions) and 125LZ (La_2O_3 + ZrO_2), and their tensile properties are shown in Figure **3**. The 125YF composition was selected because the previous base alloy, 125Y, had a much lower O content (~50% less than the other alloys) and FeO was added to increase the O content, Table 1. The new alloys have similar properties to the previous alloys, 125YN and 125YZ, with HfO_2 and ZrO_2 additions, respectively (only 125YZ is shown in Figure **3** for clarity).

Table 1. Alloy chemical compositions (mass% or ppmw for O, C, N and S) determined by inductively coupled plasma analysis and combustion analysis.

Material	Fe%	Cr%	Al%	Y%	O	C	N	S	Other
Powder	82.8	12.1	5.0	<	64	31	11	<3	0.004Si
125Y	83.3	11.4	4.8	0.19	842	380	455	20	0.05W, 0.02Si, 0.01Ti
125YZr	82.8	11.5	4.9	0.18	1920	250	160	10	0.30Zr, 0.01Hf, 0.01Si
125YHf	82.3	11.7	4.8	0.17	2280	220	110	10	0.68Hf, 0.01Zr, 0.01Si
125YTi	82.4	12.0	4.9	0.16	2220	350	135	30	0.20Ti,0.01Si
125YF	83.0	11.7	4.7	0.19	1920	200	202	30	0.01Ti,0.01Si,0.06W
125LZ	82.2	11.9	4.9	0.01	2500	260	103	30	0.27La,0.39Zr,0.01Hf
126ZY*	81.1	12.0	5.5	0.19	1360	190	130	50	0.49Zr,0.03Ti,0.05Si
126HY*	81.2	11.9	5.6	0.20	1070	260	100	40	0.83Hf,0.02Si,
PM2000	74.1	19.1	5.5	0.39	2480	14	86	8	0.48Ti, 0.02Si
APMT	69.8	21.2	4.8	0.21	519	360	530	<3	2.8Mo,0.1Zr,0.2Hf,0.5Si

< indicates below the detectability limit of <0.01%
* powder only

Creep testing has been completed at 800°C (Figure 4) and one 125YZ test is continuing past 8,000 h at 700°C and 140 MPa. The new ODS alloys are significantly stronger than wrought FeCrAl and commercial dispersion strengthened alloys, Kanthal APMT and Plansee PM2000. Most commercial PM2000 (20Cr-5.5Al) alloy was optimized for >1000°C creep strength so PM2000 powder was extruded under the same conditions at 950°C as the new 12Cr-5Al alloys but did not show good creep strength (labeled ORNL PM2000 in Figure 4).

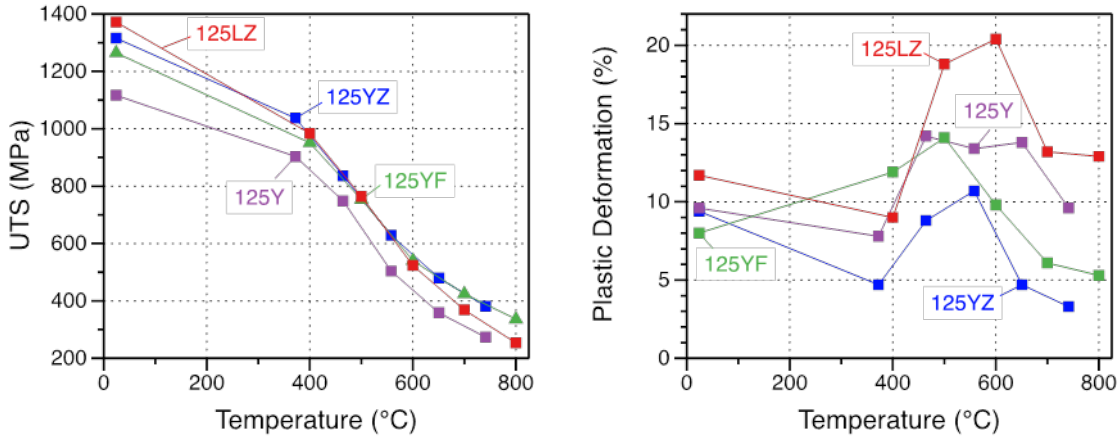

(a) (b)

Figure 3. Tensile properties of the ODS FeCrAl heats as a function of test temperature. (a) ultimate tensile strength and (b) total plastic deformation.

The good creep strength of the new ODS alloys, particularly 125YZ, is attributed to the fine (~200 nm) grain size (Figure 5a) and uniform distribution of Al-Y-Zr-O nano-clusters, which were clearly identified using the new FEI Talos analytical TEM, Figure 5b. While it was not practical to use TEM to study the microstructural stability after different anneals, alloy hardness was used to quickly assess the microstructure stability after annealing for up to 1000 h at 800-1200°C,. Some drop in hardness was seen for all of the 12Cr-5Al alloys, Figure 6, but the base alloys 125Y and 125YF showed the largest drop and 125LZ and 125YH appeared to be the most stable. In contrast, PM2000 remained almost unchanged after long times and high temperature anneals.

Figure 7 summarizes the isothermal Pb-Li compatibility at 700°C of the new alloys compared to ODS Fe-Cr alloys and wrought FeCrAl. Without Al to form a protective Al-rich oxide, the ODS Fe-Cr alloys 14YWT (Fe-14Cr-3W) and ODM401 (Fe-15Cr) showed high mass losses due to dissolution of Fe and Cr in the liquid metal. The benefit of 3.9-4.4wt.%Al was observed in wrought FeCrAl, but even lower mass losses were observed in ODS FeCrAl with ~5%Al, similar to PM2000 with 20%Cr.

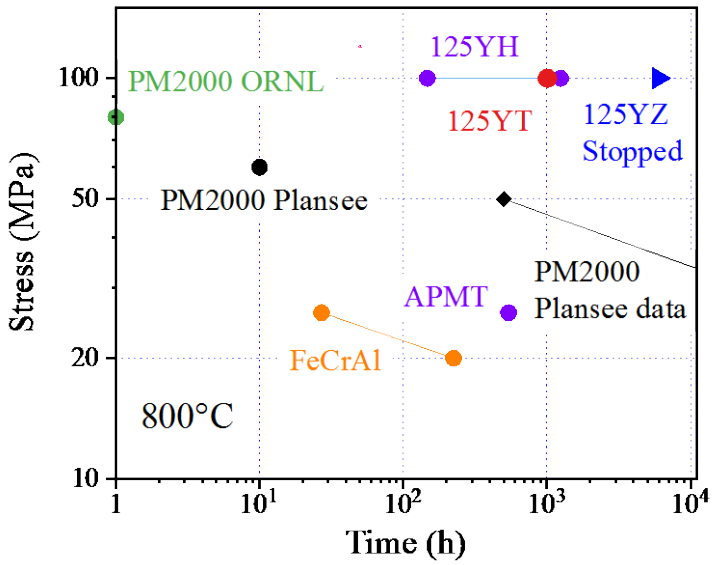

Figure 4. Lifetime at 800°C versus applied stress for the ODS Fe-12Cr-5Al, PM2000 and APMT alloys.

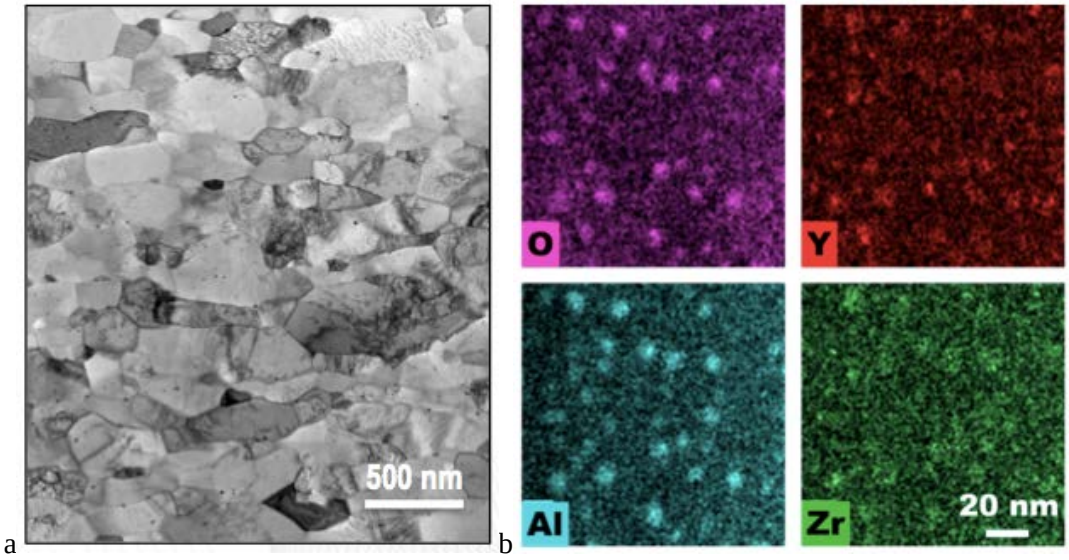

Figure 5. Microstructure of 125YZ (Fe-12Cr-5Al+$Y2O_3$-ZrO_2) (a) TEM bright field image of fine grain structure and (b) EDS maps of Al-Y-Zr-O nano-clusters.

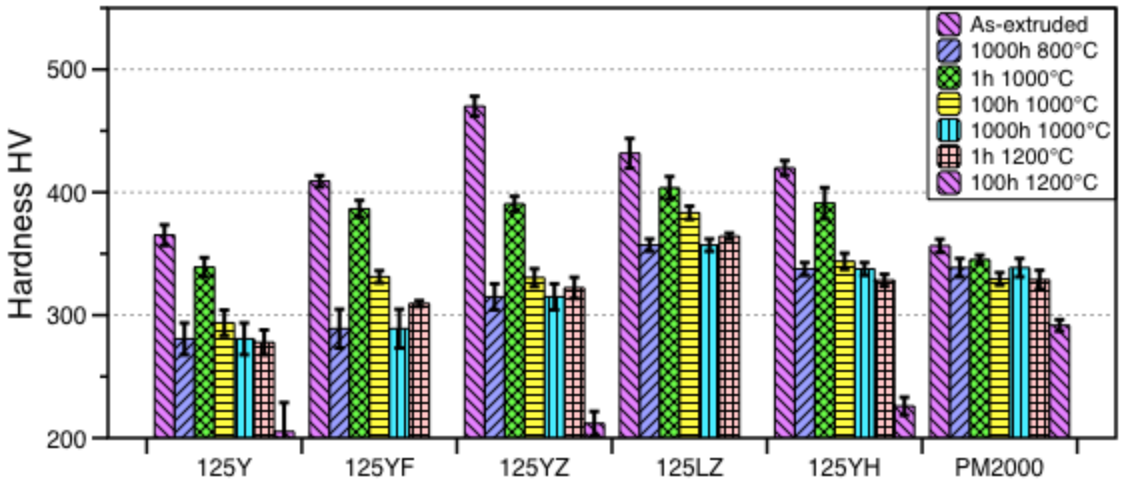

Figure 6. Vickers hardness of ODS alloys as-extruded and after various anneals at 800-1200°C.

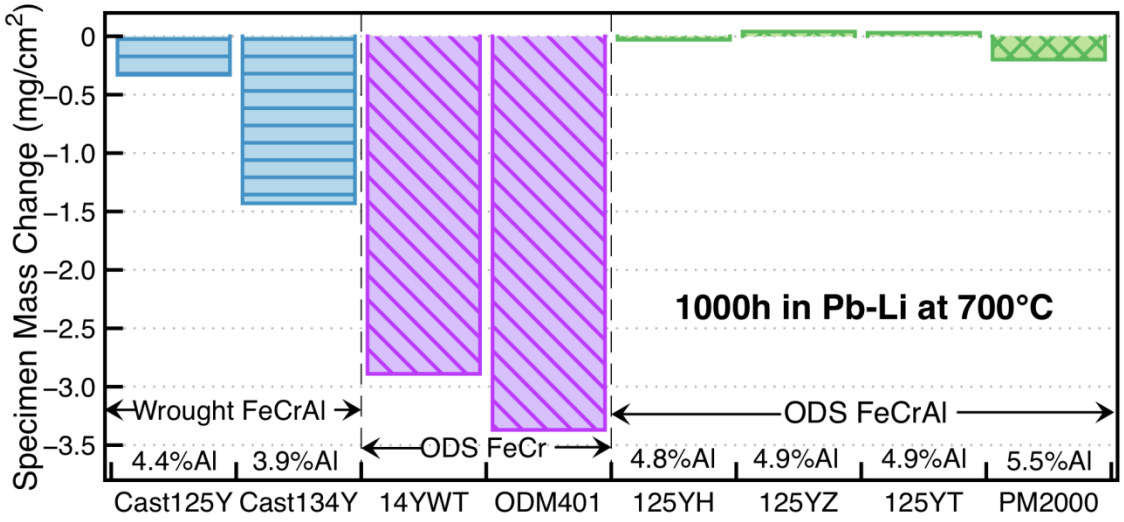

Figure 7. Mass change for alloy specimens exposed in static Pb-Li for 1000 h at 700°C.

FUTURE PLANS

New powder batches with Fe-12Cr-5.5Al and alloy additions of Zr and Hf have been milled and are awaiting consolidation. Chemical analysis of the powder, labeled 126ZY and 126HY in Table 1, showed that the oxygen content was ~1000 ppmw, lower when the Zr and Hf were added as alloy additions rather than as oxides in the 125YZ and 125YH alloys. Characterization and testing of the new alloys will determine if the lower O content has improved the properties of this iteration of ODS alloys for application in a high performance fusion blanket application.

4.2 DEVELOPMENT OF ADVANCED RAFM STEELS – CNA ALLOYS

L. Tan (tanl@ornl.gov)

OBJECTIVE

Traditional reduced activation ferritic-martensitic (RAFM) steels suffer noticeable strength reduction at temperatures above ~500°C, which limits their high temperature applications for DEMO and advanced fusion reactors. The goal of this project is to develop Cast Nanostructured Alloys (CNAs) that are manufacturable and affordable advanced RAFM steels with optimized alloy compositions and thermomechanical treatment to produce a high density of stable nano-precipitates that allow the CNAs to provide superior high temperature performance.

SUMMARY

Three heats of CNAs were designed and fabricated, among which one of the heats is primarily strengthened by MN nano-precipitates such as (V,Ta)N and the other two heats primarily by MC such as TiC and TaC. The CNAs were designed to maximize the amount of nano-precipitates and still retain an acceptable temperature range for the austenite phase at high temperatures to facilitate thermomechanical treatment of the alloys. Compared to Grade 91 steel, the CNAs exhibited increased strength in tensile tests and preliminary creep tests, comparable or lower ductile-brittle transition temperature, as well as comparable or significantly greater upper-shelf energy in Charpy V-notch impact tests. Recent welding trials of the CNA1 with MN precipitates, using conventional tungsten inert gas (TIG) and the state-of-the-art Friction Stir Welding (FSW), demonstrated the weldability of the alloy.

PROGRESS AND STATUS

Following the successful study on the stability of MX-type nano-precipitates TaC, TaN, and VN under Fe^{2+} ion irradiation up to ~49 dpa at 500°C, the same types of nano-precipitates after Fe^{2+} ion irradiation to ~246 dpa at 500°C have been characterized by transmission electron microscopy (TEM). The evolution of the nano-precipitates under these high radiation doses was analyzed semi-quantitatively. Some growth of VN particles was measured, and found to be highly dependent on the ion irradiation direction, which will be further confirmed by characterizing additional TEM specimen(s) with different grain orientations.

Conventional TIG welding was conducted on the CNA1 (1-in. thick plates) that is primarily strengthened by MN. Standard commercial Grade 92 type filler wire (1 mm diameter), complying with AWS A5.28M ER90S-G (92), was used in the TIG practice because of the unavailability of RAFM type filler wire. A post weld heat treatment (PWHT) at 750°C for 1 h was applied to the welds. Side-bending test of the 3/8-in. thick cross-weld coupons, following relevant ASME Section IX standards, did not show noticeable cracks under an optical microscope, except for a few small voids in the weld metal. The results suggested satisfactory weldability of the alloy plate. Vickers hardness was measured perpendicular to the heat-affected zone (HAZ) from the weld metal to base metal. The hardness profile is shown in Figure 8 in the black curve. Additionally, FSW of CNA1 (0.32-in.-thick plate) and Eurofer97 (0.59-in.-thick plate) was investigated by Z. Yu et al. [Z. Yu, Z. Feng, D. Hoelzer, L. Tan, M.A. Sokolov, Metall. Mater. Trans. E (2015), in press.]. For comparison, the Vickers hardness profiles from the stir zone (SZ) to base metal of the FSW-CNA1 and FSW-Eurofer97, as well as the FSW-CNA1 with PWHT at 760°C for 0.5 h, are included in Figure 8. The inset of Figure 8 shows the hardness ranges of the welds in the four conditions with the colors denoting the corresponding hardness profiles. The white lines intersecting the hardness ranges indicate the average hardness of the base metals. The FSW samples without PWHT exhibited the largest hardness ranges. After PWHT, the FSW-CNA1 showed reduced fluctuation in hardness, and a

slightly smaller hardness range than the TIG-CNA1. The higher hardness of the weld metal of the TIG-CNA1 may be attributable to the high strength Grade 92 type filler metal. Using the base metal as filler metal is expected to decrease the hardness range of the TIG-CNA1.

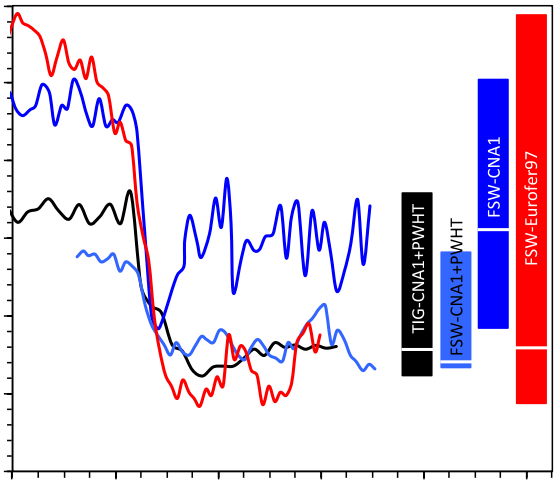

Figure 8. Comparison of Vickers hardness profiles across HAZ in the welds of CNA1 and Eurofer97 in different conditions.

Similar to other TIG FM steel welds, the TIG-CNA1 with PWHT showed minimum hardness at HAZ adjacent to the base metal as shown in Figure 8. In contrast, the FSW-CNA1 with PWHT showed a relatively smooth decrease in hardness from the SZ to base metal. Figure 9 shows optical micrographs of the HAZ in the TIG-CNA1 and FSW-CNA1. In contrast to the refined ferrite grains in the TIG-HAZ, the FSW-HAZ is composed of a tempered martensite microstructure. The FSW trial suggests the applicability of FSW to relatively thin component, which may yield comparable or better quality welds as compared to conventional TIG. Mechanical testing will be pursued to compare their performance.

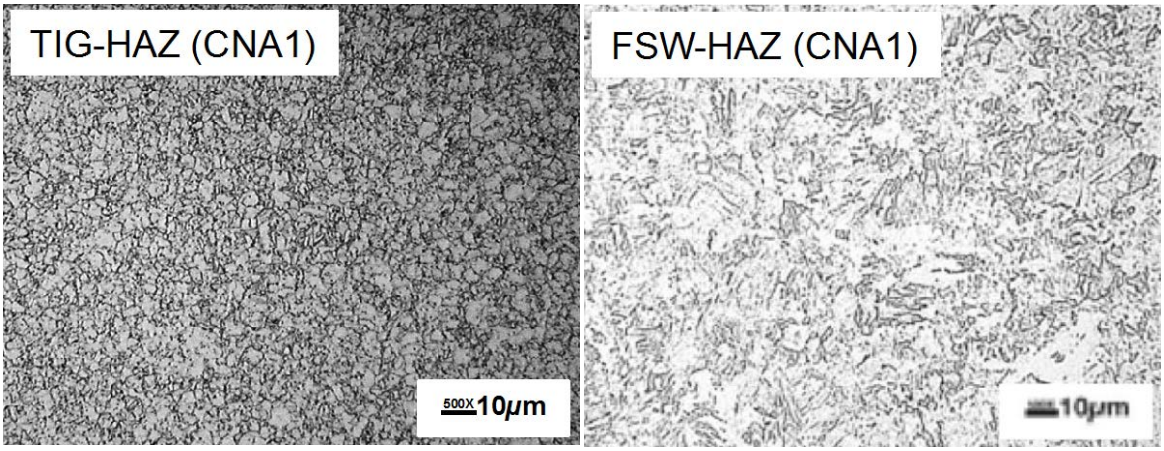

Figure 9. Optical micrographs showing microstructures of HAZ in the welds of CNA1, which were fabricated by TIG and FSW methods.

FUTURE PLANS

Development of CNAs will be continued, including larger heat production by a commercial vendor to conduct multiple same-heat tests. The HFIR neutron irradiation of the CNAs will be planned/initiated. Post irradiation examination of the neutron-irradiated TaC, TaN, and VN samples at 300, 500, and 650°C for up to ~20 dpa, together with the high dose Fe^{2+}-irradiated samples, will be conducted.

4.3 DOE-JAEA COLLABORATION ON IRRADIATION EFFECTS IN F82H

H. Sakasegawa (sakasegawah@ornl.gov), M. Ando, H. Tanigawa, and Y. Katoh

OBJECTIVE

Higher dose irradiation data on reduced activation ferritic-martensitic is indispensable to design the fusion DEMO blanket. However, mechanical property data after high-dose neutron irradiation, above 80 dpa, are still not obtained. The objective of this work is to perform tensile tests of irradiated F82H steel samples from HFIR-JP28 and 29 capsules (~85dpa; 44 cycles) and apply three dimensional fractography on ruptured specimens to understand the fracture mechanism.

SUMMARY

The F82H-IEA and F82-MOD3 heats tensile specimens irradiated above 80 dpa in High Flux Isotope Reactor (HFIR) were tested at their irradiation temperatures in the Oak Ridge National Laboratory 3025E hot cell facility. Irradiation hardening and embrittlement were observed with increasing dose, though the strengthening had been expected to be saturated at around 20 dpa. The 3D images of fracture surface were produced taking pictures from three different tilt angles on a ruptured HFIR irradiated specimen. This revealed that some irradiated specimens showed a shear rupture mode.

PROGRESS AND STATUS

Table 2 summarizes the disassembled HFIR-JP28 and 29 tensile specimen holders after HFIR irradiation. Tensile tests were performed on the SS-J3 type tensile specimen of F82H-IEA and F82H-MOD3 heats from the JP28 #7 and #9 holders at their irradiated temperatures of 673 and 773 K, respectively. As shown in Figure 10, the 0.2 % yield stress and ultimate tensile stress increased, and their ductility has deteriorated with increasing dose, though these irradiation hardening and embrittlement have been expected to be saturated around 20 dpa before seeing these results. Tensile tests of other specimens are continued to obtain and accumulate mechanical property data of high-dose neutron irradiated material.

Table 2. Disassembly results for JP28&29 tensile holders.

No	Holder No.	Irrad. Temp. (K)	Dose (dpa)	Cut	SS-J3	APFIM/MMPC	Passive TM
				Number of specimens (missing), [broken]			
1	JP28 #7	673	85.4	1	16 (0)	17 (0)	8 [0]
2	JP28 #9	773	81.8-83.4	2	16 (0)	16 (0)	8 [0]
3	JP29 #7	573	85.9-86.8	-	16 (0)	16 (0)	8 [0]
4	JP29 #10	573	76.9-79.9	1	17 (0)*	17 (0)	8 [0]
5	JP29 #13	573	46.9-52.9	3	16 (0)	16 (0)	8 [0]
6	JP29 #2	673	45.7-51.8	1	16 (0)	16 (0)	7 [1]
7	JP28 #3	573	66.8-70.8	-	16 (0)	13 (3)	7 [1]
8	JP28 #1	673	41.7-47.9	1	16 (0)	15 (1)	7 [1]
9	JP29 #3	773	58.7-63.7	1	16 (0)	15 (1)	8 [0]
10	JP29 #12	573	58.7-63.7	-	16 (0)	14 (2)	8 [0]

* Including 3 SSJ2 specimens

Figure 11 shows a 3D image of the fracture surface of the F82H-MOD3 heat specimen irradiated to 2.7 dpa at 573 K in HFIR and tested at 573 K. Three pictures of tensile specimen rupture surfaces were taken from different tilt angles to process this image. The result revealed that the irradiated specimen failed mainly in a shear rupture mode, with a small area fraction of dimpled surface. The corresponding quantitative data are shown in Figure 12. These data indicated that the fracture surface slanted with an angle of about 54 degrees to the tensile axis. This information is very helpful to understand details of irradiation effects on the rupture mechanisms, and it may be possible to obtain true fracture initiation strain, which is more consistent with the true tensile fracture nature than is reduction in area.

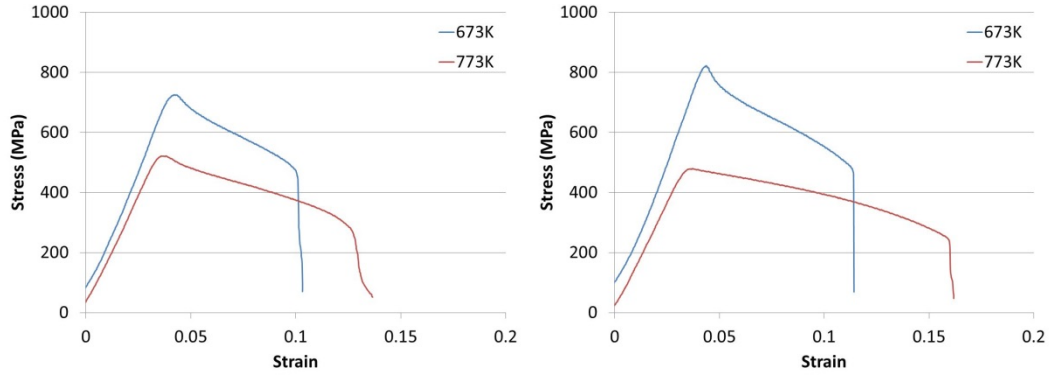

F82H-IEA heat *F82H-MOD3 heat*

Figure 10. High temperature tensile tests of high-dose neutron irradiated F82Hs.

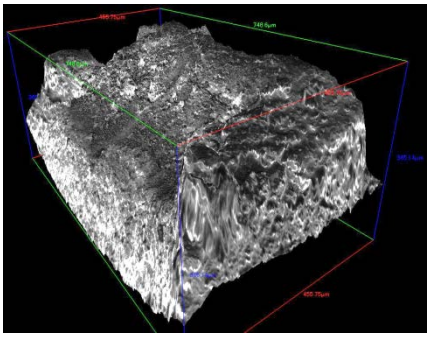

Figure 11. 3D image of the fracture surface of an F82H sample irradiated in HFIR to 2.7 dpa at 573 K and tensile tested at 573 K.

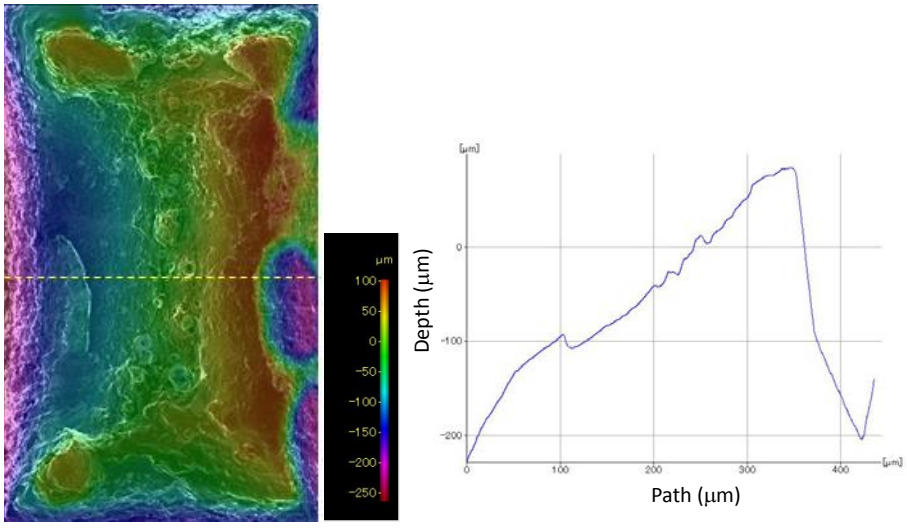

Figure 12. 3D profile of the tensile fracture surface (Left) and line profile (Right) of the relative heights along the broken yellow scan line indicated on the 3D profile. This is the specimen imaged in Figure 11.

FUTURE PLANS

Tensile tests will continue on the SS-J3 type tensile specimens from capsules JP28 and 29 in Fiscal Year 2016, and then three dimensional fractography will be performed on ruptured specimens. In addition, a non-contact extensometer will be applied to properly measure strain of the small size specimens.

4.4 NEW BAINITIC STEEL FOR FUSION STRUCTURAL APPLICATIONS

Y. Yamamoto (yamamotoy@ornl.gov)

OBJECTIVE

This work aims to develop a new bainitic steel, based on 3Cr-3WV(Ta) steels originally developed at Oak Ridge National Laboratory (ORNL), with mechanical properties of both base metal and weldments superior to those of existing commercial bainitic steels or ferritic-martensitic (F-M) steels. The target applications are high temperature structural components in fusion reactors such as vacuum vessel, structural ring which supports the blanket modules, and magnet shields, to be used at or above the 400-500ºC temperature range. Improvement of long-term creep properties by introducing additional fine, stable second-phase dispersions, as well as maintaining good weldability, is targeted via optimization of alloy composition and thermo-mechanical heat treatment.

SUMMARY

Four heats of 3Cr-3WV(Ta) bainitic steels were delivered to ORNL. Minor alloying additions of Mn, Si, and N resulted in increasing creep-rupture life of the 3Cr-3WVTa base steel at 600°C and 200MPa, which exceeded the rupture-life of P92, whereas there was no significant improvement observed due to modifying the 3Cr-3WV base steel. The continuous cooling transformation diagrams of the steels indicated that the minor alloying additions lowered the bainitic transformation temperature significantly. This allows a wider cooling-rate window for the carbide-free acicular bainite ferrite formation in the modified steels compared to the base steel, which plays an important role in improving the creep properties. Autogenous gas tungsten arc welds were conducted for evaluation of weldment characteristics, and cross-sectional microstructure characterization was initiated.

PROGRESS AND STATUS

The forged plates of two base bainitic steels and two modified steels have been prepared by Carpenter Technology Corporation. Table 3 summarizes the analyzed compositions of the steels in the present study. The heats with nominal mass 18 kg were vacuum induction melted and cast into a mold with a size of 10 cm x 10 cm x 20 cm (plus hot-top). The ingots were homogenized and forged at 1100ºC to make plates with a size of 25 mm thickness x 15 cm width x ~40 cm length, then normalized at 1100°C. A part of each plate was sectioned, and tempered at 700ºC for 1h, followed by air cooling.

Table 3. Analyzed compositions of the steels in the present study.

Heat	Composition, wt.% (balanced Fe)								Remarks
	C	Mn	Si	Cr	N	V	W	Ta	
2750	0.10	0.40	0.15	2.95	0.00	0.20	3.01	<0.01	3Cr-3WV, base
2751	0.10	0.40	0.14	2.95	0.00	0.20	3.03	0.10	3Cr-3WVTa, base
2752	0.10	0.98	0.49	2.98	0.017	0.20	3.02	<0.01	Modified 3Cr-3WV
2753	0.11	1.00	0.48	2.95	0.014	0.20	3.03	0.09	Modified 3Cr-3WVTa

Creep-rupture tests of the base and modified bainitic steels were conducted at 600°C. The creep-rupture life of the steels tested at 600ºC and 200 MPa are shown in Figure 13. The rupture life of P92 (9Cr-2W base) ferritic-martensitic steel is also shown for comparison. The results indicate a significant advantage of the bainitic steels over the existing F-M steel in the creep properties at this test condition. It was found

that the minor alloying addition improved the rupture life of the 3Cr-3WVTa base steels, whereas no significant improvement was observed in the 3Cr-3WV base steels.

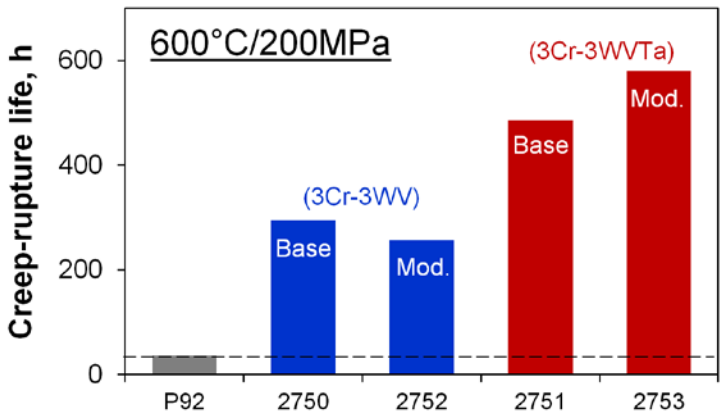

Figure 13. Creep-rupture life of the bainitic steels tested at 600°C and 200 MPa, compared with that of P92 F-M steel.

Dilatometer analysis of the steels confirmed that the minor alloying additions successfully lowered the bainite transformation temperatures. Figure 14 showed continuous cooling transformation diagrams for the bainitic steels obtained using a quenching dilatometer (Materials Measuring Corporation, Westbury, NY), representing the bainitic transformation start (B_s) and finish (B_f) temperature during continuous cooling with several different cooling rates in the range 1 to ~180°C/s. The base steels (heats #2750 and #2751) showed very similar transformation kinetics with the B_s of ~510-570°C and B_f of ~340-370°C, and no apparent effect of the Ta addition on the kinetics was observed. On the other hand, the minor alloying additions resulted in ~50-70°C lowering of both B_s and B_f temperatures. These results indicate that the transformed bainite ferrite would contain larger amounts of supersaturated carbon and nitrogen than the base steels because the transformation temperature is low enough to expect limited migration of such elements in the matrix. This would result in a wider cooling-rate window for the carbide-free acicular bainite ferrite formation in the modified steels compared to the base steels.

Autogenous gas tungsten arc welds (GTAW) on the four different heats, for both as-normalized and tempered plates, were completed as shown in Figure 15. Two weld beads were applied with offset-center in order to observe the microstructure of the heat affected zone not only in the base metal but also in the weld bead (tempered bead). Cross sectional specimens have been prepared, and microstructure characterization as well as the hardness analysis across the fusion zones is currently in progress.

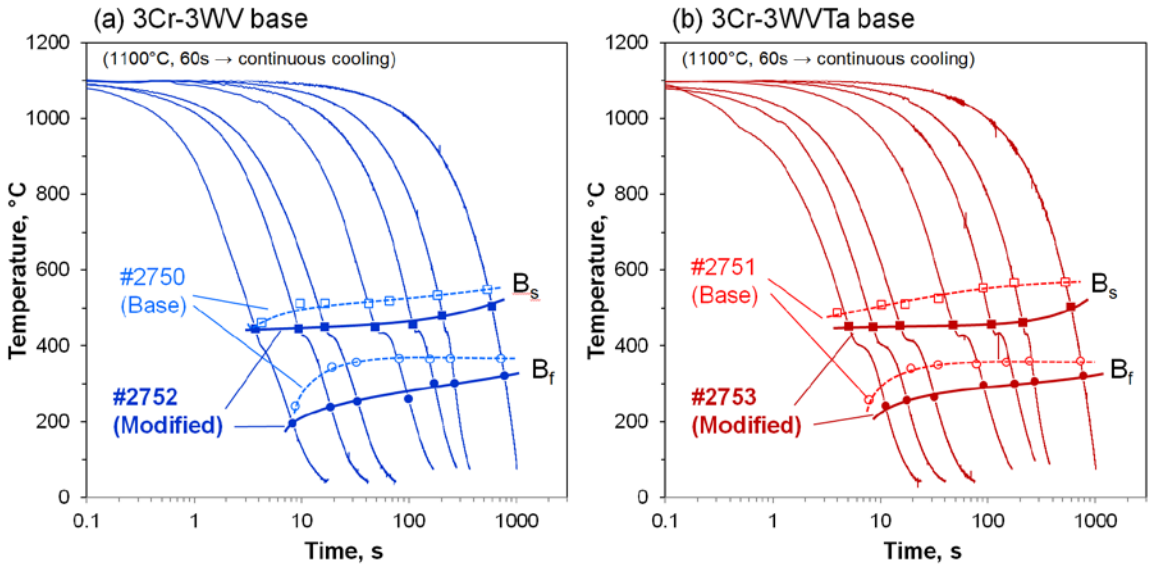

Figure 14. Continuous cooling transformation diagrams of the bainitic steels; (a) 3Cr-3WV base, and (b) 3Cr-3WVTa base steels.

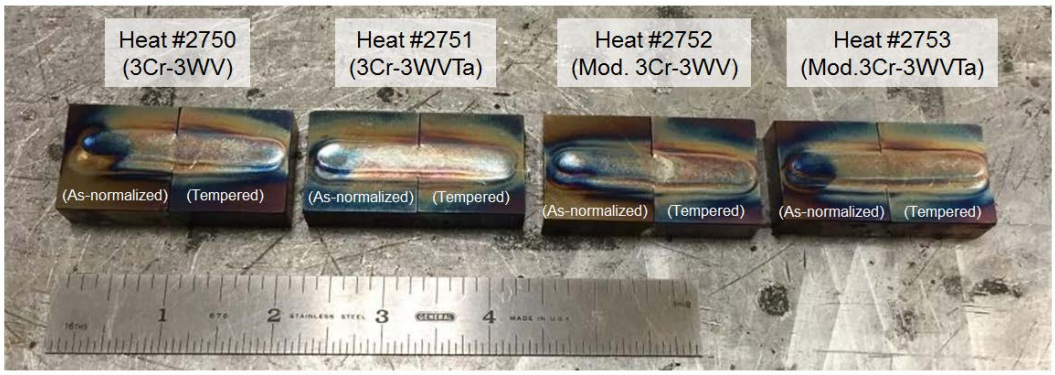

Figure 15. Photo of autogenous GTAW on the four different bainitic steels which were applied to both normalized(as-normalized) and tempered (tempered) steel.

FUTURE PLANS

Detailed microstructure characterization will be conducted, and the results will be correlated with the creep-rupture properties and the weld characteristics. Optimization of alloy compositions will be pursued with the target of developing bainitic steels that do not require post-weld heat treatment, without losing the advantage of the base metal creep properties compared to existing F-M steels.

4.5 ACCELERATED EVALUATION OF IRRADIATION EFFECTS IN 9Cr RAFM STEELS USING ^{54}Fe ISOTOPE

Y. Yamamoto (yamamotoy@ornl.gov), J.K. Thomson, J.R. Keiser, L. Tan, K.G. Field

OBJECTIVE

The primary goal is to evaluate the effect of transmutation helium during neutron irradiation on the irradiation microstructure and mechanical properties of 9Cr base reduced activation ferritic-martensitic (RAFM) steels, such as EUROFER 97 and CNA. Alloys prepared using ^{54}Fe isotope will accelerate the helium production during fast neutron exposure at HFIR which allow simulating the high dose conditions within relatively short period of exposure time. The ^{54}Fe isotope has been obtained reduced from the steel oxide powder provided by Karlsruhe Institute of Technology (KIT).

SUMMARY

Reduction of the mixed oxide steel powder that consisted primarily of ^{54}Fe was successfully conducted via a combination of a hydrogen reduction process and arc-melting with reactive elements. The arc-melted ingot of ^{54}Fe to date contains 78 wppm oxygen and 70 wppm nitrogen, together with ~1 wt.% of Cr and W. Mixing with additional Cr, W, Mn, V, and Ta, to fabricate 9Cr RAFM steels is planned.

PROGRESS AND STATUS

Figure 16 represents the reduction sequence of the ^{54}Fe oxide powder. About 400 g of mixed oxide steel powder was delivered which consisted primarily of ^{54}Fe together with small amounts of Cr, W, and other alloying elements. The powder was provided by KIT, but had been oxidized during a recovery process used to eliminate some carbon and boron contamination of the EUROFER 97 powder. X-ray diffraction analysis of the as-received powder indicated that most of the oxide was Fe_2O_3-type. This powder was reduced in flowing hydrogen at 850ºC for 12 h, cold-pressed to a pellet, and then sintered in flowing hydrogen at 1100ºC for 2 h. The pellet was arc melted to produce a button ingot which still contained ~0.22 wt.% matrix oxygen. The ingot was re-melted with Al and Si to further reduce the oxygen level. The resulting steel ingot had an oxygen content of less than ~0.008 wt.%.

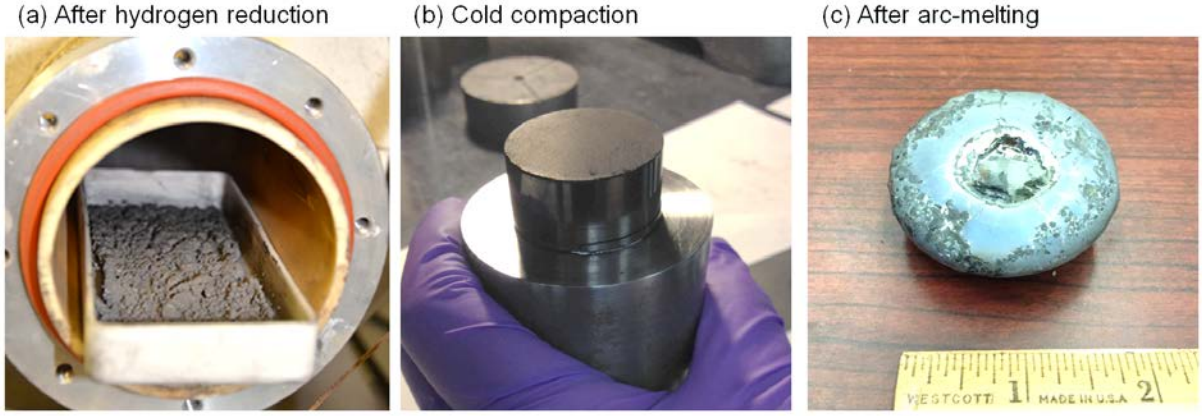

Figure 16. Reduction sequence of ^{54}Fe oxide powder; from hydrogen reduction to arc-melting.

FUTURE PLANS

The arc-melted ingot will be mixed with additional Cr, W, Mn, V, and Ta to fabricate 9Cr RAFM steels. The ingots will be forged and rolled to make plate-shape specimens, and then standard heat-treatments applied. The materials will be used for evaluation of mechanical properties and irradiation testing.

4.6 FOA-FRICTION STIR WELDING OF ODS STEELS AND ADVANCED FERRITIC STRUCTURAL STEELS

Z. Feng (fengz@ornl.gov), W. Tang, X. Yu, G. Chen, D. Hoelzer, and L. Tan

OBJECTIVE

This project addresses the critical technology gap of joining oxide dispersion strengthened (ODS) steels, nanostructured ferritic alloys (NFAs), reduced activation ferritic-martensitic (RAFM) steels, and dissimilar metal joining of ODS/NFAs and RAFM steels through Friction Stir Welding (FSW). The research focuses on understanding the stability of the strengthening phases in the weld region, and the bonding mechanisms between dissimilar structural steels as a function of FSW process conditions.

SUMMARY

In this final reporting period, the baseline FSW process conditions for joining ODS steels and RAFM steels have been successfully developed. A computational fluid dynamics based model has been developed and applied to understand temperature and material flow during FSW. Our research showed the sizes of the oxides/nano-cluster features, the primary strengthening phase in ODS alloys, is highly dependent on the FSW conditions. For the first time, local creep deformation behavior in different regions of FSW of RAFM steel in high temperature creep test was experimentally determined by a special high temperature Digital Image Correlation (DIC) technique. The creep test results revealed drastic increase in creep resistance (i.e. reduced creep rate) in the stir zone (SZ). It also revealed the creep resistance in the heat-affected zone (HAZ) of the weld, although higher than in the base metal (BM), is still better than the HAZ of a conventional fusion weld. Additional research is necessary to mature this feasibility into application.

PROGRESS AND STATUS

Microstructure characterization of 14YWT/9Cr weld. A defect-free FSW between 14YWT and 9Cr advanced steels was produced in Fiscal Year 2014. Both alloys were developed and produced at Oak Ridge National Laboratory (ORNL).

In this reporting period, 14YWT/9Cr steel FSW microstructures were characterized in detail by optical microscopy and scanning electron microscopy (SEM). Optical microstructures of the FSW joint in different metallographic zones are shown in Figure 17a. Obviously the FSW heat input was high enough to cause 14YWT grain growth and 9Cr steel martensitic transformation within the SZ. Also, micro hardness maps led to the same conclusion: 14YWT hardness drops and 9Cr hardness increases within the SZ, as is shown Figure 17b.

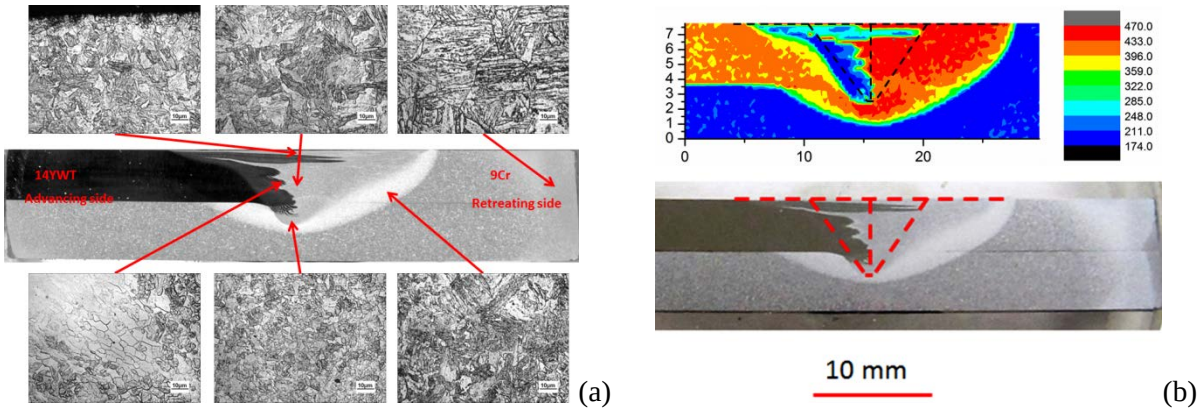

Figure 17. Microstructure and microhardness maps of FSW weldments. (a) Microstructures of 14YWT/9Cr joint. (b) Microhardness map of same region as shown in (a).

The SEM backscatter electron images of the SZ, HAZ and BM are shown in Figure 18. From those pictures, grain size of SZ, HAZ and BM are 5 – 10 microns, 1 – 2 microns and 0.3 – 0.5 microns, respectively. Obviously there was a significant grain growth in the SZ during FSW. It should be noted that the grain size in the SZ of this particular weld was much larger than that of a different 14YWT FSW we produced previously. This suggests the heat input for the weld studies in this period is much higher than previously used. Furthermore, the nano-sized precipitates in BM were not resolved by SEM since the size of these precipitates (nano-clusters) is on the order of 1-2nm. On the other hand, the "bright" precipitates inside the grains in SZ are on the order of 10-100 nm in size, indicate they are enlarged and enriched with higher atomic number elements such as Y and Ti; see Figure 19 for details. This aspect need to be further analyzed and understood.

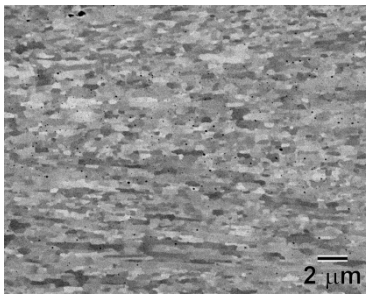

(a) Base metal

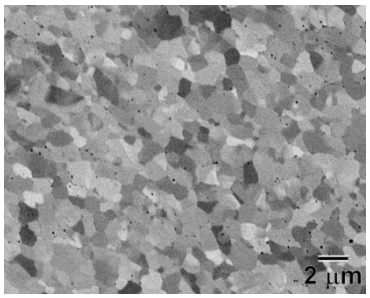

(b) Heat affected zone (HAZ)

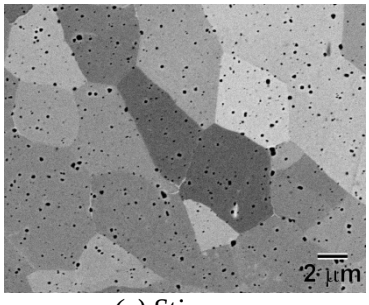

(c) Stir zone

Figure 18. SEM images of 14YWT in various metallurgical zones.

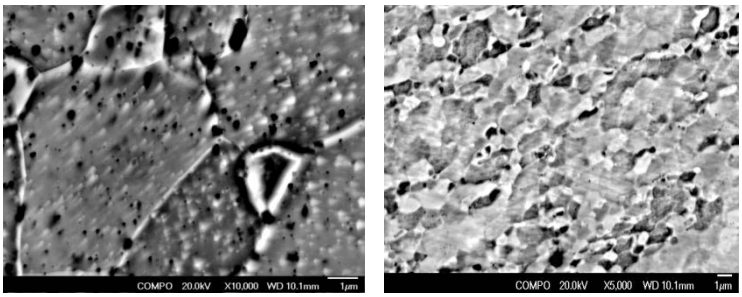

(a) 14YWT stir zone *(b) 14YWT base metal*

Figure 19. Grain and precipitate growth in the 14YWT SZ after FSW.

In our previous work it was found that FSW can preserve the nano-size precipitates in 14YWT – the mean size of the nano-clusters was 2.7 nm in the SZ, compared to 1.9 nm in the base metal. However, if the particles in Figure 19 were indeed Y-Ti oxide precipitates, they would be much larger than what we have observed in our earlier studies. This would suggest the welding process conditions (and the heat input level) can play a major role on the size of the strengthening Y-Ti particles. This effect of FSW on particle-strengthened steel requires additional study and confirmation.

High temperature creep testing and characterization of RAFM friction stir welds. Cross-weld creep test were performed on a RAFM friction stir weld that was produced early in this project. Round bar specimens were machined from the RAFM weld perpendicular to the weld, resulting in cross-weld specimens containing all different regions of the weld and base metal. Specimens were machined to 6 mm diameter with a gage length of 40 mm, as shown in Figure 20a.

Since the highly non-uniform microstructural gradients in the SZ and HAZ regions complicate the deformation of the weld in creep test, a unique high temperature DIC strain measurement technique, recently developed at ORNL, was used to capture the complex creep deformation in the high-temperature environment. This new creep experiment system made it possible, for the first time, to experimentally determine the highly non-uniform creep deformation behavior in different regions.

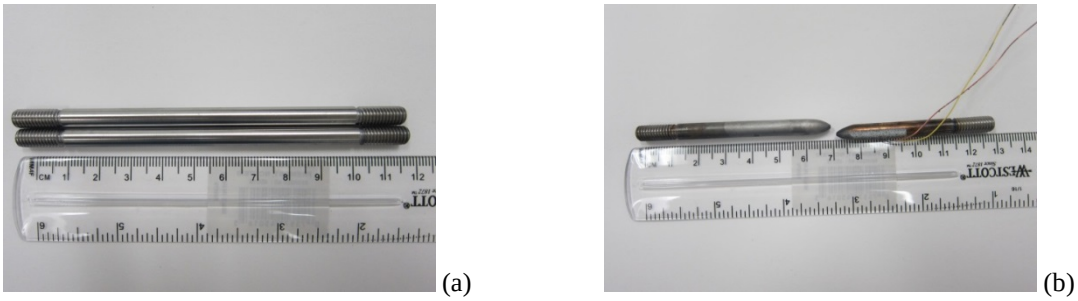

(a) (b)

Figure 20. Tensile creep specimens. (a) Untested specimens. (b) Fractured tensile creep-rupture specimen.

Tensile cross-weld creep-rupture tests were performed using a Gleeble™ thermal mechanical simulator. Two test temperatures were chosen, 550 and 650°C, which are typical use temperatures for nuclear structural materials application. The sample was heated to 550 or 650°C at 5°C/s, and a constant stress of 100 MPa was applied during the creep test.

The sample tested at 650°C failed after 16 hours at temperature. The broken specimen is shown in Figure 20b. The failure location was in the HAZ. Figure 21a shows the creep strain distribution across the sample from the DIC measurement five minutes before the final fracture. It is clear that the creep deformation in the cross-weld specimen is highly non-uniform. Considerable strain concentration occurs in the HAZ, exceeding 12% before final fracture. The high-temperature DIC measurement also revealed that the SZ had much lower creep strain, and in fact was even lower than the base metal creep strain. This is an important finding as it suggests the feasibility of using friction stir welding to improve the creep resistance of the weld region.

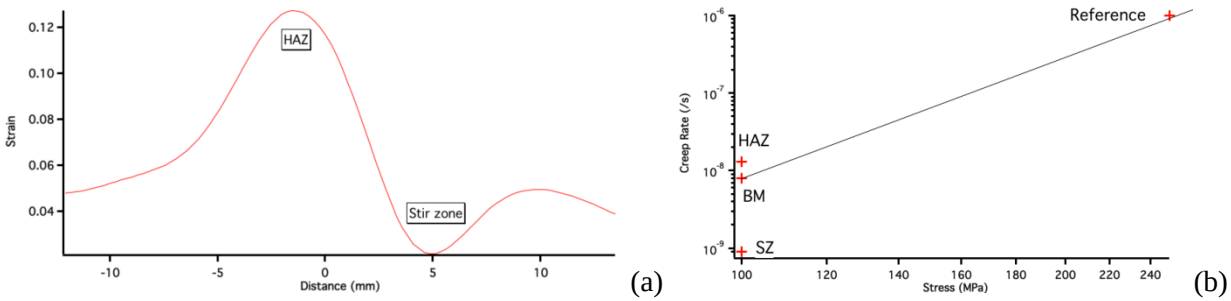

Figure 21. Creep properties of FSW material. (a) Traverse creep strain distribution of the sample tested at 650°C before fracture. (b) Stress vs. strain rate for different regions of the friction stir weld, 550°C.

The stress-rupture test at 550°C was stopped at 89 hours. The overall deformation of the specimen was very small and different regions of the specimen had different creep rates. As shown in Figure 21b, the creep rate of BM, HAZ and SZ are 2.9×10^{-5} /h, 4.8×10^{-5} /h and 3.4×10^{-6} /h, respectively. The most striking feature of the test was that the creep strain in the SZ was significantly lower than any other part of the specimen.

FSW-induced material behavior in thermal-mechanical coupled computer modeling. A thermal-mechanical coupled FSW model was set with 3D Computational Fluid Dynamics (CFD), reported in a previous report. In this period, fundamentals of thermal-mechanical conditions, such as temperature, flow and strain, in FSW of ODS and RAFM steels were studied.

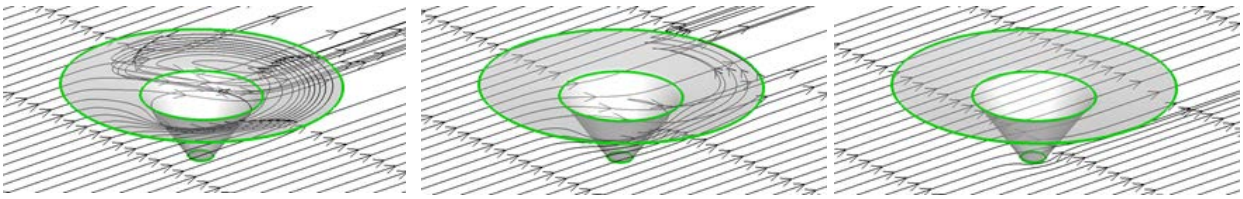

(a) 1 mm underneath shoulder **(b) 3 mm underneath shoulder** **(c) 6 mm underneath shoulder**

Figure 22. Flow pattern predictions by CFD computer modeling (Advancing side on the right).

By releasing marker materials at different heights during FSW, the material flow pattern is visualized by flow paths shown in Figure 22. From Figure 22, it is clear that material on the advancing side flow up and towards the retreating side, while material on the retreating side flow down and towards the advancing side. This flow path characterization from the computer modeling matches the FSW joint cross section materials flow pattern observation showed in Figure 17.

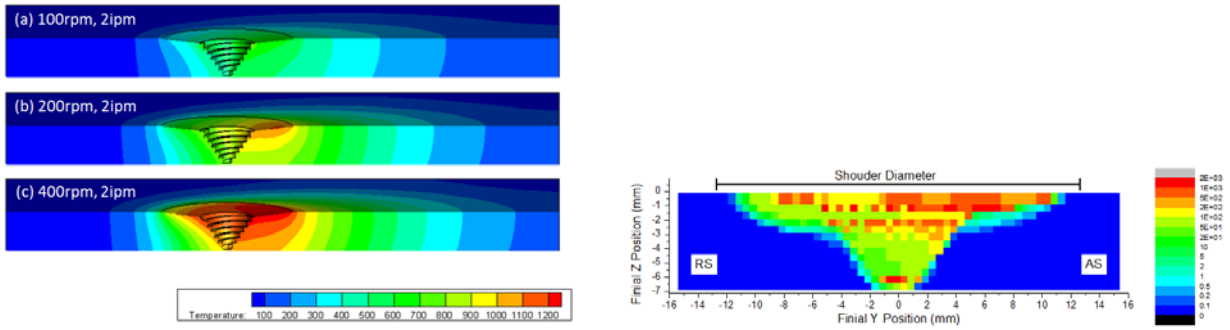

(a) (b)

Figure 23. Temperature and strain distributions from coupled computer model. (a) Temperature fields with different welding parameters. (b) Plastic strain and peak temperature distribution at a cross section in FSW.

The FSW temperature distributions are obtained from modeling results and are shown in Figure 23a. From Figure 23a, it is obvious that the welding temperature for 400 rpm FSW is higher than the austenite phase transformation temperature while that for 100 rpm FSW processes is around the austenite phase transformation temperature for the modeled material, EUROFER 97 RAFM steel (A_{c1b} = 820 °C and A_{c1e} = 890 °C). In the FSW operation, the peak temperature is mainly determined by welding power input, which is mainly determined by FSW tool rotation rate. From the previous experimental results, martensitic was the major grain microstructure for a 400 rpm condition FSW SZ, and partially martensitic microstructure was observed for a 100 rpm condition FSW SZ. The modeling results of FSW temperature fields help understand the reason behind those experimental results.

Fundamentally, the FSW joint properties are highly depended on the thermal – mechanical history during the welding process, but lots of the thermal – mechanical information will not show after the FSW because of materials recovering and recrystallization. Based on the numerical simulation development, the thermal-mechanical history of material deposited in the weld is studied by particle tracing to obtain material deformation facts. The distribution of plastic strain and peak temperature at a FSW joint cross section is shown in Figure 23b. It is clear that plastic strain is unevenly distributed inside the SZ, which explains the SZ grain size and microstructure dissimilarities in the metallographic study.

FUTURE WORK

We have successfully completed this project.

4.7 MIXING OF ODS AND 9Cr F/M STEELS IN FSW JOINTS

D.T. Hoelzer (hoelzerd@ornl.gov), L. Tan, W. Tang and Z. Feng

OBJECTIVE

One of the challenges with deployment of advanced dispersion strengthened alloys and steels in components of fusion reactor cores, such as divertor and structural rings, is development of suitable joining technologies that will not degrade the microstructure, mechanical properties and radiation tolerance of these materials in high-temperature, high-dose environments. The objective of this project is to join the advanced oxide dispersion strengthened (ODS) 14YWT ferritic alloy to 9Cr ferritic/martensitic steel by Friction Stir Welding (FSW) and to characterize the solid-state mixing behavior of these dissimilar materials along a tapered angle butt joint.

SUMMARY

Microstructural analysis was conducted on three samples prepared from 5 mm thick plates of the ODS 14YWT ferritic alloy and 9Cr ferritic/martensitic steel (FMS) joined by FSW along an effective angle (taper) of 9.6º relative to the butt joint between the two plates. Three metallographic samples were prepared from the joined plates containing solid-state mixtures of ~80%/20%, ~50%/50% and ~20%/80% volume fraction of 14YWT and 9Cr FMS. The microstructures of the stir zone (SZ) observed by scanning electron microscopy showed no macro-scale pores in the three samples. Complete solid-state mixing occurred in the SZ of the ~50%/50% sample, but mixing only occurred near the top surface region of the joined plates in the ~80%/20% and ~20%/80% samples. The mixing in this region was caused by additional heating due to friction between the shoulder of the rotating pin tool and the two joined plates. The results showed that frictional heating caused very high temperatures in the SZ that led to significant increases in the grain and oxide particle sizes for 14YWT and elimination of prior austenite grain boundaries with refinement of austenite grains, martensite laths and carbides in 9Cr FMS.

PROGRESS AND STATUS

Figure 24 shows the microstructures observed by backscattered electron (BSE) imaging of the three sample locations on the ascending side of the joined 14YWT and 9Cr FMS plates. The BSE images were obtained near the joint between the SZ, thermo-mechanically affected zone (TMAZ) and the bottom supporting 9Cr FMS plate. For the samples with solid-state mixing of ~80%/20% and ~50%/50% (Figure 24a and Figure 24b), the SZ consists mostly of 14YWT with multiple protrusions extending downward into the supporting 9Cr FMS plate and a clear demarcation in contrast along the interface between the SZ and TMAZ of 14YWT. These protrusions indicate that solid-state mixing occurred between 14YWT and 9Cr FMS and result from the time elapsed behavior of mixing that occurs as the pin tool traveled along the tapered angle butt joint. The finger-like pattern suggests that large volume sections of 14YWT and 9Cr FMS detached and then flowed in spiral motion until being forged in alternating sections as the pin tool travel progresses. For the sample with solid-state mixing of ~20%/80% (Figure 24c), the SZ consists of 9Cr FMS with little contrast variation along the interface with the TMAZ. The vertical crack defines the gap between the butted plates of 14WYT and 9Cr FMS that were not joined by the spinning pin tool. However, the two plates were joined near the top surface of the sample due to additional heating caused by the shoulder of the rotating pin tool.

Figure 25 shows BSE images at higher magnifications of the microstructures on the ascending side of the samples with solid-state mixing of ~80%/20 and ~20%/80%. The results for 14YWT (Figure 25a) for the ~80%/20% sample indicated that significant grain size coarsening of 5-10 times occurred in the SZ compared to the adjacent TMAZ. In addition, the 2-5 nm size Y-, Ti- and O-enriched nanoclusters present

in 14YWT also coarsened significantly to sizes ranging from ~50 to ~350 nm. At low magnification, the microstructure of 9Cr FMS (Figure 25b) for the ~20%/80% sample appears featureless with a low number density of small pores. The BSE image of the SZ at high magnification (insert in Figure 25b) indicates that the prior austenite grain boundaries and lath structure are not discernable and no carbide particles are visible. These results indicate that very high temperatures were reached in the SZ during passage of the rotating pin tool causing dynamic recrystallization of the microstructure in 14YWT and complete austenization and dissolution of carbides in the microstructure followed by formation of smaller martensite lath packets and precipitation of carbides in 9Cr FMS.

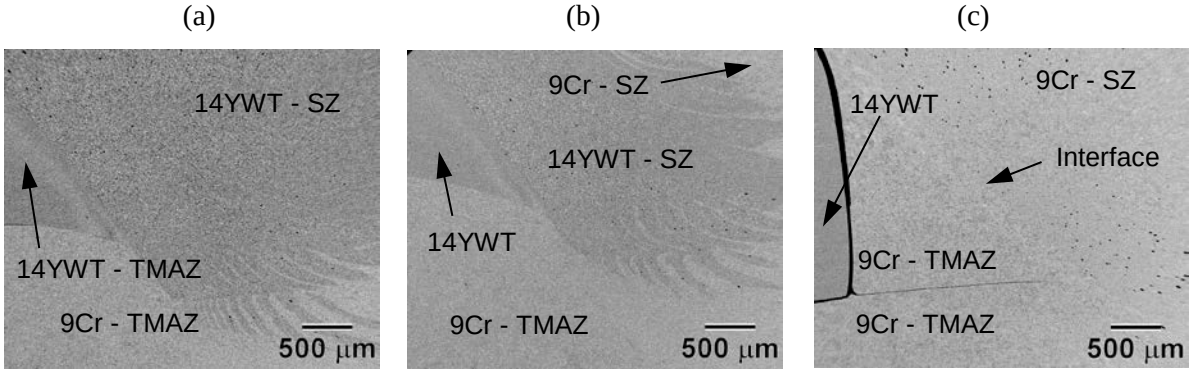

Figure 24. BSE images at very low magnification showing the microstructures on the ascending side of joined plates of 14YWT and 9Cr FMS with solid-state mixing of (a) ~80%/20% (b) ~50%/50% and (c)~20%/80% (14YWT/9Cr FMS).

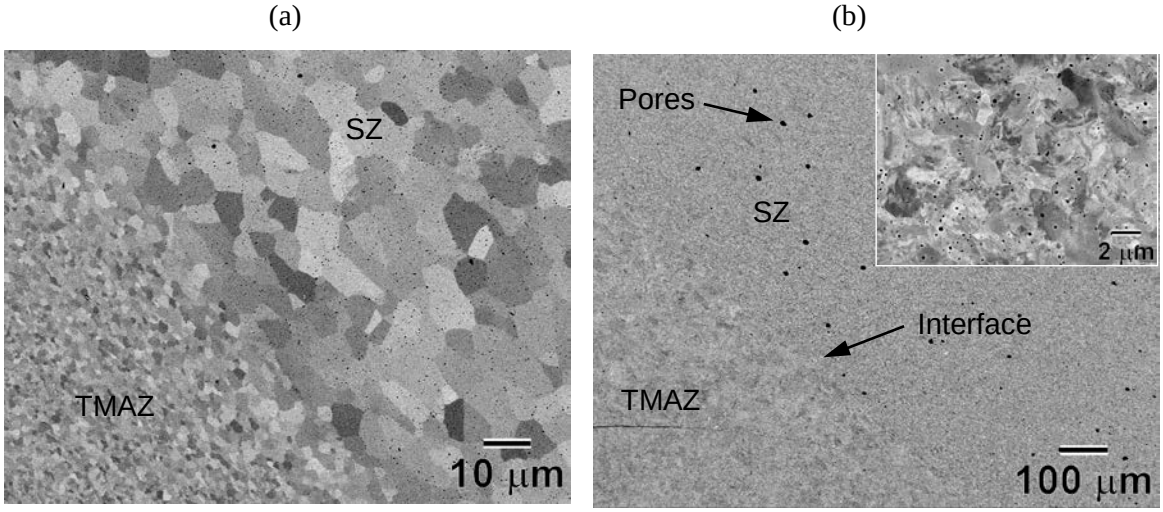

Figure 25. BSE images showing the interface regions between the SZ and TMAZ on the ascending side of (a) 14YWT in the ~80%/20% sample and (b) 9Cr FMS in the ~20%/80% sample (14YWT/9Cr FMS). Insert in (b) shows SZ of 9Cr FMS at high magnification.

FUTURE PLANS

Additional microstructural studies are required on the samples prepared from three locations along the tapered angle butt joint to improve the understanding of solid-state mixing behavior between dissimilar materials to ensure overall better integrity of butt joints. Additional joints are required to optimize the FSW parameters in order to lower the overall temperature during FSW, yet still achieve a defect-free butt joint between 14YWT and 9Cr FMS.

4.8 LIQUID METAL COMPATABILITY IN FLOWING SYSTEMS

S. J. Pawel (pawelsj@ornl.gov), B. A. Pint

OBJECTIVE

The objective of this task is to identify potential structural materials having sufficient compatibility with flowing Pb-Li eutectic that the maximum metal temperature for operation can be increased to improve overall system efficiency.

SUMMARY

A thermal convection loop (TCL) fabricated using dispersion strengthened FeCrAl (Kanthal APMT) tubing – known for high strength and creep resistance at elevated temperature and, based on capsule testing, also anticipated to have excellent resistance to Pb-Li – was operated continuously for 1000 h at a peak temperature of 550 ± 1.5˚C and an average temperature gradient of about 116˚C. The resulting liquid metal flow rate was approximately 0.4 m/min. The TCL contained chains of APMT specimens spanning the length of both the hot leg and cold leg to facilitate the compatibility assessment. In the previous reporting period, initial analysis of post-exposure weight change and surface analysis of APMT specimens was documented. In this reporting period, the mechanical properties of the APMT specimens were examined as a function of exposure temperature.

PROGRESS AND STATUS

Figure 26 presents the room temperature yield strength as a function of TCL exposure temperature for each APMT specimen. The approximate temperature of each specimen location was estimated by linear extrapolation as a function of position between thermowell locations at which the temperature was known. For comparison, data are also included for the APMT specimens that did not receive the pre-oxidation heat treatment (8 h in air at 1050˚C) but were placed at a few positions around the loop for comparison exposures. Note that the specimens with the largest weight loss (specimens without pre-oxidation lost a factor of 3-30 more weight than adjacent specimens with pre-oxidation) did not deviate from the pattern of yield strength established by the pre-oxidized specimens.

The most dramatic increase in yield strength occurred for specimens exposed below about 475-500˚C, although the temperature at which the strength increase develops appears to modestly depend on whether specimens were exposed within the cold leg or hot leg (in which there is larger potential for dissolution rather than deposition). Interestingly, the yield strength of as-received APMT specimens (mill-annealed), the pre-oxidized specimens, and the pre-oxidized specimens heat treated for 1000 h at 550˚C in argon was consistently 647 ± 10 MPa for all conditions. These observations suggest that precipitation reactions within the APMT structure, rather than interaction with the Pb-Li eutectic, are responsible for the change in yield strength. This is discussed further in a subsequent paragraph. The data for the ultimate tensile strength (UTS) of the APMT specimens followed the same pattern as that for the yield strength, with nominal UTS values near 862 MPa increasing to about 1207 MPa as the TCL exposure temperature was decreased.

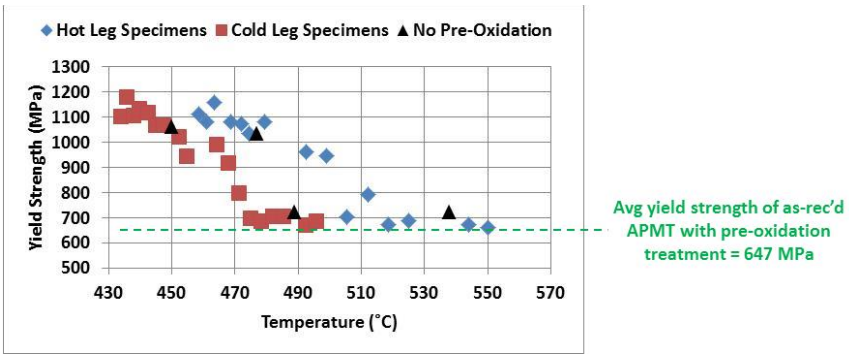

Figure 26. Room temperature yield strength of APMT specimens exposed to flowing Pb-Li eutectic for 1000 h at the indicated temperature. Black triangles are for specimens that did not receive the pre-oxidation heat treatment.

More scatter was observed in the relative ductility data, which is represented by total plastic elongation plotted in Figure 27. Note that the lowest ductility values occurred at temperatures consistent with the concomitant increase in strength, but it is also apparent that very large variations in ductility were observed for adjacent specimens within the TCL (at an exposure temperature difference of only ~ 2˚C). Again, the elongation of as-received APMT specimens (mill annealed), pre-oxidized specimens, and pre-oxidized specimens heat treated for 1000 h at 550˚C in argon was consistently 23 ± 2% for all conditions. It is not clear that 23% elongation observed for sheet material can be expected for all forms and heats of material, because the as-received tubing used to fabricate the TCL was relatively brittle when strained at room temperature (order of 2% elongation or less, but not analytically assessed in specimens of the same size/shape as those exposed within the TCL).

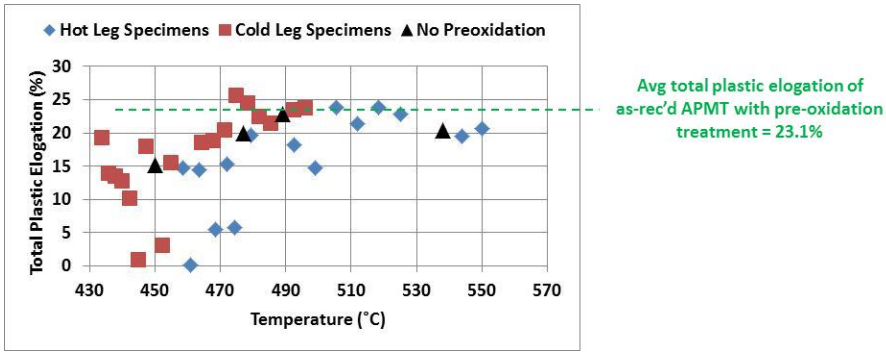

Figure 27. Room temperature ductility (represented by total plastic elongation) of APMT specimens exposed to flowing Pb-Li eutectic for 1000 h at the indicated temperatures. Black triangles represent data for specimens that did not receive the pre-oxidation heat treatment.

Consistent with the above observations of wide variations in ductility even for similar exposure temperature, Figure 28 shows representative views of the fracture surface of post exposure tensile specimens from the TCL hot leg. Note that the specimens on the left side of Figure 28 (458.5 and 461˚C exposure temperatures) were immediately adjacent to each other within the TCL, but exhibited substantially different total plastic elongation despite many similarities in the fracture face features, which include a largely planar fracture surface indicating a predominantly cleavage-style fracture and some amount of secondary cracking. In contrast, the specimen exposed at ~ 505˚C (right, bottom in Figure 28) exhibited a nominal yield strength and a relatively ductile fracture surface indicative of micro-void

coalescence. An even higher exposure temperature (550˚C) yielded a fracture surface looking substantially less ductile, yet the total plastic elongation was not much less than that exhibited at 505˚C.

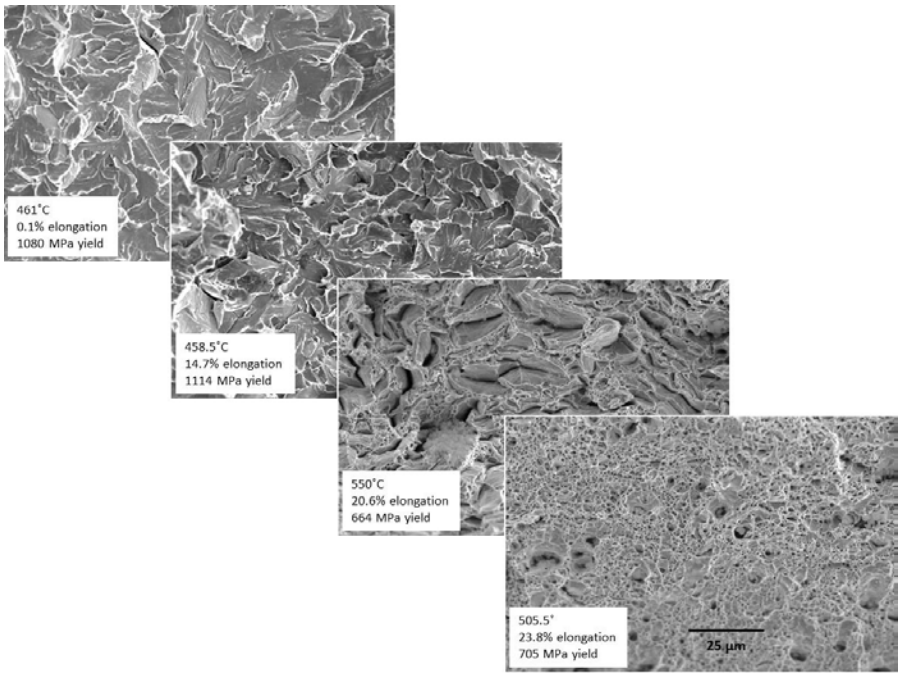

Figure 28. Post-exposure fracture surfaces of APMT miniature tensile specimens. Exposure temperature within the hot leg, total plastic elongation, and yield strength are given; each image at the same magnification.

The observation that the mechanical properties of APMT change substantially with exposure temperature – despite the fact that the weight change and metallography data suggest very little interaction with Pb-Li – indicates that embrittling precipitation within the APMT results from time-at-temperature reactions independent of the environment. An additional experiment was conducted to examine potential mechanical property changes as a result of 1000-h exposure in argon (within a quartz capsule) for comparison with the Pb-Li exposures. The results are summarized in Figure 29. Clearly, the change in mechanical properties with extended time-at-temperature below about 490˚C is independent of compatibility with Pb-Li, and appears consistent with something akin to "475˚C embrittlement" observed within some grades of stainless steels, which involves composition-dependent precipitation of brittle Cr- and/or Mo-rich phases throughout the structure. Transmission electron microscopy of selected specimens exposed in argon for 1000 h at each of 450, 500, and 550˚C did not isolate or identify particular differences in the few precipitates large enough to examine, but the lowest temperature specimens exhibited a "breakdown" in the regular distribution of Fe and Cr into clusters representing precursors of the alpha-prime phase known to embrittle these alloys.

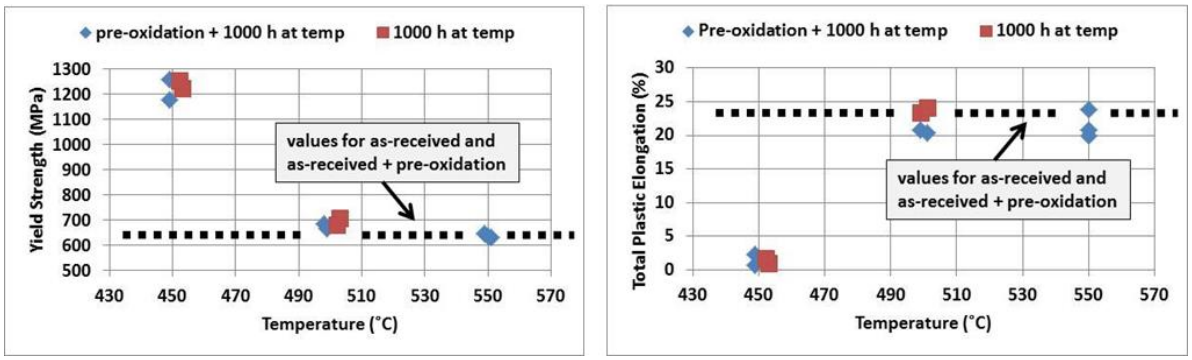

Figure 29. Yield strength (left) and total plastic elongation (right) for APMT specimens heat treated in argon in sealed quartz tubes for 1000 h at the indicated temperatures. [Actual treatment temperatures were 450, 500, and 550˚C; data staggered slightly on plot for clarity of presentation.] The pre-oxidation treatment was 8 h in air at 1050˚C, and in selected cases this treatment was performed prior to the subsequent heat treatment for 1000 h in argon. Tensile tests performed at room temperature following exposure in the TCL.

It should be noted that APMT does not possess the physical/mechanical properties required for fusion materials service and is not being considered as a candidate alloy, but it is available in tubing and several other forms necessary to fabricate a TCL. It was evaluated in this experiment as a surrogate for potentially compatible materials under development but not yet readily available.

FUTURE PLANS

Future work will include completion of the fabrication of two additional APMT thermal convection loops with attendant specimens and components. It is anticipated that the next TCL will be operated similarly to the prior experiment (commercially pure Pb-Li eutectic, 1000 h duration, ~ 116˚C temperature gradient) except that all temperatures around the loop will be raised by 50˚C.

5. CERAMIC AND COMPOSITE MATERIALS

5.1 FOA – DEVELOPMENT OF SiC JOINING TECHNOLOGIES FOR FUSION

Y. Katoh (katohy@ornl.gov), T. Koyanagi, J.O. Kiggans, L.L. Snead, T. Hinoki (Kyoto University), C.H. Henager, Jr. (PNNL,) M. Ferraris (Politecnico di Torino),C.A. Lewinsohn (Ceramatec Inc.), and S. Grasso (Queen Mary University)

OBJECTIVE

This project is developing radiation-tolerant joining technology for SiC materials. The main tasks are

- Process development to fabricate robust SiC joints,
- Development of test methods to determine the strength of ceramics joints, and
- Irradiation experiments to evaluate and understand the radiation tolerance of SiC joints.

SUMMARY

- Process optimization has been conducted for SiC joint formed by a pressure-less transient-eutectic (TEP) process. The limited secondary phase network in the bonding layer was demonstrated, which is a key for achieving excellent irradiation resistance.
- Specimen size effects on torsion tests were investigated for development of a new ASTM standard test method to determine shear strength of ceramics adhesive joints.
- Irradiation tolerance of 10 types of SiC joints was investigated at 500 and 800°C for neutron exposures to 3 dpa. All types of tested joints retained their strength after irradiation unless the joint contained impurity elements or significant second phases formed during the joining process.

PROGRESS AND STATUS

Process development of new pressure-less jointing methods:

In the previous year, the feasibility of new pressure-less joining processes using TEP sintering SiC nano-powder was demonstrated. This year process optimization of the TEP joining was conducted. The effects of processing feedstock such as sintering additives and binder on the joint microstructure were investigated. Increased amounts of the sintering additives (up to 10 wt.%) effectively reduced micro-pores in the bonding layer (Figure 30) without forming a network of the secondary phases. Controlling second phases in the bonding layer is considered to be a key for irradiation tolerance. Use of reduced amount of binder is effective in obtaining relatively dense microstructures because outgassing limitation during joining increases the binder residue. A journal paper on the development of pressure-less TEP joining has been submitted and is under review.

Test method development for shear strength evaluation of ceramics joints:

Our previous work revealed that a torsional shear test is a promising technique to evaluate strength of ceramics joints and is useful for testing irradiated material. Further development of the torsional shear test was conducted this year; specimen size effects on the test were investigated, utilizing brittle ceramics joints. This work is important because miniature specimens are used in the irradiation experiments. Three different sizes of SiC-to-SiC brittle joint specimens were prepared for torsional shear testing; the machined hourglass test specimens have necks of 5, 10, or 15 mm diameter in the bonding plane. Uniformity of the bond quality was confirmed by acoustic scanning microscopy prior to machining. Pure

shear failure was observed for all the specimens, showing that there was no obvious size effect on the fracture appearance, Figure 31a. The size effect on the strength was apparently insignificant, though the large scatter in the torsional shear strength make detailed discussion on the specimen size effect a challenge, as shown in Figure 31b.

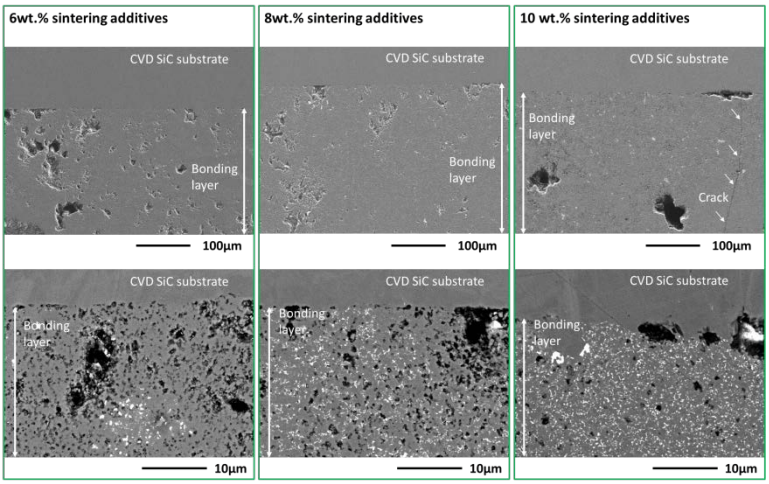

Figure 30. Backscattered electron images of TEP joints fabricated with different amount of sintering additives.

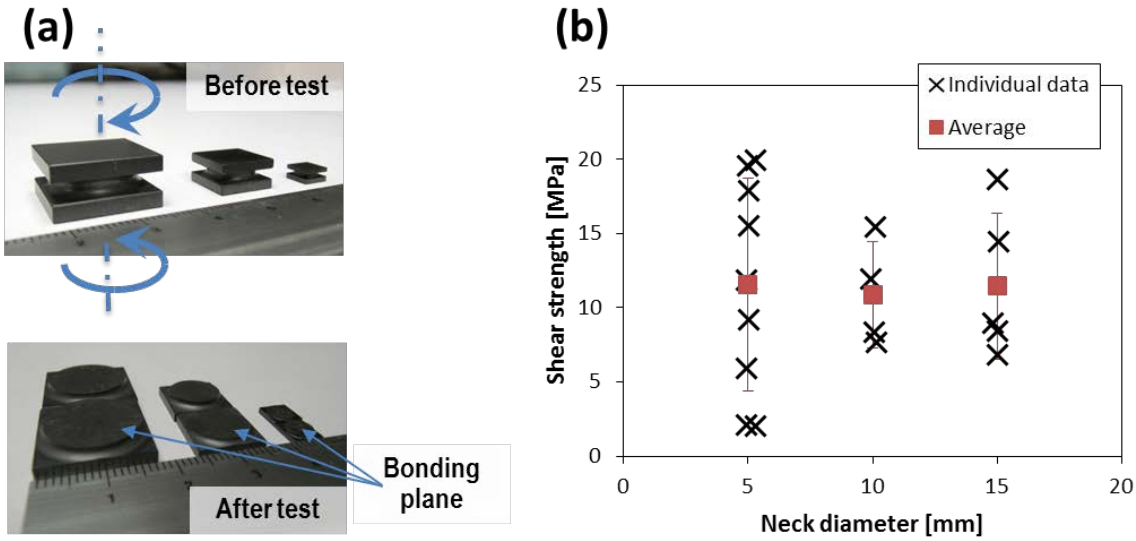

Figure 31. Appearance of three sizes of SiC joint specimens before and after torsion tests (a), torsional shear strength of SiC joints with different specimen sizes (b).

Irradiation resistance of various SiC joints:

The High Flux Isotope Reactor irradiations of newly developed joints were conducted in FY2014. In addition, high dose irradiations were conducted for joints that had demonstrated irradiation tolerance joint after low neutron fluence exposures. Post irradiation experiments for newly developed joints were mainly conducted in this year. The test specimens include 10 types of SiC joints: Mo diffusion bond (Mo diff), Ti

diffusion bond (Ti diff), pressure-less sintered Ti-Si-C joints (Ti-Si-C P/L), modified Ti-Si-C MAX-phase bonding (Ti-Si-C Mod), Ti spark plasma sintered joints (Ti SPS), TEP joints using a slurry method (TEPs), TEP joints using green tape (TEPt), pressure-less TEP joints (TEP P/L), $CaO–Al_2O_3$ glass ceramics joints (CA), and Al-Si-C-O brazed joints (C-tec Braze). All joints were prepared at Oak Ridge National Laboratory or by outside collaborators. The irradiation conditions were 500°C/3 dpa and 800°C/3 dpa. The torsional shear strength of those joints before and after irradiation is summarized in Figure 32. Significant strength degradation was found in TEPs and TEPt joints, which were irradiation tolerant in the previous study. Microstructural observation indicates that this was likely caused by significant amounts of unexpected impurity elements or significant second phase formation, which was not observed in the previous work. Regarding the other joints, strength degradation was insignificant and they were irradiation tolerant, at least for this low neutron fluence.

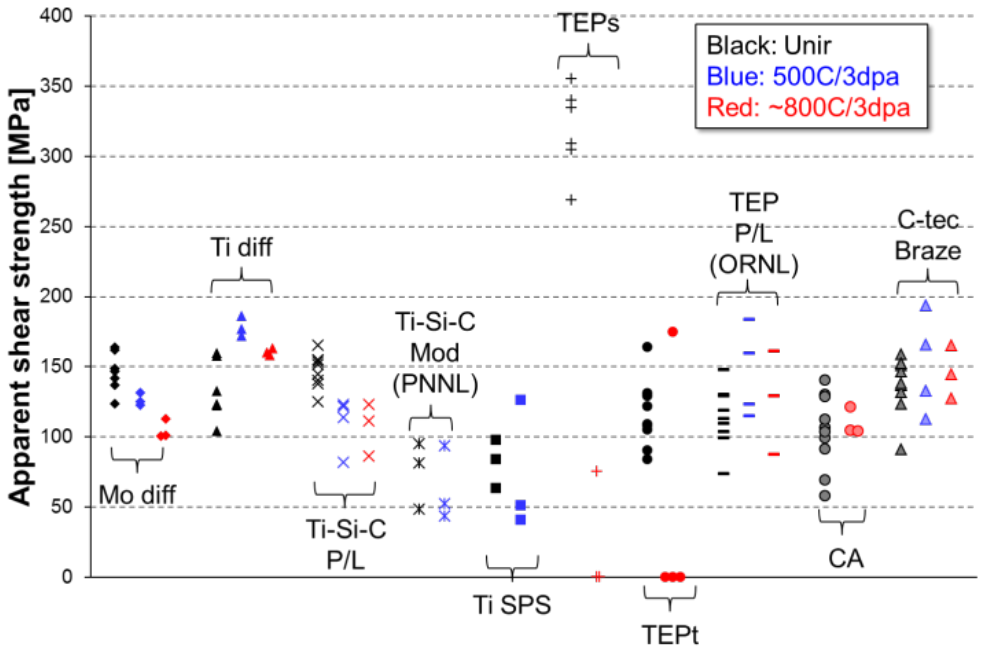

Figure 32. Apparent shear strengths of various SiC joints before and after neutron irradiation.

FUTURE PLANS

Joining process development: A paper on the processing study of pressure-less TEP joining will be completed.

Test method development: Further investigation of specimen size effects on the torsion test will be investigated. The Weibel statistical approach will be used for clarifying the size effects on the joint strength. This task will contribute to the development of an ASTM testing standard.

Irradiation effects: High dose neutron irradiation effects on the SiC joints will be investigated using torsional shear tests and microstructural observations.

5.2 IRRADIATION CREEP OF NUCLEAR GRADE SiC MATERIALS

Y. Katoh (katohy@ornl.gov), T. Koyanagi, K. Ozawa, L.L. Snead, and T. Hinoki (Kyoto U.)

OBJECTIVE

The goal of this research is to investigate the irradiation creep of nuclear grade SiC, which often defines the design limit stress for thermo-structural fusion components. The main focus this fiscal year was on the irradiation creep of nuclear grade generation III SiC fibers.

SUMMARY

- The measurement and analysis of creep strain of irradiated SiC fibers was completed. Microstructural observation confirmed that irradiation under initial applied stress up to ~1 GPa did not introduce cracking in the SiC fibers.
- The apparent creep rate of the four types of nuclear grade SiC fibers is very small, ~1×10^{-7} [dpa^{-1} MPa^{-1}] at 1 to 10dpa, but slightly higher than that of chemical vapor deposited (CVD) SiC. The effect of material quality on the creep rate, including grain size and presence of secondary phases increased with increasing irradiation temperature.

PROGRESS AND STATUS

Systematical investigations of irradiation creep of SiC materials have been achieved by development of an evaluation method for creep strains in small specimens and development of irradiation creep rabbit irradiation capsules at Oak Ridge National Laboratory. The recent work revealed the irradiation creep behavior of high-purity CVD SiC materials up to 30dpa; the creep behavior can be explained by swelling-creep coupling in the transient region and secondary creep at doses more than ~1 dpa. This fiscal year effort mainly focused on irradiation creep of nuclear grade SiC fibers. Four types of fibers: Hi-Nicalon Type S, Tyranno SA3, isotopically-adjusted Sylramic and Sylramic-iBN fibers were investigated. Figure 33 shows the appearance of surfaces of Hi-Nicalon Type S fibers before and after the irradiation creep experiment. The observations revealed that irradiation under applied stress did not introduce cracking on the fiber, though there was minor surface modification. Cracking was also absent on the surfaces of the other three fiber types for all irradiation conditions, even when the initial applied stress was greater than 1 GPa.

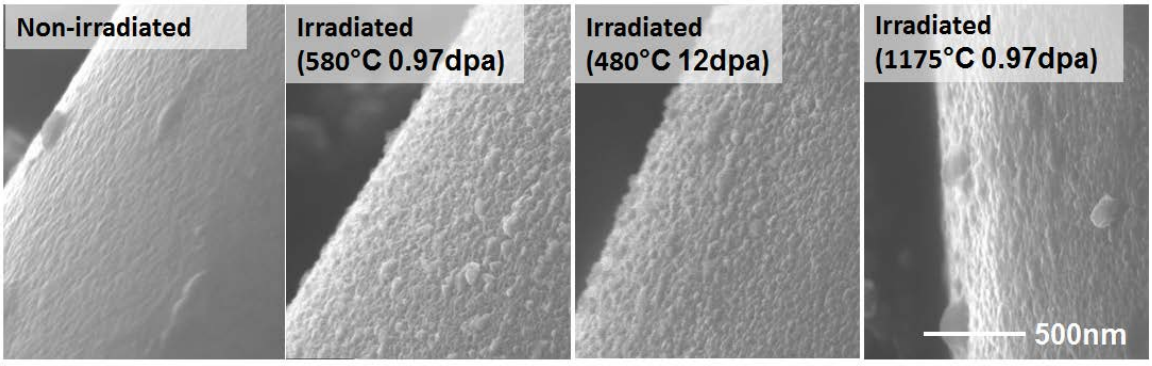

Figure 33. Secondary electron images of surface of Hi-Nicalon Type S fiber before and after the irradiation creep experiment.

The creep strains of the irradiated specimens have been measured with more than 200 raw data points obtained in the fiber creep experiments. The apparent creep rates normalized by applied stress were analyzed and are shown in Figure 34. The figure also includes data points for nano-powder sintered SiC ceramics and SiC composite fabricated by the nano-infiltration transient eutectic phase process. In addition, the trend line for CVD SiC is shown. The creep rate was on the order of 1×10^{-7} [MPa dpa]$^{-1}$ at 1 to 10 dpa for all the fibers. This creep rate is comparable to the rate for bulk CVD SiC, sintered SiC, and SiC composite, and more than one order of magnitude smaller compared to metallic materials. Further analysis revealed the effects of material quality on the creep behavior. A small grain structure and the presence of secondary phases in the fibers tend to result in an increase in the creep rate with increasing irradiation temperature. Ultrafine-Grained Hi-Nicalon Type S fiber was less creep resistant at ~500 °C than the other fibers.

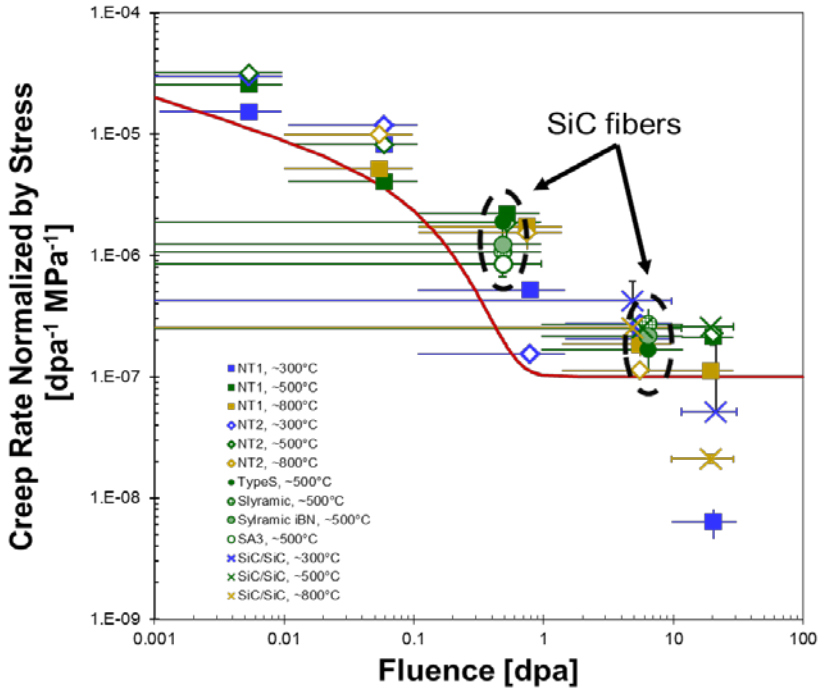

Figure 34. Apparent creep rates of various SiC materials, including SiC fibers, sintered SiC ceramics, and SiC composites. The horizontal error bars is uncertainty in analytical processing. The red line shows the trend of reference CVD SiC.

FUTURE PLANS

Advanced characterization methods such as synchrotron X-ray diffraction will be conducted to assist in developing a detailed understanding of the creep mechanism. The recent high-dose irradiation creep experiment results, including the strain measurement, the analysis of creep rate, the investigation of material effects, and the microstructural observation will be summarized to understand and explain the irradiation creep of SiC ceramics.

5.3 MICROSTRUCTURES AND MECHANICAL PROPERTIES OF IRRADIATED SiC

Y. Katoh (katohy@ornl.gov), T. Koyanagi, L.L. Snead, T. Nozawa (JAEA) and K. Ozawa (JAEA)

OBJECTIVE

The objective of this task is to obtain further understanding of the effects of high neutron fluence irradiation on mechanical properties and microstructures of SiC and SiC fiber reinforced SiC matrix (SiC/SiC) composites. This information will assist in the evaluation of SiC materials for fusion structural applications.

SUMMARY

- Post-Irradiation evaluation of Hi-Nicalon Type S fiber SiC/SiC composite neutron irradiated to ~100 dpa were conducted. The degradation of room temperature ultimate flexural stress appears to saturate at fluence below 70 dpa at 300 and 500°C.
- A study of high dose neutron irradiation effects on newer generation nuclear grade SiC fiber reinforced SiC matrix composites was started employing a series of new High Flux Isotope Reactor (HFIR) rabbit capsules. The irradiation matrix was designed to achieve maximum neutron fluence above 100 dpa for a range of irradiation temperature from ~300 to ~1000°C.
- The mechanistic understanding of irradiation creep of high purity SiC irradiated to more than 10 dpa was obtained through microstructural observation; the synergetic effect of anisotropic dislocation formation and growth of the dislocation loops contributed to creep strain at high neutron doses.

PROGRESS AND STATUS

High Dose Neutron Irradiation Effects on Strength of SiC/SiC composite:

The previous work in the Department of Energy Japan Atomic Energy Agency collaboration has accomplished neutron irradiations to greater than 70 dpa in HFIR, and provided an extended understanding of effects of high does neutron irradiation on thermomechanical properties of early generation nuclear grade Hi-Nicalon Type S SiC/SiC composite with SiC-pyrolytic carbon (PyC) multilayer interphase. This fiscal year the irradiation to ~100 dpa was completed and the post-irradiation examination was conducted.

Figure 35 shows room temperature stress-strain curves of the SiC/SiC composites before and after irradiation at ~300 and ~500°C to 100 dpa. Significant degradation of ultimate flexural stress and loss of fracture strain were found at 300°C. The room temperature fracture strain increased, but the flexural strength was reduced for irradiation at 500°C. These trends were also observed in the SiC/SiC irradiated to 70 dpa. Further analysis indicates that the degradation of ultimate flexural stress appeared to saturate below 70 dpa.

Because of the significant strength degradation that resulted from low-temperature and high-dose irradiation, additional high-dose irradiation experiments on newer generation nuclear grade SiC/SiC with different SiC fibers and different interphase was initiated to seek SiC/SiC composites that are irradiation tolerant for neutron exposures above 100 dpa. Three types of SiC/SiC composites were fabricated; SiC/SiC composites with PyC coated Hi-Nicalon Type S fibers, Tyranno SA3 fibers, and Ultra SCS fibers. Note that the carbon interphase is different in these experiments than in the old high-dose experiments. The irradiation matrix was designed to achieve the maximum neutron fluence above 100 dpa for a range of irradiation temperatures from ~300 to ~1000°C. Twelve rabbit capsules containing three

types of SiC composites and high-purity monolithic SiC were built. Irradiations of all capsules started in HFIR Cycles 457 or 458. Properties to be evaluated after irradiation include dimensional stability, mechanical properties, physical properties, and microstructures. Appearance of the three types of SiC/SiC composite specimens are shown in Figure 36.

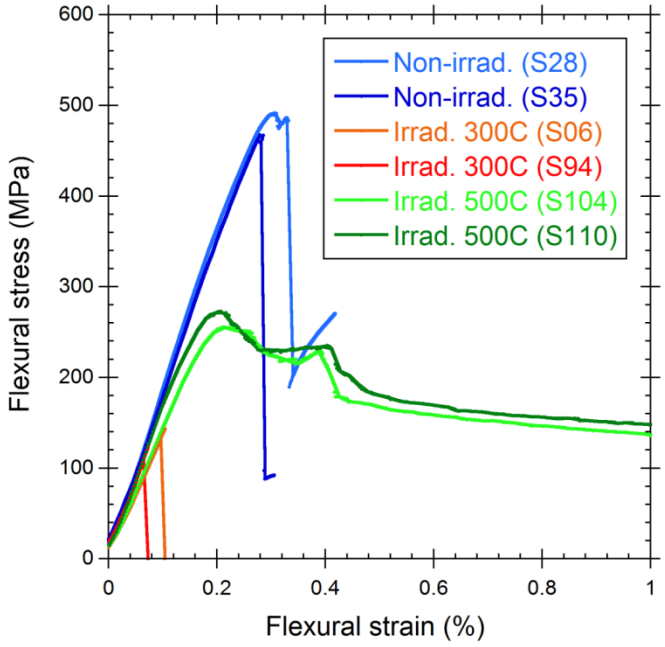

Figure 35. Stress-strain curves during room temperature flexural tests of SiC/SiC composites with and without irradiation to 100 dpa.

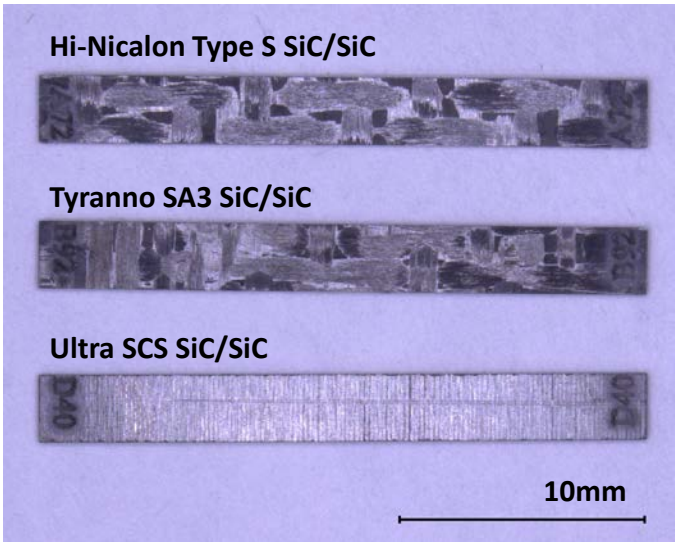

Figure 36. Appearance of SiC/SiC composite specimens for high-dose irradiation experiments.

Microstructural Evolution in SiC during High Dose Irradiation Creep:

The irradiation creep behavior of SiC materials has been systematically investigated up to 30 dpa utilizing a series of bend stress relaxation experiments developed at Oak Ridge National Laboratory. In the last period, extensive understanding of the stress effect (creep behavior) was pursued by microscopic observation of irradiation-induced interstitial loop defects in chemical vapor deposited (CVD) SiC irradiated at 300 and 800°C to ~10 dpa. In this period, this work was extended to higher neutron fluence (30 dpa) to evaluate the secondary creep mechanism which is dominant above ~1 dpa.

Figure 37 shows transmission electron micrographs of dislocation loops formed in CVD SiC during irradiation creep experiments at 750°C to 10 and 30 dpa. The pair of images for the same irradiation condition were taken in the same location, but taken using different streaks indicated in the diffraction pattern. This imaging technique enables comparison of the loop formation on {111} planes closely perpendicular to the stress axis (image A and C) and parallel to the stress axis (image B and D). A larger number of loops formed on the plane perpendicular to the stress axis for both irradiation conditions. Statistical analysis revealed that the average loop size increased by ~3 nm for all {111} planes as the irradiation fluence increased from 10 to 30 dpa. The synergetic effect of the anisotropic microstructural evolution with applied stress and the loop growth gives a phenomenological understanding of the creep strain in the secondary creep region, based on the classic theory of irradiation creep; the stress induced preferential nucleation and absorption mechanisms. Because the dislocations in Figure 37 accounts for only ~20% of the creep strain, a quantitative understanding of irradiation creep will be attempted utilizing advanced characterization methods in next period.

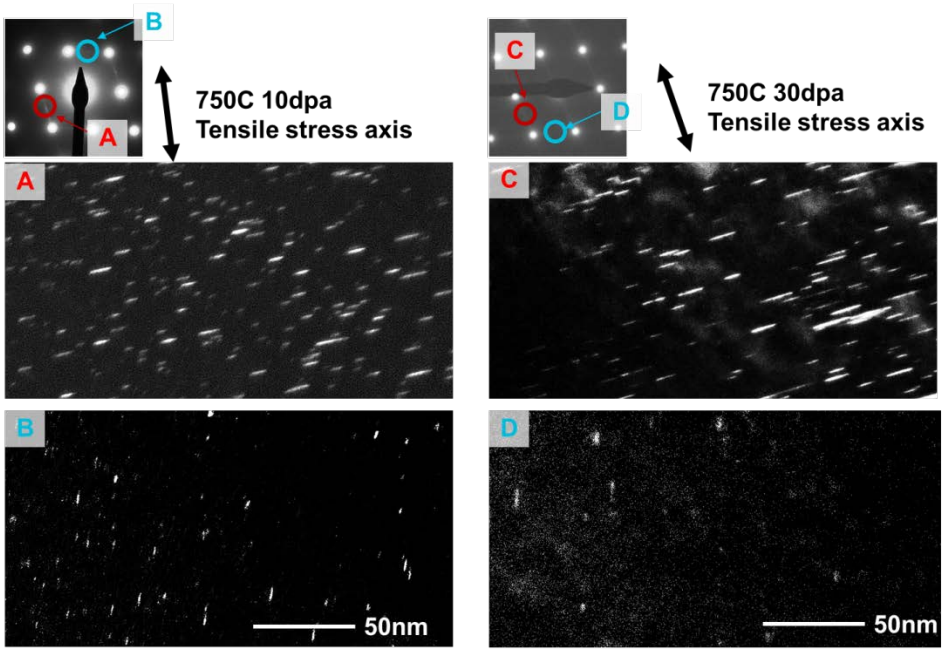

Figure 37. Transmission electron micrographs of dislocation loops formed in SiC under irradiated at 750°C to 10 and 30 dpa. The images were taken using streaks around the diffraction spots.

FUTURE PLANS

Post-irradiation evaluation of SiC/SiC composites irradiated to 100 dpa:

Further investigation of the mechanical properties and microstructures will be conducted. The work will mainly focus on understanding the degradation mechanisms based on additional data set. The mechanistic understanding will help to guide design of SiC/SiC composites that are irradiation tolerant up to high doses.

New irradiation campaign for high dose irradiations:

Post irradiation evaluation of material from the new irradiation campaign will start for low dose specimens, depending on activity of the specimens. The irradiation to >10 dpa is scheduled to be completed in Fiscal Year 2016.

Mechanistic understanding of irradiation effects based on microstructure:

Advanced characterization of irradiation produced defects in SiC irradiated with and without applied stress will be conducted utilizing Synchrotron X-ray diffraction for quantitative understanding of the irradiation creep behavior.

5.4 IRRADIATION AND CHARACTERIZATION OF ADVANCED CERAMICS

Y. Katoh (katohy@ornl.gov), T. Koyanagi, M.J. Lance, and N.O. Cetiner

OBJECTIVE

The main objectives in this task are:

- Examination of irradiation tolerance of advanced ceramics for potential use in fusion applications, and
- Evaluating and understanding irradiation effects in ceramics utilizing advanced characterization techniques.

SUMMARY

- Ceramics materials include SiC with various qualities of additives, AlN, TiC, YAG, glassy carbon, Si, MAX phases such as Ti_2AlC, Ti_3AlC_2, Ti_3SiC_2, and ultra-high temperature ceramics including TiB_2 and ZrB_2 were prepared for irradiation. Some irradiations started this fiscal year.
- Irradiation induced structural changes in SiC are investigated using Raman spectroscopy. The presence of carbon clusters is strongly indicated following irradiation to low neutron fluence, changes which cannot be detected by conventional transmission electron microscopy.

PROGRESS AND STATUS

Irradiation of Advanced Ceramics:

This task started this fiscal year to investigate the irradiation tolerance of advanced ceramics for potential fusion applications. Ceramics materials include SiC with various qualities of additives, AlN, TiC, YAG, glassy carbon, Si, MAX phases such as Ti_2AlC, Ti_3AlC_2, Ti_3SiC_2, and ultra-high temperature ceramics including TiB_2 and ZrB_2 were prepared for irradiation. Though these materials are potentially attractive for high temperature use in fusion applications, irradiation effects on them are poorly understood except for the reference SiC. In this period, specimen preparation and irradiation capsule fabrication were followed by the start of some of the irradiations in High Flux Isotope Reactor (HFIR).

Figure 38 shows the schematic image of a HFIR rabbit irradiation capsule and the calculated irradiation temperature distribution of the specimens in a low temperature irradiation capsule. The irradiation capsule was designed to contain 6 mm disc specimens. These disc specimens can be utilized for various characterization measurements, such as evaluation of strength, thermal properties, density, electrical properties, etc. The specimen temperatures vary depending on the material. Therefore, the distribution of actual irradiation temperatures within the specimens will be experimentally determined by dilatometry of 8 SiC temperature monitors designed to be in contact with the disc specimens. The post-irradiation examination will start next fiscal year.

Advanced Characterization of Irradiation Defects in Ceramics:

A quantitative understanding of correlation between microstructures and properties such as swelling and irradiation creep is essential for mechanistic understanding of irradiation-produced changes in fusion materials. However, that is challenging because of difficulty in capturing the properties and behavior of atomic scale defects using conventional investigation methods. To obtain a better understanding of atomic scale defects in irradiated SiC, evaluation using Raman spectroscopy was initiated. Raman spectra can provide information about the crystal structure of SiC, including the polytype, extent of amorphous

bonding and the presence of defects. In addition, both silicon and carbon have strong and distinct Raman peaks which may appear as the SiC structure dissociates.

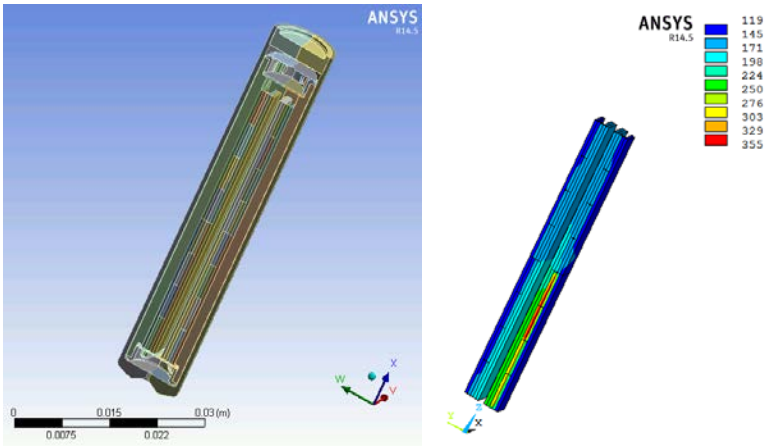

Figure 38. Appearance of an irradiation capsule (left image), and simulated temperature distribution in 6 mm disc ceramic specimens and SiC temperature monitors during irradiation (planned irradiation temperature: ~200°C (right image).

Figure 39 shows Raman spectra of high purity CVD SiC both un-irradiated and irradiated at 380°C to 0.01 dpa. The bonding type for each major peak is indicated, with 3C SiC peaks clearly observed in the as-received material. Following irradiation, three broad bands appear around 200, 1400, and 1600 cm^{-1} in addition to Si-C bonding. These are characteristic of Si-Si (200 cm^{-1}) and C-C homonuclear bonds (D band at 1400 and G band at 1600 cm^{-1}). The important finding is the presence of D and G bands, strongly indicating formation of irradiation induced carbon clusters in SiC, which was not observed using conventional electron microscope imaging. Further analysis will be conducted in the next period to obtain a semi-quantitative characterization of these defects.

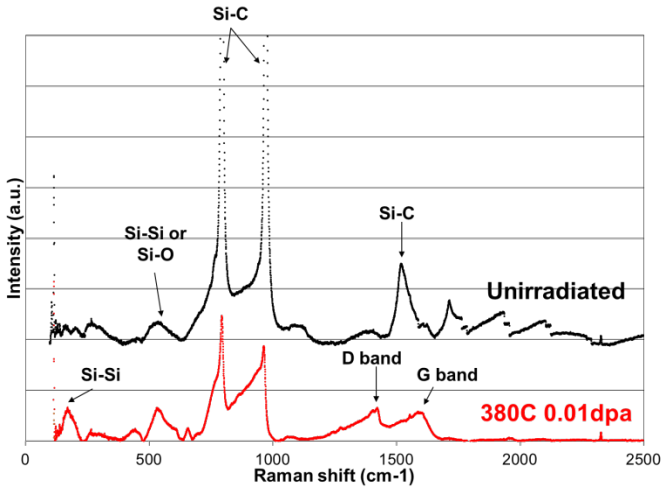

Figure 39. Raman spectra of unirradiated and irradiated SiC specimen. The bond types for the major peaks are indicated.

FUTURE PLANS

Irradiation of advanced ceramics:

The additional irradiations will start in Fiscal Year 2016. Post irradiation evaluation of the ceramics specimens irradiated at low dose and low temperature will be conducted, as allowed by the specimen activity. The irradiation tolerance of various ceramics will be investigated based on dimensional stability, microstructure, and physical property response to the HFIR neutron irradiation.

Advanced characterization:

Characterization of irradiation produced defects using Raman spectroscopy will be further conducted to understand the atomic-scale structure of the irradiated SiC. Additional advanced characterization using positron annihilation spectroscopy and synchrotron X-ray diffraction analysis will be used to investigate atomic scale defects in irradiated ceramics.

6. HIGH HEAT FLUX AND PLASMA FACING MATERIALS

6.1 FABRICATION OF LAMINATED TUNGSTEN STRUCTURES

L. M. Garrison (garrisonlm@ornl.gov) and T. Colling

OBJECTIVE

Tungsten is the leading choice of plasma facing material for future fusion reactors. Fusion reactors beyond ITER must operate at higher power levels and thus the first wall and divertor components will operate at higher temperatures. Because of this, several design concepts replace copper alloys with advanced steels, which require robust tungsten to steel joints. Additionally, for tungsten to be used as a structural component, its fracture toughness must be improved. The goal of this project is to create a tungsten-steel laminate composite that would provide the transition between tungsten and steel in a component as well as improve the fracture toughness compared to tungsten alone.

SUMMARY

Tungsten and steel foils were alternately stacked within a stainless steel container and then hot rolled at 1000°C to approximately 80% reduction of the original height to induce bonding. A cross-section sample of the composite was polished for metallographic analysis, including scanning electron microscopy (SEM) and quantitative elemental analysis. Individual foils were tensile and shear punch tested. An electron backscatter diffraction analysis (EBSD) was performed on the tungsten foils to reveal the texturing.

PROGRESS AND STATUS

The foils were alternately stacked in a stainless steel box, Figure 40a shows the stacking sequence, and then rolled at 1000°C to an overall 80% reduction. A sample of the resulting laminate composite was cut using electric discharge machining, mounted on its side, and polished to reveal the cross section of the layers (Figure 40b-d). Because many cracks were found in Section 1, and the tungsten in Section 3 appears segmented, Section 2 appears to be the most successful.

A region from Section 3 of the composite was analyzed and the results are presented in Figure 41. The line scan goes from the steel phase, through the intermetallic region, into the pure tungsten region, and through to the steel zone on the opposite side. The signal from the alloying elements in the steel, Mo, Mn, and V, is multiplied by 100 in all the following profiles for better comparison. It can be seen that the Mo is enriched near the W layer, but all the other alloying elements in the steel are depleted near the W layer.

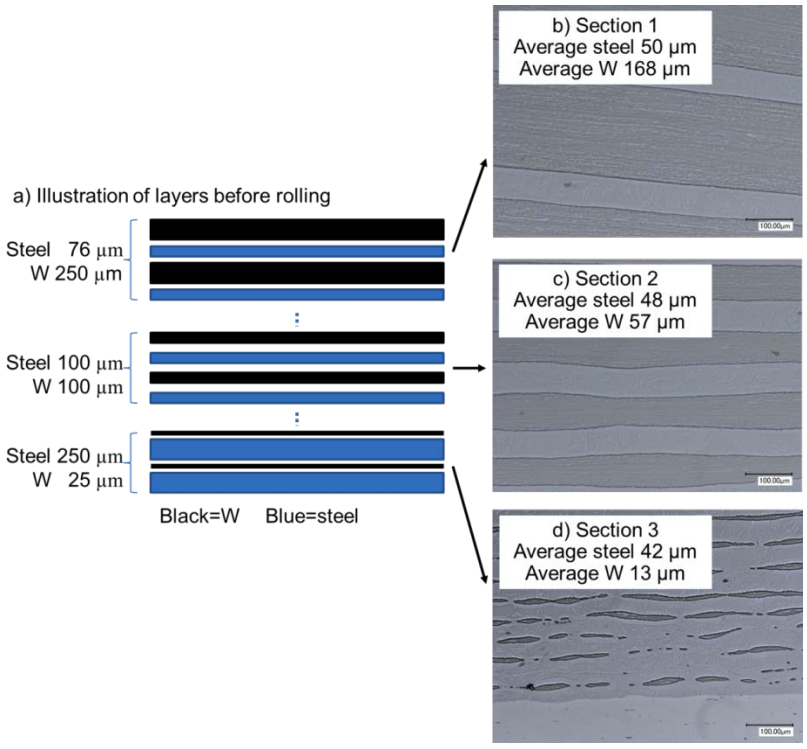

Figure 40. a) Stacking sequence of foils, showing thicknesses before rolling b)-d) SEM images of cross section of laminate after rolling.

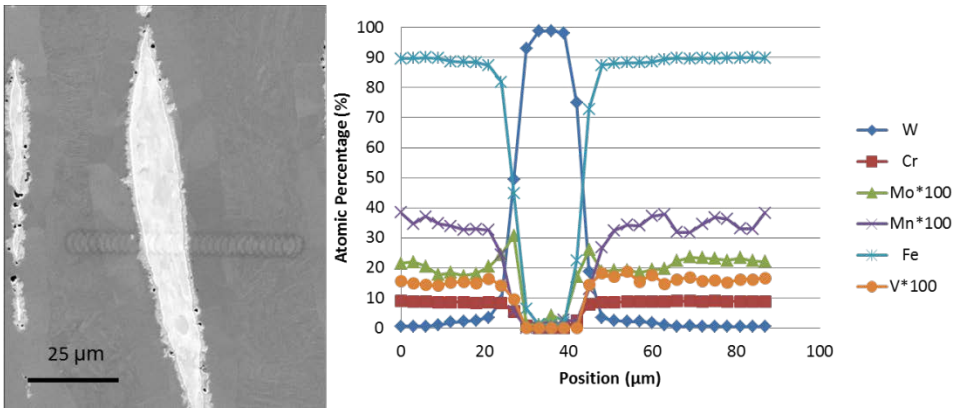

Figure 41. Quantitative line scan from Section 3 of Figure 40 in the tungsten-steel composite.

Figure 41 shows two separate microstructure layers between the base tungsten and the base steel zones, but their elemental composition cannot be differentiated. A more detailed scan is shown in Figure 42. It reveals that the thin, porous layer near the tungsten is composed of near equal amounts of tungsten and iron. Based on the atomic percentages, it is likely that this layer is a W_6Fe_7 phase. Moving into the iron rich intermetallic phase, the tungsten percentage quickly drops to 10-20%. In this detailed view it is more clearly seen that Mo enriches closer to the W layer, while Cr, Mn, and V deplete closer to the W layer.

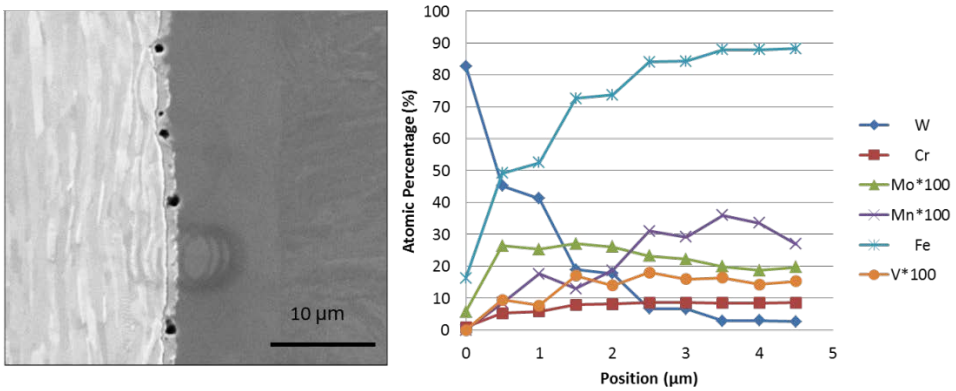

Figure 42. Detailed line scan to identify the composition of the intermetallic phases between the tungsten and steel layers.

Tensile tests were performed on the tungsten and steel foils. The resulting yield strength (YS), ultimate tensile strength (UTS), uniform elongation (UE), and total elongation (TE) are summarized in Table 4. In cases where there was more than one valid tensile test, the values in Table 4 are the average values. For all materials except the 250 µm tungsten foil, the samples cut at 45 degrees to the rolling direction exhibited more total elongation than the samples from the same material cut at 0 or 90 degrees to the rolling direction.

Table 4. Data from tensile tests of steel and tungsten foils.

Material	Nominal thickness	Angle to rolling direction	YS (MPa)	UTS (MPa)	UE (%)	TE (%)
Steel	100 µm	0	999	1070	1.1	3.3
		90	844	1033	1.5	1.9
		45	928	1007	1.5	3.6
	250 µm	0	925	969	0.9	5.1
		90	974	1011	0.9	4.1
		45	871	942	1.2	6.0
Tungsten	25 µm	0	1681	1698	0.2	0.2
		90	1653	1653	0.04	0.05
		45	1574	1695	1.1	1.3
	100 µm	0	2166	2233	0.9	1.3
		90	1479	1479	0.1	0.1
		45	1769	1832	1.0	3.2
	250 µm	0	1826	1883	1.2	4.0
		90	1944	1993	0.6	0.7
		45	1636	1676	0.8	2.7

Shear punch testing was used for the tungsten foils because it can also give information about the ductility of the materials without being sensitive to sample alignment in the holder or to edge effects, which was especially problematic for the thinnest foils in the tensile tests. In the shear punch tests, the medium tungsten foil performed the best with more uniform and total elongation than the two other foil thicknesses (Figure 43).

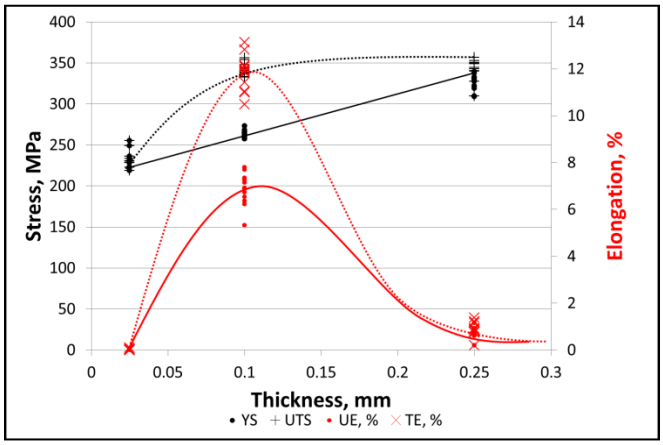

Figure 43. Shear punch results of tungsten foils.

The tungsten foils were electro-polished with a 2 wt.% KOH solution and then examined with EBSD. The thickest foil, 250 µm, does not show strong texturing (Figure 44a). The medium foil, 100 µm, had texture along the 100 to 111 edge of the inverse pole figure (Figure 44b). The thinnest foil, 25 µm, is similar to the 100 µm foil, but with the texture even more toward the 100 corner than the 111 (Figure 44c).

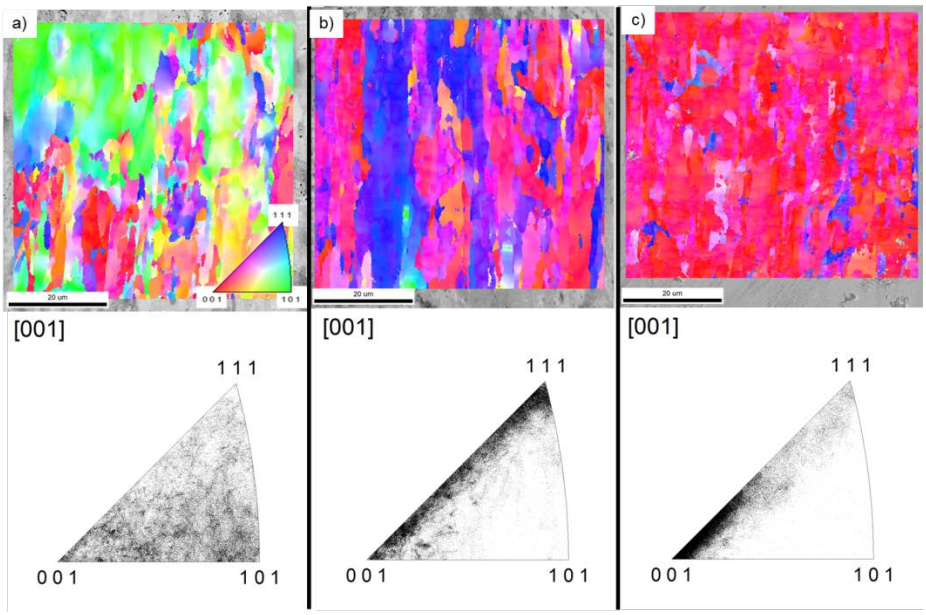

Figure 44. EBSD analysis of the a) 250 µm thick tungsten foil surface, b) 100 µm thick tungsten foil surface, and c) 25 µm thick tungsten foil surface. Rolling direction is vertical on the page.

FUTURE PLANS

The composite will be tensile and shear punch tested to compare the properties to the individual foil properties.

6.2 TUNGSTEN-RHENIUM ALLOYS

L. M. Garrison (garrisonlm@ornl.gov)

OBJECTIVE

Neutron irradiation causes tungsten to transmute to rhenium and also creates point defects. In neutron irradiation studies of tungsten, rhenium rich precipitates have been observed and increases in hardness have been measured. To better understand how additions of rhenium change the microstructure and mechanical properties of tungsten, several tungsten-rhenium alloys were fabricated and will be neutron irradiated.

SUMMARY

Tungsten alloys with 0.043, 0.41, and 2.24 wt.% Re were selected for irradiation in the High Flux Isotope Reactor MFE-RB*-19J experiment. Sample preparation has been completed.

PROGRESS AND STATUS

Five alloys of tungsten with different rhenium additions as well as one pure tungsten control material were fabricated by arc melting. After arc melting, the samples were hot-rolled to approximately 80% reduction. The estimated compositions based on the weight of material used in the arc-melting are listed in Table 5. Evans Analytical Group performed glow discharge mass spectrometry and inductively coupled plasma optical emission spectroscopy on Alloys 2, 4, and 6 to measure the compositions after fabrication (Table 6).

Table 5. W-Re alloy compositions based on feed material used in arc-melting.

Alloy number	Initial Re wt.%
Alloy 1	0.033
Alloy 2	0.165
Alloy 3	0.830
Alloy 4	3.440
Alloy 5	17.700
Alloy 6	0.000

Table 6. Results of glow discharge mass spectrometry and inductively coupled plasma optical emission spectroscopy on selected W-Re alloys after fabrication.

Material Name	W (wt%)	Re (wt%)	All other impurities (wt%)
Alloy 2	99.585	0.41	0.0053
Alloy 4	97.757	2.24	0.0032
Alloy 6	99.941	0.043	0.0157

Alloys 2, 4, and 6 were selected to be included in the RB*-19J irradiation experiments, as part of the PHENIX collaboration with Japan. This experiment will use a thermal neutron shield, so additional rhenium production is expected to be minimal. The irradiation will allow a comparison between the un-irradiated and irradiated alloys with little change in composition during irradiation. The three different temperature zones in the irradiation capsule will include W-Re alloy samples (Table 7).

Table 7. Sample size and quantity of the W-Re alloys that will be included in the 19J RB* irradiation.

Sample size	Alloy number	Quantity in 500°C zone	Quantity in 800°C zone	Quantity in 1200°C zone
D3 x t0.5	Alloy 6	1	1	1
D6 x t0.5	Alloy 2	3	3	3
D6 x t0.5	Alloy 4	1	1	1
D6 x t1	Alloy 6	1	1	1
D6 x t1	Alloy 2	2	2	2

FUTURE PLANS

Testing of the un-irradiated control samples will begin for eventual comparison with the irradiated samples. This analysis will include microstructural characterization, thermal conductivity measurements, and equibiaxial flexure testing.

6.3 IRRADIATION EFFECTS IN TUNGSTEN

L. M. Garrison (garrisonlm@ornl.gov), P. Edmondson, N.A.P. Kiran Kumar, T. Colling, M. McAlister, S. Curlin, M. Williams, L. Snead, T. S. Byun, D. Lewis, and M. Fukuda (Tohoku University, Japan)

OBJECTIVE

The objective of this work is to evaluate the effects of neutron irradiation on the mechanical properties and microstructure of tungsten-based materials to aid in developing plasma-facing components for fusion reactors.

SUMMARY

A total of 440 samples were irradiated in High Flux Isotope Reactor (HFIR) at temperatures from 70 to 900°C and fast neutron fluence of 0.01 to 20 $\times 10^{25}$ n/m^2 , E>0.1 MeV. Material types included in this study were [110] single crystal tungsten, [100] single crystal tungsten, wrought tungsten foils, annealed tungsten foils, and tungsten-copper laminates. Analysis of room temperature tensile test data for the single crystal samples reveals that ultimate strength decreases at less than 1 dpa. The tungsten-copper laminate tensile tests and fracture surface analysis were completed. Atom probe analysis of a single crystal tungsten sample irradiated to 2.9 dpa at approximately 750°C revealed rod-like, ribbon-like, and clusters-shaped Os and Re rich precipitates. Tungsten foils irradiated to 2.4 and 4.5 dpa showed increased amounts of the Re-Os rich precipitates but did not develop a void lattice.

PROGRESS AND STATUS

Single Crystal Tungsten Mechanical Properties:

Single crystal samples were more ductile both before and after irradiation in the [110] orientation along the tensile axis compared to the [100] orientation (Figure 45). For tungsten, the conversion 1$\times 10^{25}$ n/m^2 (E>0.1 MeV) ≈ 0.32 dpa is used.

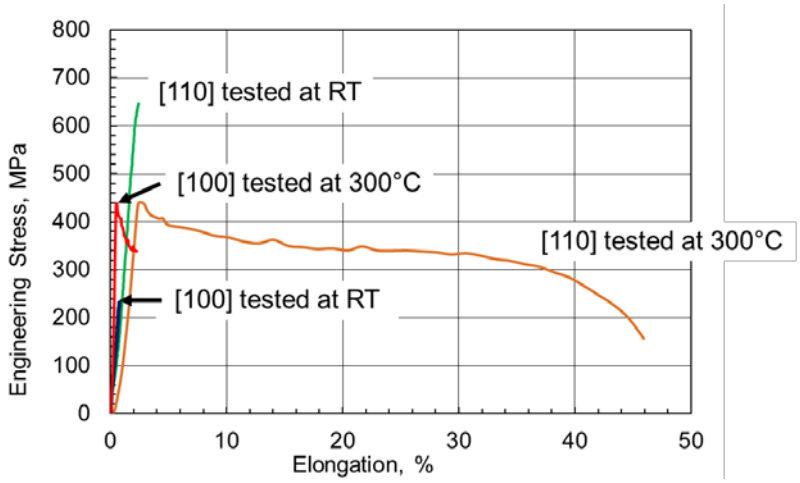

Figure 45. Single crystal tungsten tensile behavior for material irradiated to 0.03 dpa at 90°C.

Both orientations of single crystal tungsten exhibited the same trend of increasing hardness with increasing neutron dose; the [110] results are shown in Figure 46. The hardness values all follow the same trend despite the different irradiation temperatures.

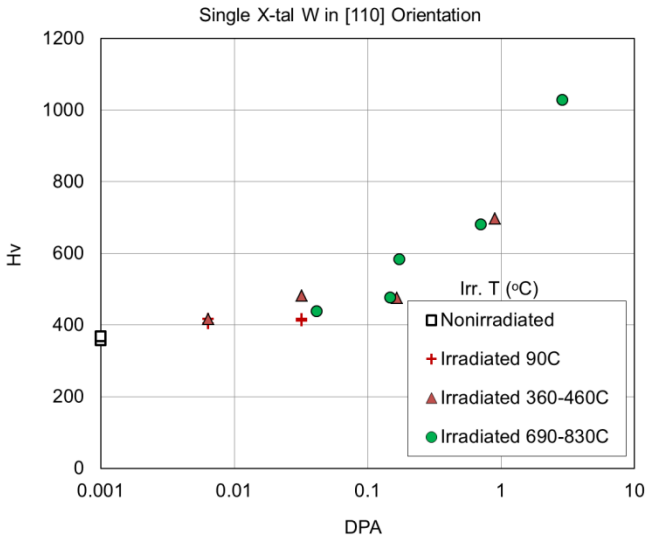

Figure 46. Hardness of single crystal tungsten after neutron irradiation.

Figure 47 shows the ultimate tensile strength, or fracture strength in the case of brittle fracture, of single crystal tungsten samples tensile tested at room temperature. While the hardness is seen to increase, the fracture strength decreased starting above ~0.1 dpa. Since these room temperature tests failed in a brittle manor, it is postulated that many of the samples failed on initial loading because they are sensitive to any surface defects, so the tensile do not properly reflect the strengthening apparent in the hardness tests.

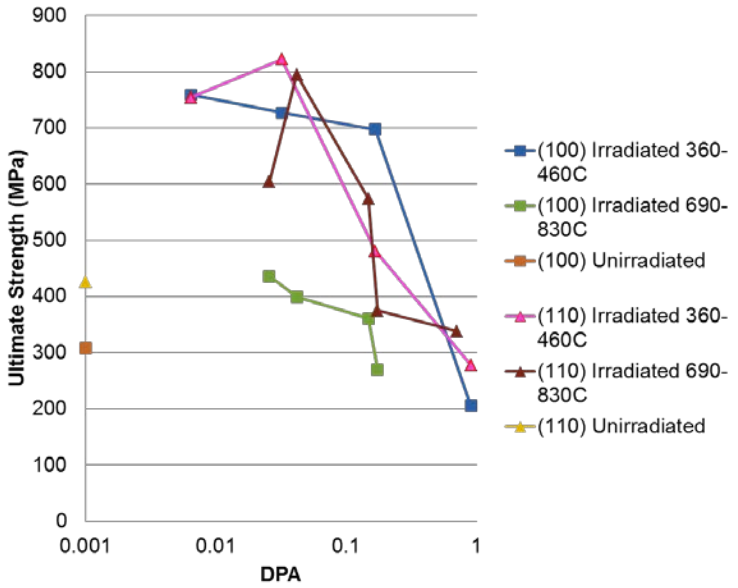

Figure 47. Room temperature ultimate tensile strength of irradiated single crystal tungsten.

Tungsten-Copper Laminates:

Tungsten-Copper laminate samples were irradiated up to 2.9 dpa (tungsten) at temperatures of 400-900°C. An example of tensile data is shown in Figure 48; the elastic regions of the curves have been adjusted using the tungsten Young's Modulus of 411 GPa. After irradiation to ~0.2 dpa and tested at 22°C the laminate is stronger than the un-irradiated sample tested at °C but the irradiated samples have lost essentially all the ductility shown by the control sample. After irradiation, when tested near the

irradiation temperature, the composite strength is similar to the un-irradiated composite tested at 650°C, but the ductility is reduced.

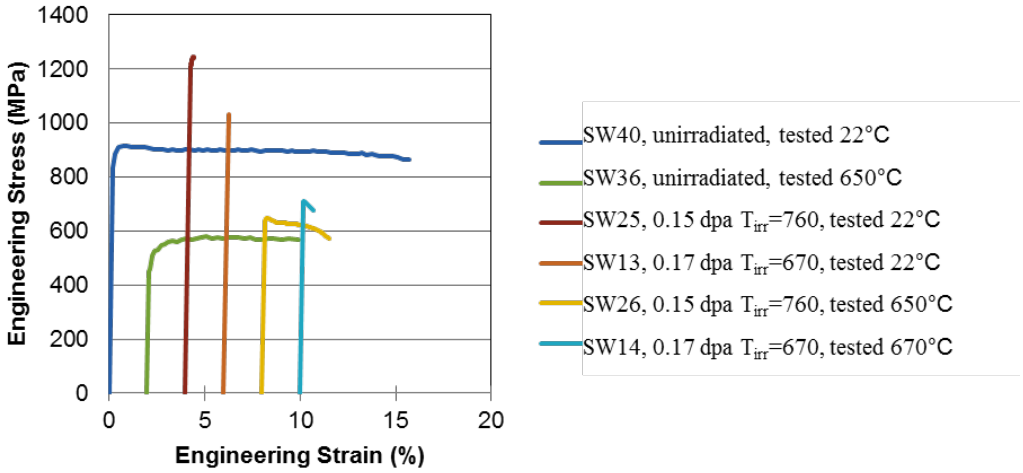

Figure 48. Tensile data for tungsten-copper laminate samples irradiated at ~0.2 dpa and 670-760°C compared with unirradiated sample data.

The different fracture behavior seen in SW25 and SW26 in the tensile curves in Figure 48 is illuminated in the images in Figure 49. For SW25 tested at room temperature, Figure 49a shows the multiple cracks present in the tungsten layer in addition to the fracture. The copper layer under the cracked tungsten appears to be holding the tungsten pieces together. In the SEM view of the fracture surface (Figure 49c), there is no noticeable reduction in area or necking of the tungsten layers, which each have rough, angular surfaces. Figure 50 shows the fracture surface of SW25 in more detail. The tungsten layers are rough locally but flat overall. The copper layer, in contrast, is smoother on the surface, but is clearly peaked in the center due to deformation during the tensile test. Despite the deformation of the copper layers, the overall composite fractured with little ductility. It is likely that as the tungsten layers fractured at over 1200 MPa, the copper layers were unable to sustain the load when it was suddenly transferred to them.

The side view of SW26 (Figure 49b), tested at 650°C shows deformation in the top tungsten layer rather than any cracks. The fracture surface of SW26 (Figure 49d) shows delamination within the tungsten layers and an overall reduction in area of the composite. At the test temperature of 650°C, the copper would not have had any significant strength as compared to the tungsten, so the ductile behavior was due to the tungsten deformation.

Microstructure Analysis—Atom Probe:

The Oak Ridge National Laboratory CNMS Cameca Instruments Local Electrode Atom Probe was used to identify and characterize the second phase precipitates formed during the irradiation of single crystal (011), nominally pure tungsten to doses up to 2.9 dpa at a temperature of approximately 750 °C.

For the 0.16 dpa irradiated specimen, the recorded time-of-flight spectra indicated that the tungsten had undergone some neutron-induced transmutation, with the primary transmutation products being Os and Re resulting in a bulk composition of W-0.4Os-0.7Re (at.%). The atomic reconstruction of the atom probe data shows the presence of fusiform-shaped Re- and Os-rich clusters (Figure 51a). The average composition of these clusters was found to be W-2.8Os-7.4Re (at.%), with a small spread in compositions, as shown in Figure 51b.

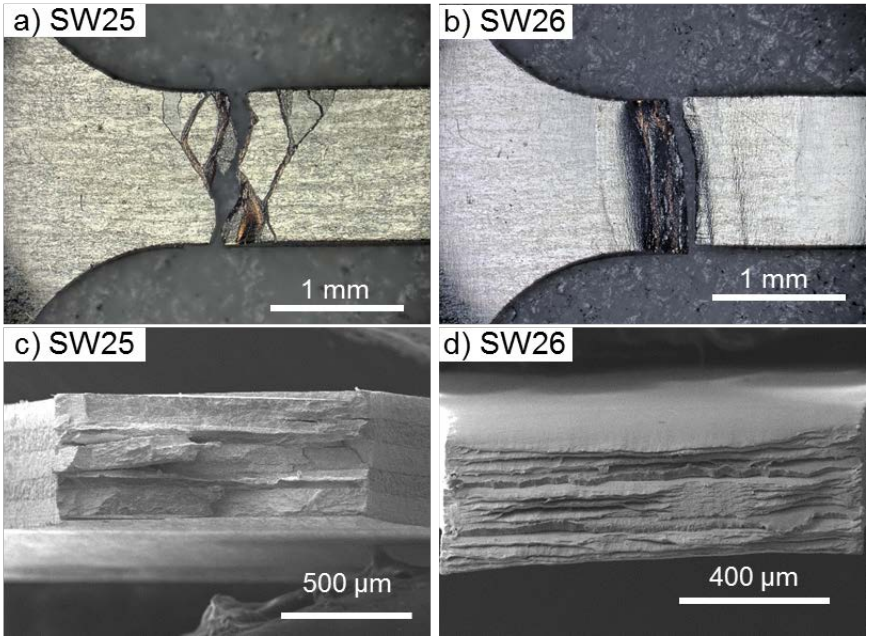

Figure 49. Optical microscope images a-b, and SEM images c-d of samples SW25 and SW25. Both samples were irradiated to 0.15 dpa at 760°C but SW25 was tensile tested at 22°C and SW26 was tested at 650°C.

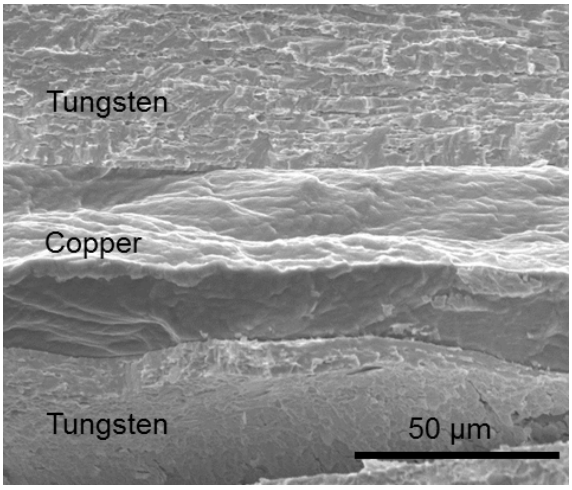

Figure 50. SEM image of fracture surface of sample SW25, irradiated to 0.15 dpa at 760°C, tensile tested at 22 °C.

The neutron-induced transmutation in the sample irradiated to 2.9 dpa resulted in a bulk composition of W-7.5Os-5.2Re (at.%). Again, precipitates rich in Os and Re are formed under irradiation, Figure 52a. These precipitates have morphologies that could be broadly classified as rod-like, ribbon-like, rod- and ribbon-like, and clusters. The compositions of these individual precipitates in addition to the bulk and average compositions (W-20.2Os-15.9Re) are shown in Figure 52b. All precipitates, with the exception of two, lie within the sigma phase composition boundary regardless of the morphology.

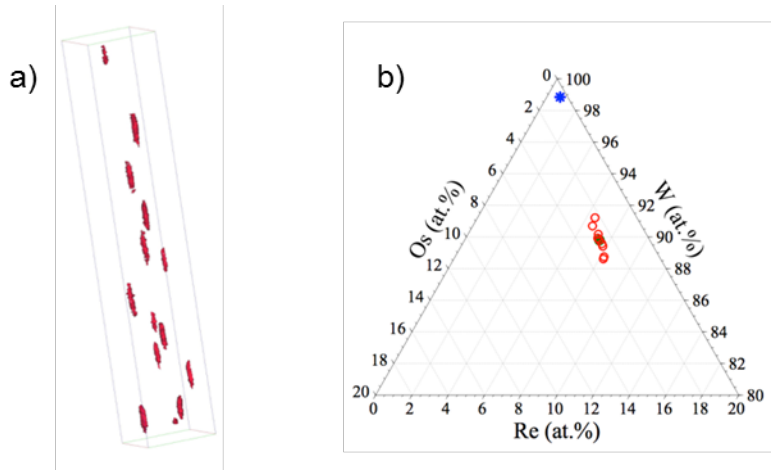

Figure 51. a) Concentration isosurface (ReOs - 20%) from the tungsten sample irradiated to 0.16 dpa. Reconstruction volume is 350 x 60 x 60 nm. b) Ternary diagram showing the composition of individual clusters in the 0.16 dpa irradiated sample. The blue asterisk is the average bulk composition.

There are two points of interest that should be noted regarding the shape and orientation of the precipitates: first, the shape (fusiform, and rod- and ribbon-like) of the neutron irradiated precipitates are vastly different to those formed during self-ion irradiation of a W-1Os-1Re (at.%) alloy in which spherical clusters were formed after irradiations to 33 dpa (A. Xu et al, Acta Mater. 87 (2015) 121). Second, the precipitates all appear to be crystallographically aligned. Electron backscatter diffraction was used to determine the crystal orientation along the z-axis of the atom maps (the long axis of the atom probe needle analyzed). This revealed that the direction of analysis was along the (111) crystal orientation, indicating that there may be some form of preferred diffusion of the solutes along this orientation.

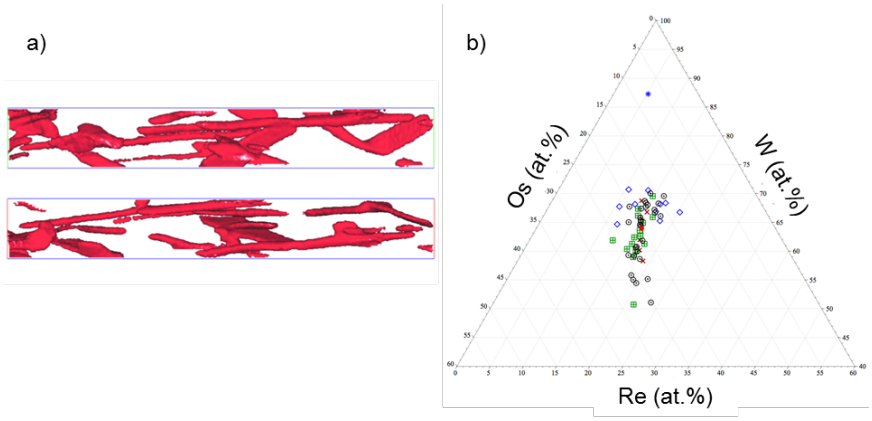

Figure 52. a) Concentration isosurface (ReOs - 20%) from the tungsten sample irradiated to 2.9 dpa. Reconstruction volume is 250 x 35 x 35 nm. b)Ternary diagram showing the composition of individual precipitates (ppt's) found in the irradiated tungsten sample. The blue asterisk is the average bulk composition; red circle is the average ppt composition; the black circles are ribbon-like ppt's; green squares are rod-like ppt's; dark red crosses are rod- and ribbon-like ppt's; and blue diamonds are cluster ppt's.

Microstructural Analysis—TEM:

In our earlier reports microstructure evaluation in tungsten at lower neutron doses was described. The dominate features were dislocation loops at lower temperatures and voids at higher temperatures. This

report present the microstructural changes in both polycrystalline and single crystal tungsten specimens exposed to higher neutron doses. The irradiation conditions of examined high dose tungsten specimens are presented in Table 8. A focused ion beam system with Ga^+ ion beam was used to prepare TEM specimens. In order to minimize the unwanted damage caused by Ga^+ ions, very low voltage and current (2 kV and 27 pA) were used on TEM specimens during final thinning process.

Table 8. High Temperature-High Dose Tungsten specimens examined by TEM

Sample ID	Material	Design Temp (°C)	Actual irradiation temperature (°C)	Fluence ($x10^{25}$ n/m^2)	Dpa
1W17	Single Crystal	500	705	2.2	0.7
1W19	Single Crystal	500	770	9.0	2.9
OW125	Polycrystalline	500	Not available	14.1	4.5
OW158	Polycrystalline	650	Not available	7.4	2.4

Figure 53 provides the summary of microstructural changes in single crystal and polycrystalline tungsten as a function of irradiation dose and temperature. In order to avoid confusion, henceforth only design temperatures instead of actual exposed temperatures will be shown on all the micrographs and tables. The TEM micrographs were recorded under two-beam condition with diffraction vectors g = 110 and $1\bar{1}0$. Line dislocation and loops were seen in 500°C, 0.7 dpa specimen. With increasing dose, considerably fewer loops were seen and the transmuted second phase dominates the microstructure. Both polycrystalline specimens exposed to higher irradiation doses showed heavy transmutation in the microstructures. A dense platelet type structure was observed in all high dose irradiated specimens (see Figure 53). In polycrystalline tungsten, apart from the platelet type structures within the grains, huge pancake type precipitates were also seen at the grain boundaries. The irradiation induced defect sinks such as dislocation loops, voids, which are formed in the early stage of irradiation may have acted as nucleation sites for the second phase precipitates. Therefore a drop in void number density was observed at higher irradiation doses (Table 9). The size of the precipitates also increased with the irradiation dose and temperature. However the number density of precipitates remained in the same range of about 10^{22} m^{-3}, did not change with the change in irradiation temperature and dose (Table 9).

Table 9. Summary of microstructural observation in pure tungsten after neutron irradiation

Material	Irradiation Temp (°C)	Fluence ($x10^{25}$ n/m^2)	Mean dislocation loop diameter (nm)	Mean void size (nm)	Void density (m^{-3})	Precipitate length (nm)	Precipitate Density (m^{-3})
Single Crystal	500	2.2	6.37	3.03	$1.22X10^{22}$	-	-
Single Crystal	500	9.0	-	5.28	$7.23X10^{20}$	20	$4.77X10^{22}$
Polycrystalline	500	14.1	-	7.40	$4.11X10^{21}$	33.5	$3.04X10^{22}$
Polycrystalline	650	7.4	-	6.40	$5.45X10^{21}$	36	$1.24X10^{22}$

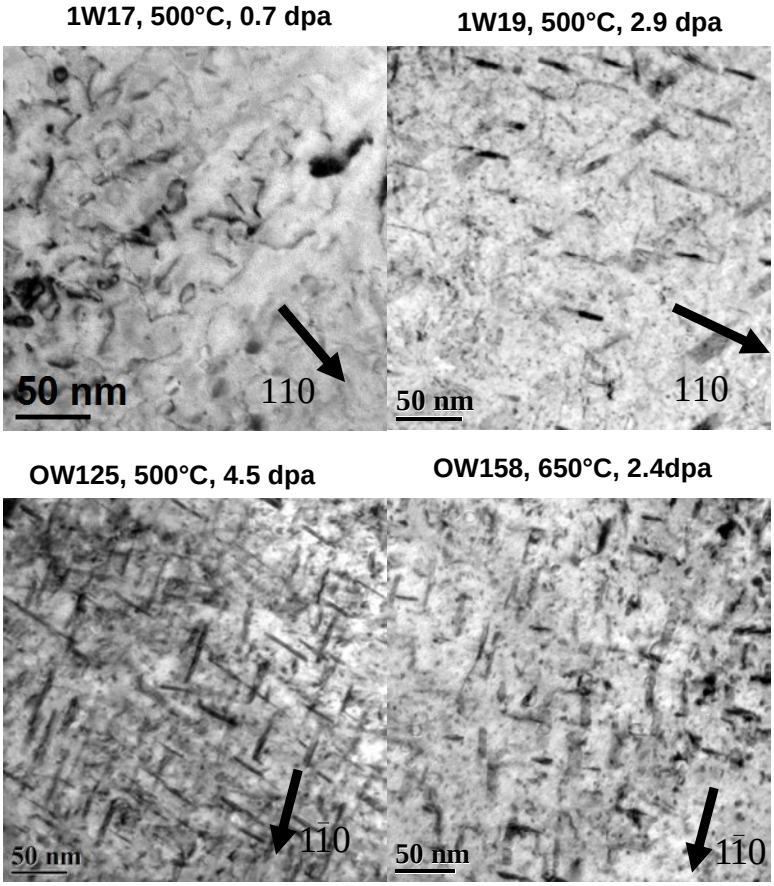

Figure 53. Micrographs illustrating the damage microstructure in tungsten. All images were recorded at B= [001]. 1W is single crystal, OW is polycrystalline material.

Transmutation:

It is widely known that tungsten produces transmutation rhenium and osmium during neutron irradiation. The compositional change in pure tungsten after exposure to a neutron dose of 1 dpa in HFIR is estimated at W-9.22%Re-5.02%OS (M. Fukuda et al, Journal of Nuclear Materials, 455, (2014), 460-463). In general, the solubility of Re and Os in pure tungsten is approximately 27 at.% and 5 at.% respectively at room temperature (B. Ralph, D. Brandon, Philosophical magazine, 8, (1963), 919-934 and A. Taylor, B. Kagle, N. Doyle, Journal of Less Common Metals, 3, (1961), 333-347). However due to irradiation, Re and Os form precipitates well below their solubility limits. Figure 54 shows the scanning transmission electron microscope (STEM) images of polycrystalline tungsten irradiated to 2.4 dpa at 650°C with platelet and pancake shaped precipitates within the grains and at the grain boundaries respectively. The STEM embedded with Electron Dispersive spectrometry (EDS) was used to measure the composition of the precipitates. The EDS confirms the presence of high concentrations of Re and Os in the platelets, but due to limited width of the platelet type structures the elemental ratio is still unclear. However, the pancake type structures at the grain boundaries showed an average composition of W- 40%Os-24%Re. Figure 55 shows the atomic profile of pancake type precipitates. Further study on these precipitates is ongoing.

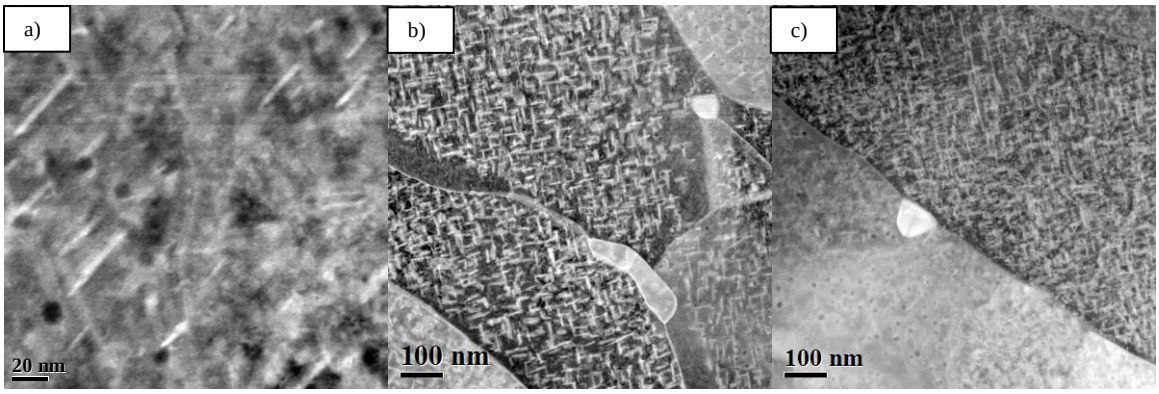

Figure 54. STEM micrographs showing the transmuted phase within grains and at the grain boundaries in OW158, 650°C- 2.4 dpa, polycrystalline tungsten a) platelet type precipitates within the grains, b) c) grain boundary precipitates.

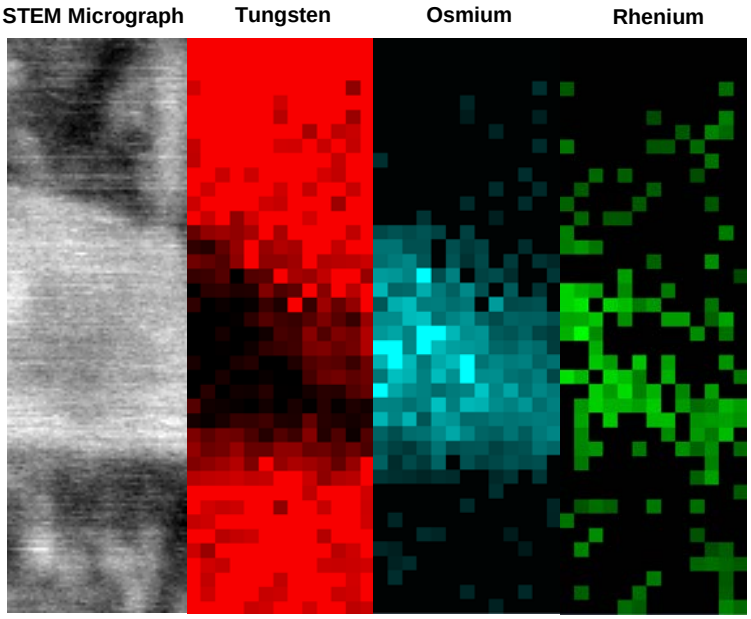

Figure 55. Atomic profile of the pancake type grain boundary precipitate shown in Figure 54.

Voids:

Microstructural examination of the irradiated specimens revealed the presence of voids at all four irradiation conditions (see Figure 56). The mean size of voids increased with the increasing irradiation dose and temperature (Table 9). Alignment of voids, usually referred as void lattice, formation in irradiated tungsten is usually observed at doses above 10 dpa (K. Krishan, Radiation Effects, 66, (1982), 121-155). Recently Tanno et al., have report void lattice formation even at smaller dpa in JOYO test reactors (T. Tanno et al, Materials Transactions, 48, (2007), 2399-2402). However, such void lattice formation was not observed in current irradiated specimens. Voids were rather randomly distributed in both polycrystalline and single crystal specimens. Void size distribution as a function of irradiation conditions is shown in Figure 57. With the increase in irradiation dose and temperature, the entire distribution moved to larger sizes.

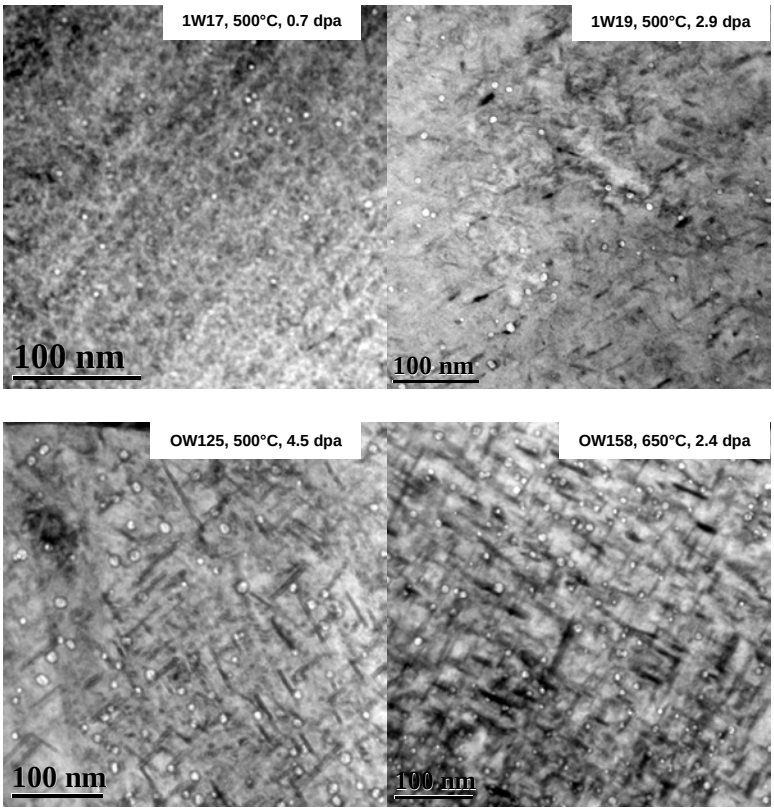

Figure 56. TEM images showing voids in neutron irradiated tungsten.

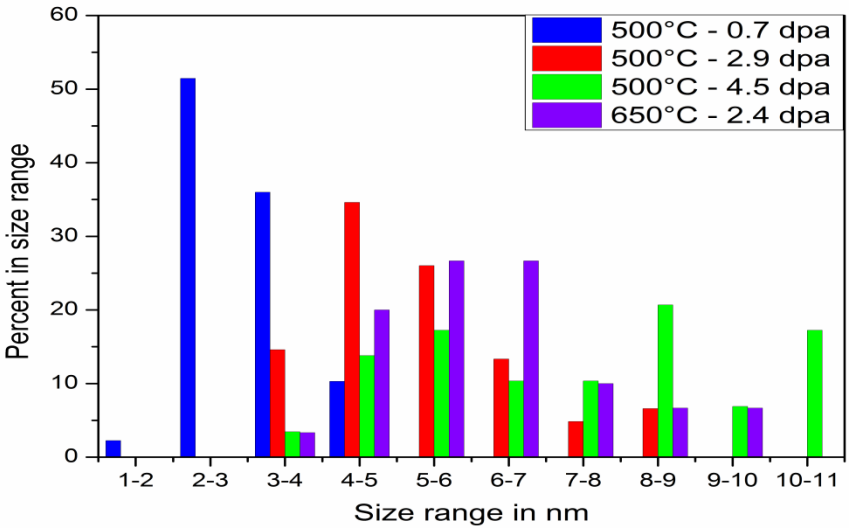

Figure 57. Void size distribution in irradiated tungsten.

FUTURE PLANS

More samples with doses higher than 2 dpa will be mechanically tested and microstructurally analyzed. Nano indentation is planned for the copper tungsten samples to gain information about individual layers within the composite.

6.4 GAS-POINT DEFECT INTERACTIONS IN TUNGSTEN

Xunxiang Hu (hux1@ornl.gov)

OBJECTIVE

The coexistence of gaseous foreign species (e.g., helium and hydrogen isotopes) and radiation damage is a major driver of a multitude of performance degradation mechanisms that limit the lifetime of plasma facing materials in fusion reactors. However, because very few facilities around the world have the capability to conduct gas behavior studies on neutron-irradiated samples, the overall picture of gas behavior in tungsten under irradiation remains disconnected, incomplete, and far from self-consistent. The objective of this project is to expand the current fundamental understanding of the behavior of those gas species in tungsten through a coordinated experimental and modeling study.

SUMMARY

In Fiscal Year (FY) 2015, the project was centered on the development of two unique experimental capabilities, i.e., positron annihilation spectroscopy (PAS) and thermal desorption spectrometry (TDS) coupled with an in situ 20 keV ion gun in the low-activation materials development and analysis (LAMDA) lab at ORNL. The PAS system is fully functional while the construction of the TDS system has been completed and the system is being calibrated and tested. The PAS system was successfully employed to investigate the defect evolution in single crystal tungsten following low dose and low temperature neutron irradiation. It reveals the correlation between microstructure and the mechanical properties, in combination with hardness tests and TEM observations.

PROGRESS AND STATUS

The PAS is a powerful tool to investigate the open volume in condensed materials. A new PAS system consisting of two techniques, positron annihilation lifetime spectroscopy and coincidence Doppler Broadening was established in LAMDA lab, serving as an important microstructural characterization tool. Figure 58 shows the PAS system in LAMDA. After becoming fully functional, this system has been used to study the defect evolution in neutron-irradiated tungsten, to quantify the pore population in a novel membrane, and to perform pre-irradiation characterization of T91 steel. The unique capability of PAS to identify small vacancy clusters, which are invisible in TEM observations, enables its broad application in nuclear materials research.

The integrated characterization of the microstructure of neutron irradiated tungsten using various techniques serves as the cornerstone for understanding the gas-point defect interactions in tungsten. Defect evolution and the resulting mechanical property changes of tungsten following low temperature and low dose neutron irradiation was investigated. Isochronal annealing at 400, 500, 650, 800, 1000, 1150, and 1300°C was performed on two tungsten specimens neutron irradiated at 90°C to nominally 0.006 and 0.03 dpa, specimens 1W05 and 1W25, respectively. Following one-hour annealing, ex situ characterization of vacancy defects using PAS was carried out. Figure 59 shows the size distribution of the 3-D vacancy clusters in tungsten following different annealing conditions by interpreting the measured positron lifetime spectra in a combination with the well-developed positron trapping model.

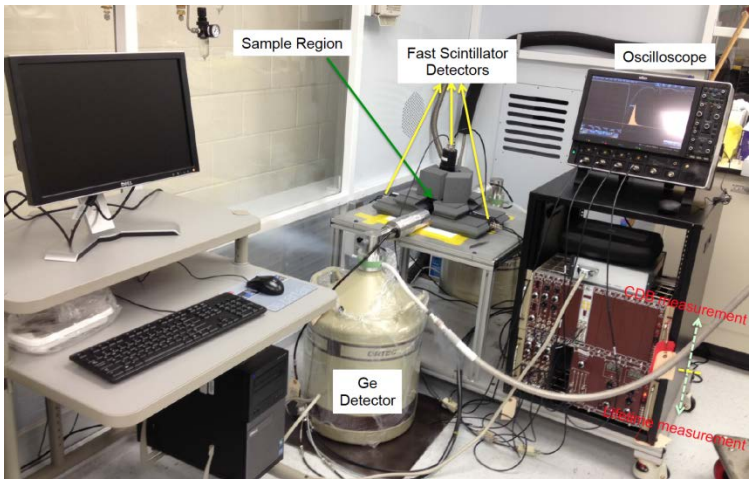

Figure 58. Positron Annihilation Spectroscopy (PAS) system in LAMDA.

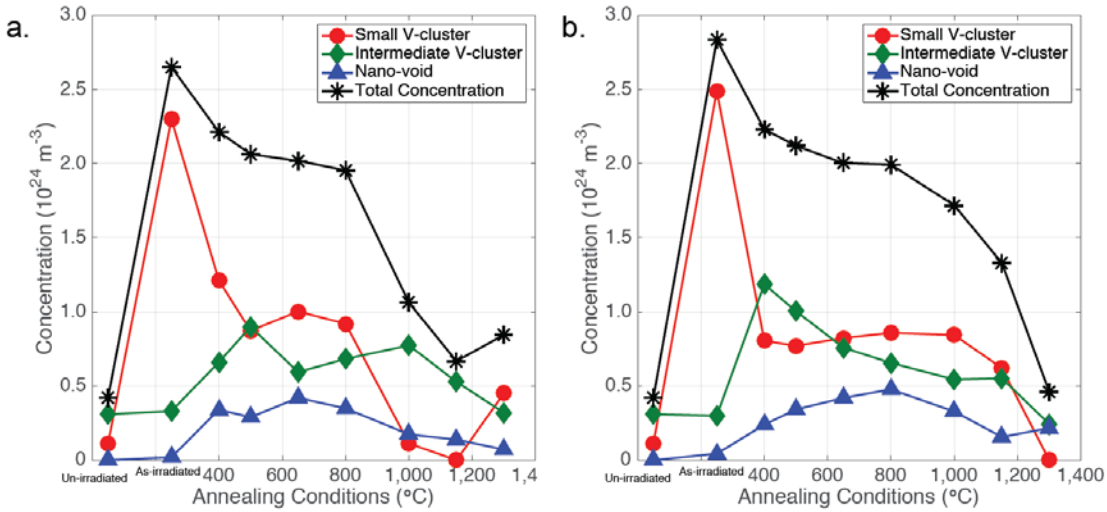

Figure 59. Size distribution of the three-dimensional vacancy clusters in (a) 1W05 (90°C, 0.006 dpa) and (b) 1W25 (90°C, 0.03 dpa) for different annealing conditions, derived from positron lifetime analysis.

The TEM observations at selected annealing conditions for 1W25 provided supplemental information on dislocation loop and visible void populations, shown in Figure 60. Thus, a relatively complete picture of the microstructural evolution of neutron irradiated tungsten during the isochronal annealing processes was obtained, based on which the physical explanations of annealing Stages III, IV, and V were extracted. Stage III (400°C) resulted from the migration of monovacancies. The dissolution of intermediate vacancy clusters, the existence of vacancy-impurity complex and the annihilation of dislocation loops contributed to Stage IV (500-800°C). Significant dissociation of vacancy clusters and voids coarsening were the major cause of Stage V (1000-1300°C).

During the annealing process, microstructures evolved, and corresponding mechanical property changes occurred. Hardness as a factor contributing to irradiation embrittlement was determined by micro-Vickers testing following each annealing condition, as shown in Figure 61. Annealing hardening due to the growth of big vacancy clusters and hardness reduction in the high temperature regime (> 800°C) resulting from significant damage recovery was observed. The direct comparison helps to reveal the relationship between the microstructure and mechanical properties of tungsten.

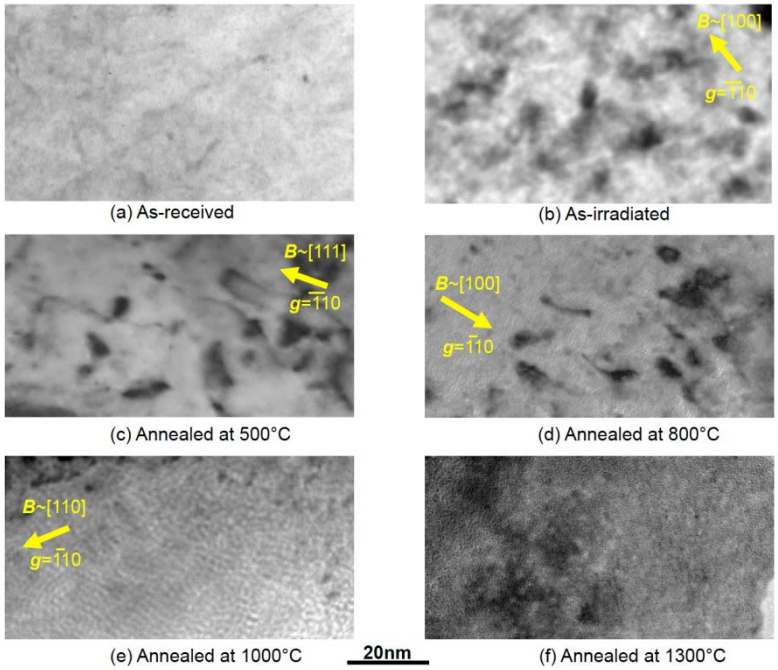

Figure 60. Bright-field images of damage microstructures in (a) as-received un-irradiated single crystalline W(110) and (b) as-irradiated tungsten, and post-irradiation annealed tungsten subject to (c) 500°C for 1 h, (d) 800°C for 1 h, (e) 1000°C for 1 h, and (f) 1300°C for 1 h. The images were taken under two-beam conditions. The arrow in each image shows the direction of the g-vector.

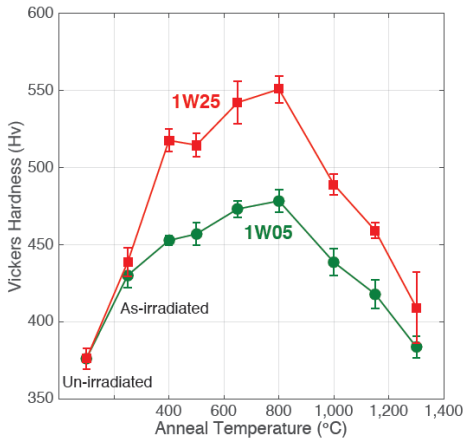

Figure 61. Vickers hardness for 1W05 (90°C, 0.006 dpa) and 1W25 (90°C, 0.03 dpa) following different annealing conditions. The hardness values of un-irradiated and as-irradiated samples are also shown for comparison.

Following the microstructure characterization of un-irradiated and neutron-irradiated tungsten, helium/deteurium implantation and subsequent thermal desorption will be performed in combination with multiscale modeling to evaluate the synergestic effects of neutron irradiation on helium and hydrogen isotope behavior in tungsten. The TDS is the critical experimental technique to realize the proposed work. A new TDS system coupled with an insitu 20 keV ion gun has been successfully designed and assembled, shown in Figure 62. This system consists of an implantaion chamber, heating chamber, and measurement chamber. It is being tested and calibrated and is expexted to be fully functional in FY2016.

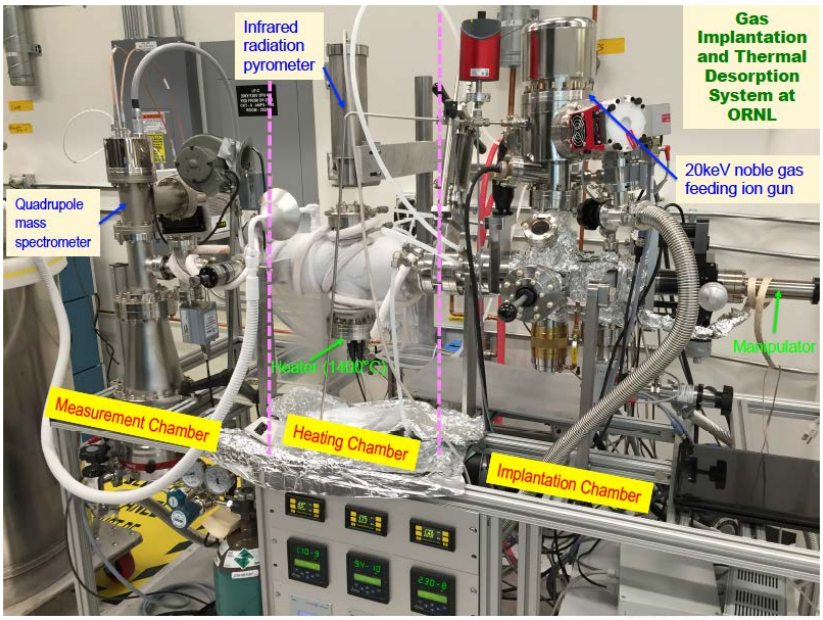

Figure 62. Thermal desorption spectromety system being tested in LAMDA.

FUTURE PLANS

In FY2016, microstructure characterization of tungsten exposed to various neutron irradiation conditions will be performed employing a variety of characterization techniques. Of particular interest are the gas-defect interactions in tungsten, which will be explored on the TDS system now being tested. Test and calibration of the TDS system will be the priority in the beginning of FY2016. Then gas implantation (i.e., He, D) will be performed on the un-irradiated and neutron-irradiated tungsten samples, followed by TDS measurements. Meanwhile, the microstructure of the samples after gas implantation will also be studied by using PAS and TEM to evaluate the microstructure changes induced by the introduction of gaseous species. A cluster dynamics model will be developed to capture the fundamental mechanisms describing the gas-defect interaction, enabling direct comparison with the measured gas desorption spectra.

6.5 DAMAGE-MECHANISM INTERACTIONS AT THE PLASMA-MATERIALS INTERFACE – AN EARLY CAREER AWARD PROJECT

C. M. Parish (parishcm@ornl.gov)

OBJECTIVE

The overarching objective of this work is to bridge the gap between the atomistic knowledge and models and the phenomenological materials science underlying the design, fabrication, and service of divertor and other plasma-facing materials for magnetic confinement fusion. Specifically, the influence of intrinsic defects (dislocations, grain boundaries) and extrinsic defects (ion- and neutron-irradiation damage, impurities) interactions with He and bubbles, in terms of nucleation sites, growth, trapping, and surface degradation, will be measured.

SUMMARY

This project began in mid-July 2015. Presently, stock material has been obtained and is being characterized. Initial collaboration visits have been made to University of Tennessee-Knoxville (UT-K), University of California, San Diego, and General Atomics DIII-D. Initial microstructural characterization has been performed on collaborators' plasma-exposed samples, and first new exposures are being planned.

PROGRESS AND STATUS

Stock material (nominally 99.995% pure tungsten, metals-basis) has been obtained from ESPI Metals (Ashland, OR, USA). The stock was a 25×30×0.3 cm plate, and shows a strong rolling texture and fine grain size, indicative of hot rolling. The texture is shown in Figure 63, and the grain structure in Figure 64. Grain size is ~3-4 μm, with an elongated aspect ratio averaging ~0.4, and many low-angle grain boundaries. This starting structure is beneficial for the intended experiments, in that a wide array of different grain orientations and boundaries are available. A chemical assay of the stock purity is planned.

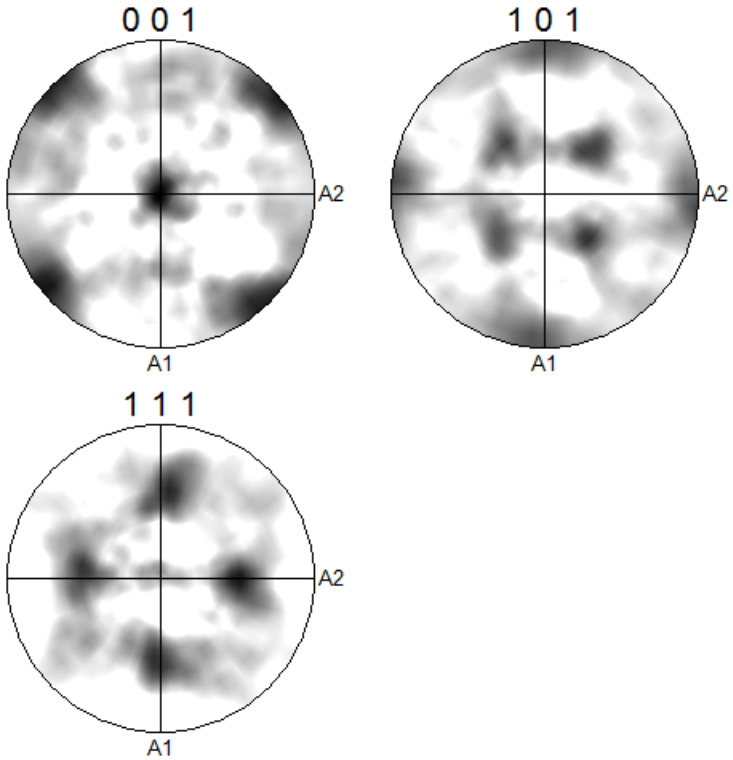

Figure 63. Pole figures for the stock material. Out-of-the-page is the plate normal, and ↑ is the rolling direction. White: 0 intensity, black: 7.75× random.

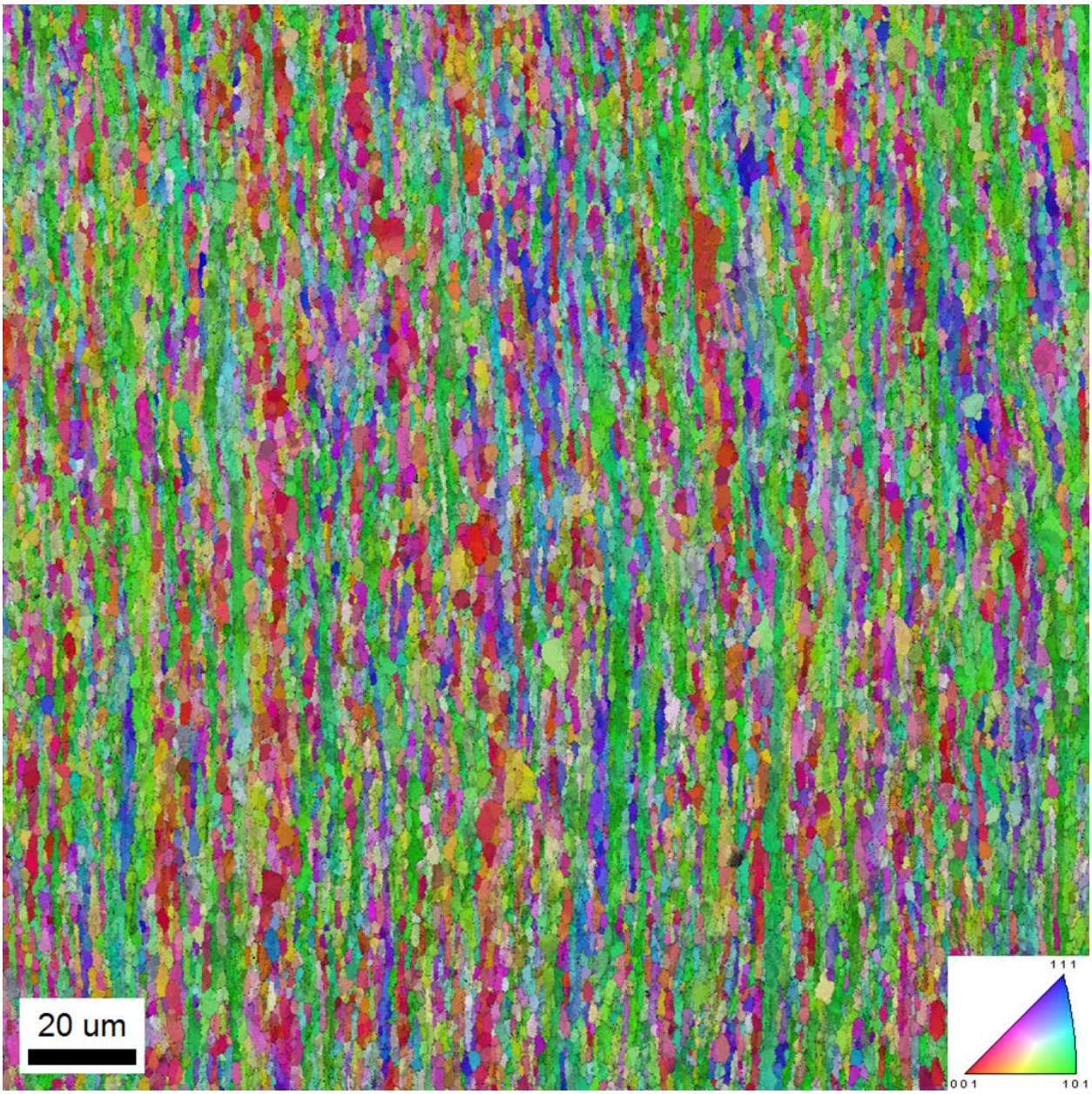

Figure 64. Cross-Section of the stock material. The ← direction is the plate normal, and ↑ the rolling direction. Data presented is the IPF in color (inset unit triangle) projected onto the direction out of the page; color intensity is the EBSD pattern fit value at each pixel.

Initial data has been obtained on ITER grade ALMT material plasma-exposed at 1000°C (sample examined in collaboration with Dr. David Donovan, UT-K). Significant surface faceting and topography was observed in the material, which had been polished smooth prior to plasma exposure. Consistent with previous results from ion beam exposure at the Oak Ridge National Laboratory (ORNL) multi-charged ion research facility (MIRF), this plasma-exposed tungsten showed smooth grains near the [103] region, pyramids near [001], and terraces along [114]-[112], Figure 65. The exposure was ~75 eV He, ~2×10^{19} ions/m^2sec, ~3×10^{24} ions/m^2. The previous results from ORNL MIRF were for 80 eV He, 4×10^{24} ions/m^2, ~10^{20} ions/m^2sec, ~1130°C.

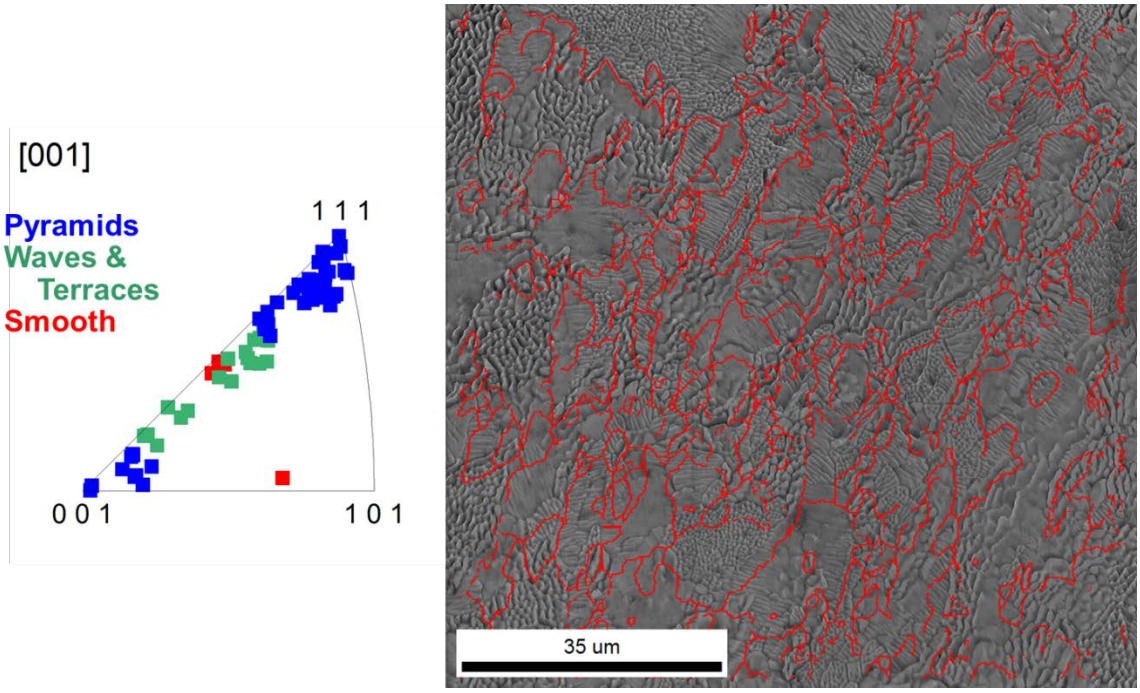

Figure 65: SEM image, right, with superimposed EBSD-determined grain boundaries. The inverse pole figure shows the surface normal orientations of different plasma-induced morphologies.

FUTURE PLANS

Approximately two months of this five-year project have been completed. In the immediate future, samples for scanning electron microscopy, plasma exposure, and TEM will be prepared. A chemical purity assay is planned for the stock material. It is also intended to begin sample ion irradiations to work in parallel with the low-energy plasma exposures.

6.6 UPGRADE OF THE ORNL PLASMA ARC LAMP FACILITY

A.S. Sabau (sabaua@ornl.gov), C.R. Schaich, J. Kiggans, and Y. Katoh

OBJECTIVE

The objective of this work is to upgrade the Plasma Arc Lamps (PALs) at Oak Ridge National Laboratory (ORNL) to enable the high-heat flux testing of a wide range of: (a) irradiated materials specimens for plasma facing components and (b) mock-up divertor components.

SUMMARY

The efforts were focused on:

- Enhancing safety during testing of irradiated specimens by reducing the footprint of the contaminated area and the level of contamination in the test section, and
- Increasing the incident heat flux from PAL.

In order to enable higher heat fluxes using PAL, appropriate funding must be available to the project; the available funding levels did not allow the upgrade of PAL facilities in Fiscal Year 2015. Other Department of Energy programs that use the PALs were contacted in order to leverage the resources and approximately 25% of the new reflector costs were obtained from those programs. However, even with these additional resources from other programs, the current commitments from the fusion program at the current funding levels will allow the fabrication of the new reflector in March 2017.

PROGRESS AND STATUS

The enhancement in the radiation safety during testing of irradiated specimens was accomplished by employing an additional, smaller sealed chamber with a hemispherical cap, rated for vacuum systems, enclosing the cooling rod, specimen holder, and irradiated specimen (Figure 66). The following activities were conducted:

- A high-vacuum system for the additional sealed chamber enclosing the specimen holder and irradiated specimen, including its own high-vacuum pumping system, was assembled and tested.
- Both the high-vacuum and low-vacuum systems were instrumented with appropriate vacuum pressure transducers.

The reduction in oxidation during testing of irradiated specimens was accomplished by employing an additional high-vacuum test section embedded within the main (low-vacuum) test chamber. The high-vacuum test section encloses the cooling rod, holder, and irradiated specimen (Figure 66a). The main test chamber will not be contaminated, lowering the maintenance and operational costs. Also, the limited amount of O_2 in the high-vacuum test section will limit formation of tungsten oxide. Specifically, the high-vacuum section is formed by a quartz dome, whose circumference is shielded by a Cu plate in order to protect the O-ring seal from direct heating by the plasma-arc lamp (Figure 66b).

The data for the high-vacuum pressure is next shown for selected cycles for specimens 1, 2 and 5. In order to keep the high-vacuum to acceptable levels, the heat flux was increased incrementally to its maximum value. Data acquired with a high-vacuum pressure transducer indicated that the absolute pressure increased during the High Heat Flux Testing (HHFT) (Figure 67a-b). The pressure and temperature data is shown for specimen 2 and 5 in Figure 68. The maximum pressure was approximately

10^{-6} to 10^{-4} Torr, lower than that for specimen 1. This higher vacuum was maintain for all the subsequent specimens, indicating that the entire testing section was preconditioned during the HHFT of specimen 1 by slowly outgassing most of the volatile species in the test section.

Increase the Incident Heat Flux from Plasma-arc Lamps:

Original equipment Manufacturer (OEM) support: Mattson, Inc., the OEM of the PAL was contacted and the electrode fabrication and support for ORNL systems has resumed. The 750 kW PAL, rated at 4 MW/m^2, is fully operational. Three new anodes were purchased for the 300 kW PAL.

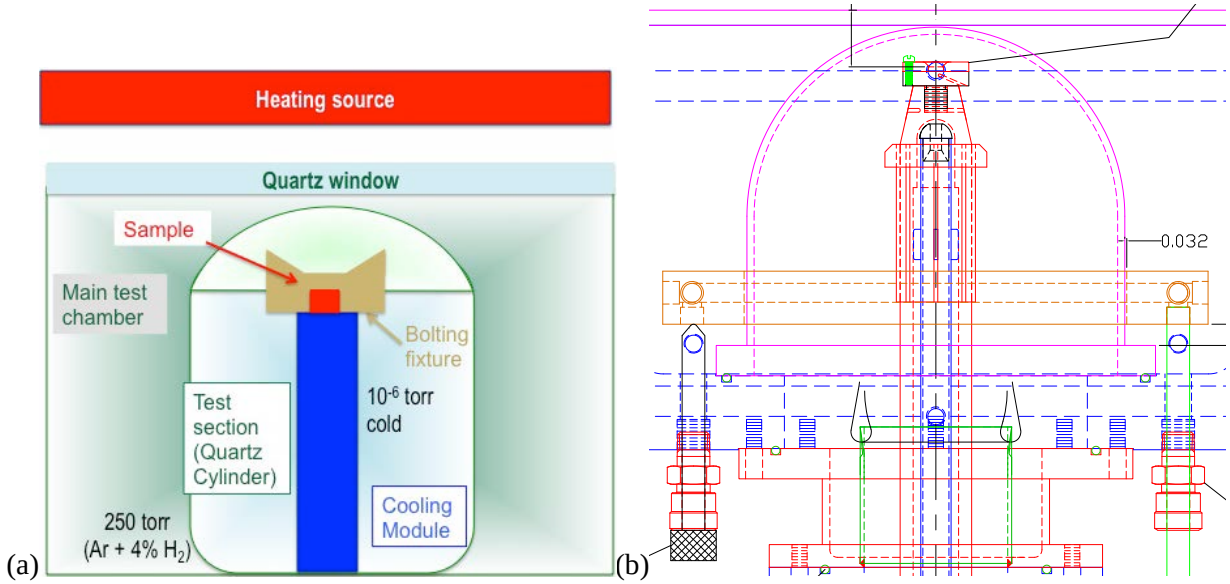

Figure 66. Schematic illustration of the use of two confinement enclosures in the test section.

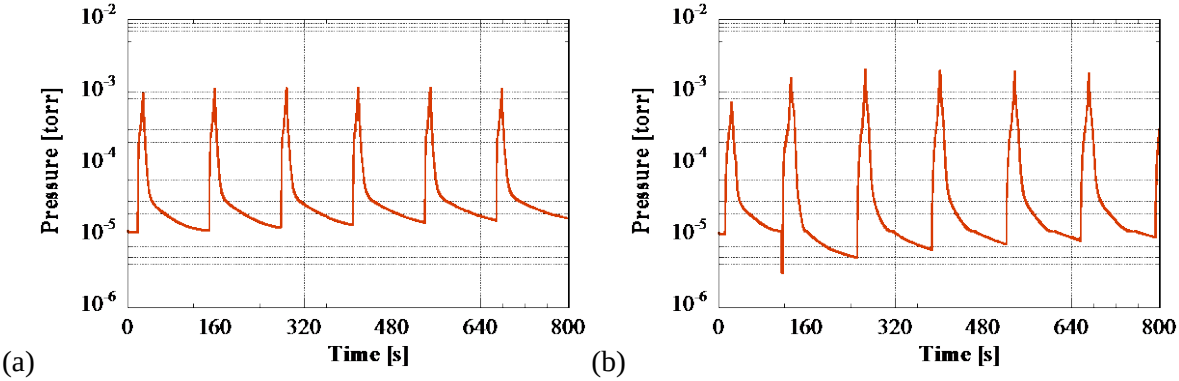

Figure 67. Representative data on absolute pressure for specimen 1 and cycles: (a) 84-89 (300 W/cm^2 for 10 s) and (b) 132-137 (300 W/cm^2 for 12 s cycle 132 and 15 s for cycles 133-137).

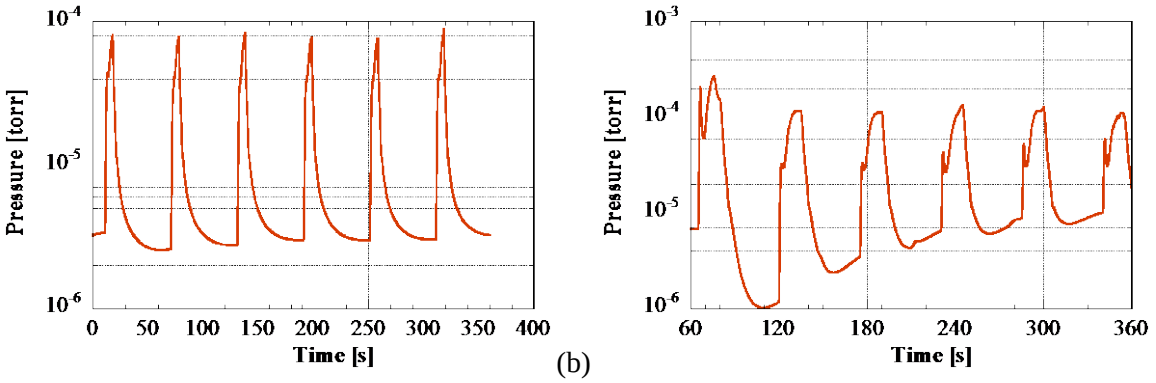

Figure 68. Representative data on absolute pressure for (a) specimen 2 for cycles 114-119 and (each cycle: 278 W/cm^2 for 7 s) and (b) specimen 5 for cycles 37-42 (each cycle: 323 W/cm^2 for 15 s).

New reflector for the 750 kW PAL to increase its heat flux to 16 MW/m^2. Currently, the 750 kW PAL system uses a uniform reflector rated at 4 MW/m^2 over a wide area of 12x14 cm^2. To increase the heat flux, a new line-focus reflector for the 750 kW PAL is proposed. The line-focus reflector will distribute the 750 kW energy such that a higher maximum heat flux, as high as 16 MW/m^2, will be attained over a smaller region of 2x14 cm^2. A quotation was obtained from the Mattson Inc. but the funding is not yet available at ORNL for its commission.

Status of 300 kW PAL, rated at 27 MW/m^2. A preliminary diagnosis of the 300 kW PAL was conducted and the 300 kW PAL was successfully brought online in February 2015. However, the 300 kW PAL malfunctions, requiring one anode per 90 s of operation at high heat fluxes. The debugging of the 300 kW PAL has stopped due to the lack of funding.

The current statuses of the PAL facilities at ORNL, together with the upgrade and maintenance needs, are shown in Table 10 and Table 11.

Table 10. High-heat flux testing using the water-wall PAL systems available at ORNL

System	Power [kW]	Profile of heat flux on sample	Pulse Duration [s]	Incident Max. Heat Flux [MW/m^2]	Total Heat Flux Area [cm^2]	Size @ Max Heat flux [cm^2 @ MW/m^2]	Status
Vortek 500	750	Uniform	0.02-30*	4.2	320	9x12 @4 12x14 @1	Operational
Vortek 300	300	Bell shape	0.01-30*	27	41	1x10	Malfunctions, Need debug
Vortek 300 (One Pulse)	300	Bell shape	0.001-0.005	200	41	1x10	Malfunctions, Need debug
Vortek 500	750	Bell shape (new refl.)	0.02-30*	16	200	2x15	New reflector

* Can be easily extended to 450 s by providing additional coolant

Table 11. High-heat flux testing using the water-wall PAL systems available at ORNL

System	Current Incident Max. Heat Flux [MW/m^2]	Size @ Max Heat flux [cm^2 @ MW/m^2]	Effort needed to reach desired heat flux
Vortek 500 (current uniform reflector)	4.2	9x12	Uniform reflector cannot attain desired heat flux
Vortek 300	27	1x10	Debug of entire system, and software upgrade needed
Vortek 300 (One Pulse)	200	1x10	
Vortek 500 (new reflector)	16	2x15	New reflector needed

FUTURE PLANS

The increase in the HHFT will be accomplished through either of the following steps:

- Further debug the 300 kW PAL, rated at 27 MW/m^2 with its own line-focus reflector, when additional funds are available for system debug.
- Purchase a new line-focus reflector for the 750 kW PAL that would deliver 16 MW/m^2, pending the availability of new funding.

6.7 HIGH-HEAT FLUX TESTING OF FUSION MATERIALS

A.S. Sabau (sabaua@ornl.gov), J. Kiggans, S. Gorti, and Y. Katoh and K. Tokunaga (Kyushu University)

OBJECTIVE

The objective of this work is the High Heat Flux Testing (HHFT) of irradiated materials for plasma facing components and of mock-up divertor components using Plasma Arc Lamps (PALs). This will provide basic materials property information and constitutive equations for materials behavior in the harsh fusion environment.

SUMMARY

In Fiscal Year 2015 HHFT of five bonded W-F82H specimens, was successfully conducted at Oak Ridge National Laboratory as part of the joint US/Japan PHENIX program. Other efforts focused on:

- Achieving a high-thermal gradient through the specimen while enhancing the measurement accuracy of the specimen temperature, and
- Developing a model for the thermo-mechanical simulation of the HHFT.

PROGRESS AND STATUS

In order to attain a high thermal gradient through the W/F82H specimens, new bolting holders were fabricated from a Ta-10W alloy that exhibits high strength at high temperature. In the final design, as shown in Figure 69, the specimen was mounted directly onto a Cu cooling rod to attain the lowest temperature on the back surface of the specimen and thus enabling a highest thermal gradient in the specimen. The thermocouple wires were shielded using an Nb cone. The reduction in the oxidation during testing of irradiated specimens was accomplished by employing a high-vacuum test section made by a quartz dome that would enclose the cooling rod, holder, and irradiated specimens (Figure 69).

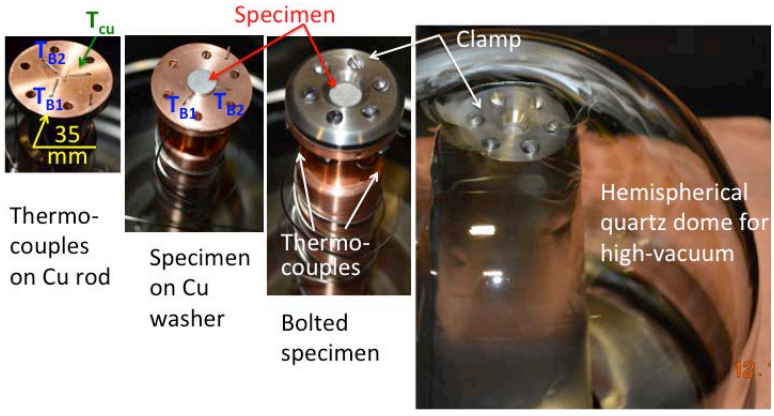

Figure 69. Experimental setup showing the sequence for placing different components. From left to right the individual frames indicate: placement of thermocouples on Cu rod, Cu washer and specimen on the rod, clamping the specimen, thermocouple shield and high-vacuum dome, respectively.

Several high-heat flux experiments were conducted as part of the joint US/Japan PHENIX program, in December 2014 (Table 12). Thickness of the W and F82H steel segments of the bonded specimen was 1 mm each. Each specimen was exposed to high-heat fluxes adjusted such that the maximum temperature would attain the target temperature shown in Table 12. The specimen temperature, T_{Cu}, was measured with thermocouples inserted between the back surface of the specimen and top surface of the Cu rod.

Table 12. W/F82H specimens[1] exposed to high-heat flux testing.

	Diameter [mm]	[2]T_{Max} [^oC]	[3]No. Cycles	Cycle duration [s]	Max. Heat Flux [W/cm^2]	Comments
1	10	750	101	10-15	300	Delamination observed
2	10	500	164	7-10	210-278	No delamination observed (Visual)
3	10	550	214	4-5	300	No delamination observed (Visual)
4	6	450	110	10-16	300	No delamination observed (Visual)
5	6	550	42	10-15	300-323	[4]No delamination observed (Visual)

[1] Thickness of W and F82H steel each 1 mm.

[2] The target temperature for the interface between the W and F82H.

[3] Number of cycles at heat flux.

[4] Thermocouples shielded from the direct IR flux.

Typical pressure and temperature data is shown for Specimen 5 in Figure 70. The peak of the measured temperature T_{Cu} was approximately 240^{o}C. The temperatures at the top surface of the specimen are expected to be higher than measured temperature T_{Cu}.

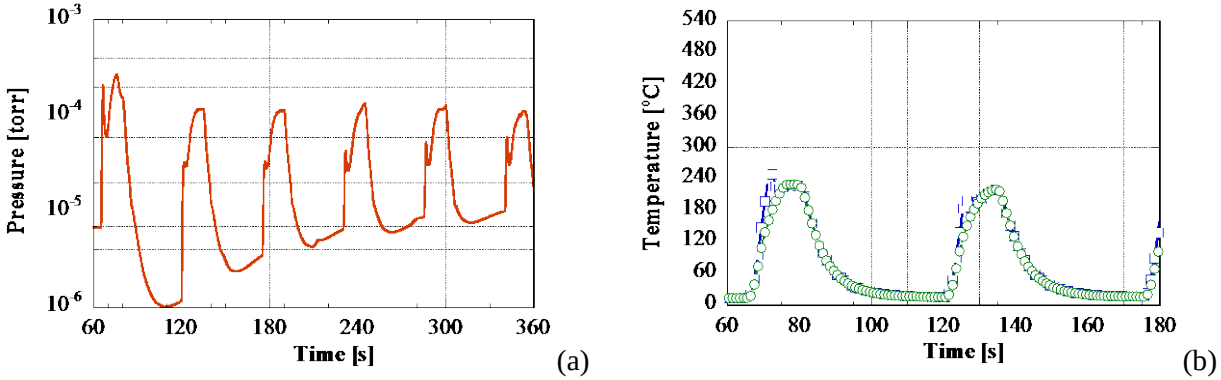

Figure 70. Representative data for specimen 5: (a) absolute pressure for cycles 37-42 and (b) measured temperature T_{Cu} for cycles 37 and 38 with shielded thermocouples (each cycle: 323 W/cm^2 for 15 s).

The accurate temperature measured on the back surface of the Cu washer by T_{Cu} was taken as a temperature boundary condition in the model. This assumption enabled the calculation of the heat flux removed from the back surface of the Cu washer by the cooling water within the Cu rod. The simplified heat transfer model eliminated the need for complex Computational Fluid Dynamics (CFD) simulation of the water flow and avoided the coupling of CFD and stress analysis. In this model, the thermal contact conduction (TCC) between the F82H and Cu washer is an unknown as the top surface temperature could not be measured.

In order to understand the deformation and residual stresses in the samples tested under high-heat flux, a coupled thermal and mechanical analysis is sought. Temperature dependent mechanical properties for the materials involved were obtained in preparation for numerical simulations. Inelastic properties, including hardening properties, were obtained from open literature for F82H steel and Cu materials. Thermomechanical models for the simulations of the entire HHFT were implemented in the ABAQUS™ software and numerical simulation results were conducted for sample S5 by taken into account the actual high-heat flux and high-temperature cycles. One of the main modeling assumptions is that the clamp is a rigid body, i.e., the distance between the clamp surface and the back-side of the Cu washer was held constant. For the last HHFT cycle, the calculated temperatures at the top surface of W, top and back surfaces of F82H, and top of Cu washer are shown in Figure 70a-b. The results presented were for TCC per unit area (between the F82H and Cu washer) of 5,000 and 7,000 [W/m^{2}K].

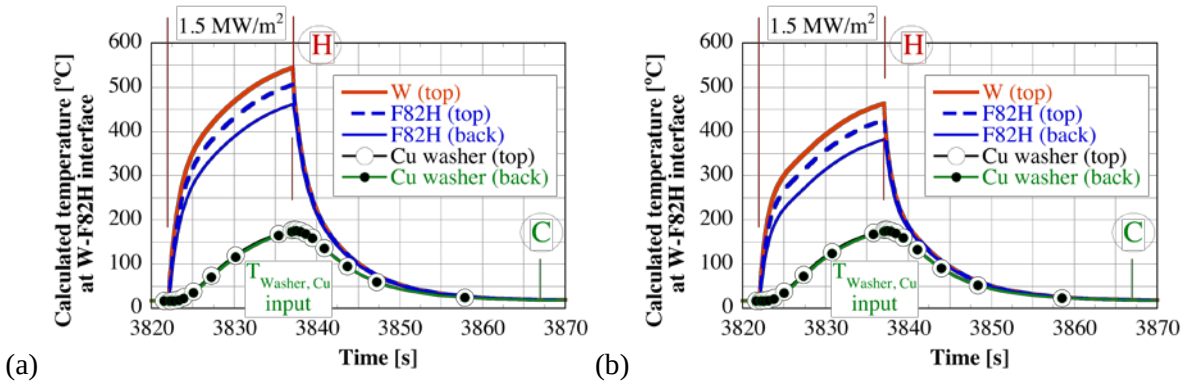

Figure 71. Calculated temperature evolution during cycle 42 for thermal contact conduction per unit area between the F82H and Cu washer of (a) 5,000 and (b) 7,000 [W/m^{2}K]. The temperature on the back-surface of the Cu washer was used as input.

Based on the temperature and mechanical properties, the following variables were calculated: specimen deformation, plastic deformation, and build-up of residual stresses during HHFT. The results for the Von Mises stress [Pa] is shown at two instances for cycle 42, as indicated by letters H and C in Figure 71. In these instances, the specimen is at high temperature (Hot), i.e., right at the end of the HHF, and at room temperature (Cold), respectively. The stresses are shown on a deformed mesh in order to illustrate the changes in the specimen geometry during HHFT, with the deformation scale indicated in figures. Figure 72 and Figure 73 contain the data for the case when TCC is 5,000 and 7,000 [W/m^{2}K], respectively. Although the specimen S5 thickness was 6 mm, simulation data was also obtained for 10 mm specimens. The following observations can be made with respect to the stress and deformation results:

- At high temperatures, the specimens bulge *downward* at its center, resting on the clamp at its outer edges.
- At room temperature, before clamp removal, the specimens bulged *upward* in its center.
- Predicted residual stresses after cooling are higher for the 6 mm than those for the 10 mm specimens.
- The maximum stress was found to occur in the steel, at the steel-W interface. The maximum stress was located at the edge of the steel and within the steel for the 6 mm and 10 mm specimens, respectively.

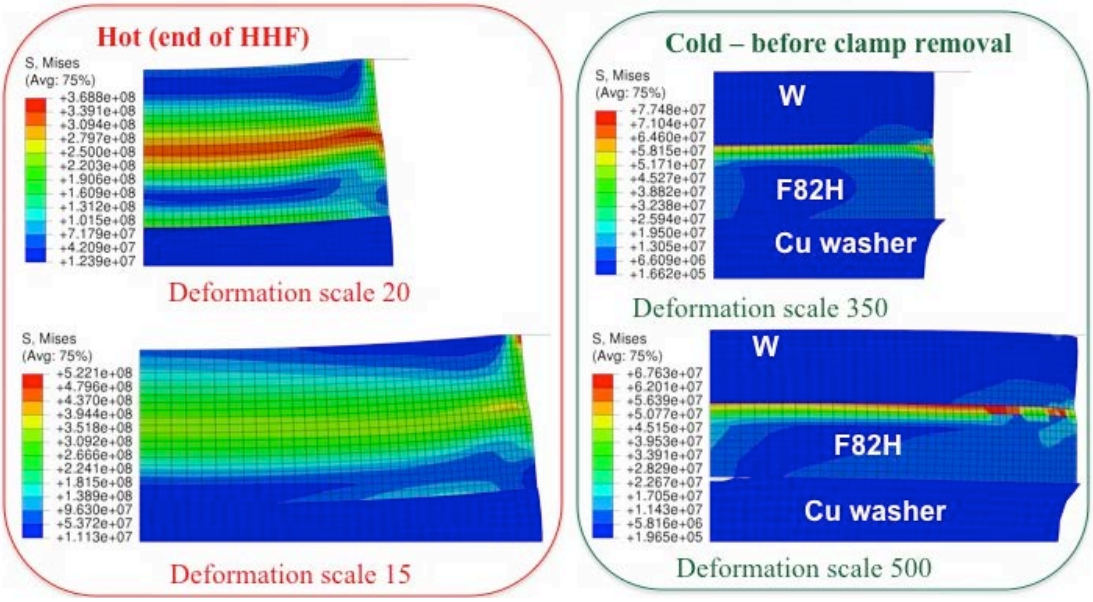

Figure 72. Von Mises stress results when specimen is at high temperature (Hot), i.e., right at the end of the HHF, and at room temperature (Cold) for 6mm specimens (top line of figures) and 10mm specimens (the last line of figures) for the case when TCC per unit area F82H-Cu was 5,000 [W/m^{2}K].

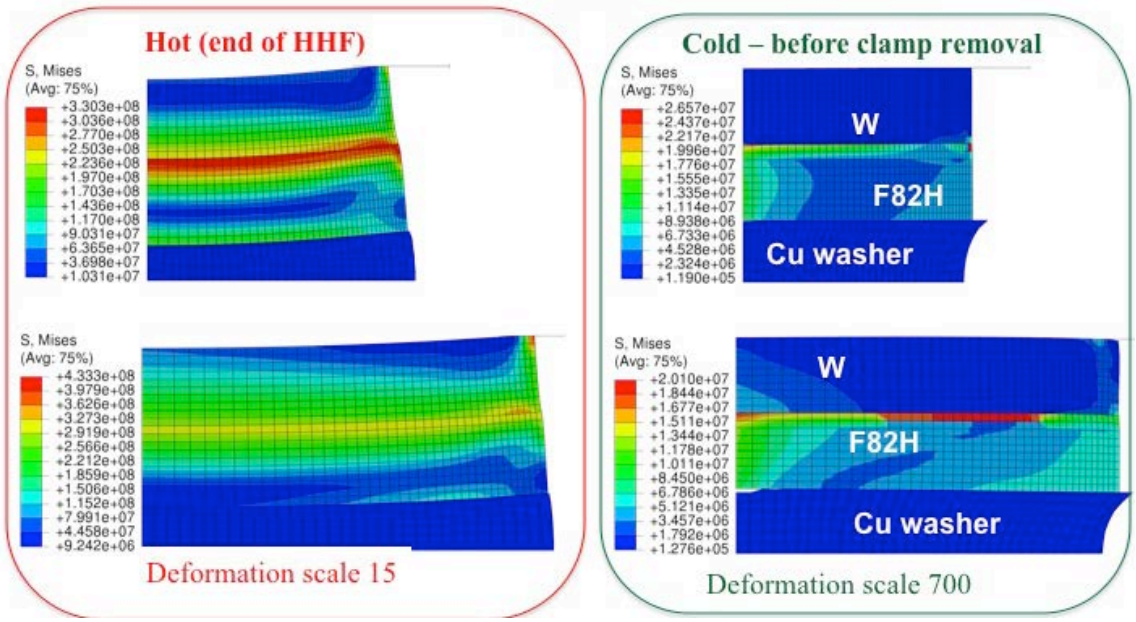

Figure 73. Von Mises stress [Pa] results when specimen is at high temperature (Hot), i.e., right at the end of the HHF, and at room temperature (Cold) for 6mm specimens (top line of figures) and 10mm specimens (the last line of figures) for the case when TCC per unit area F82H-Cu was 7,000 [W/m^{2}K].

FUTURE PLANS

Efforts are now focused on:

- Conducting high-heat flux testing with non-irradiated specimens for the joint US/Japan PHENIX program, and
- Understanding the deformation during HHFT using thermo-mechanical simulation of HHFT.

7. SPECIAL PURPOSE MATERIALS – IRRADIATION RESPONSE OF NEXT GENERATION HIGH TEMPERATURE SUPERCONDUCTOR TAPES

P.D. Edmondson (edmondsonpd@ornl.gov), K.J. Leonard, F.A. List III, A.M. Williams, J.W. Geringer and T. Aytug

OBJECTIVE

This work is evaluating the irradiation response of the newest generation of coated conductors based on rare earth doping of $YBa_2Cu_3O_{7-x}$ (YBCO) high temperature superconductors. The materials under investigation represent different methods for enhanced flux pinning for improved performance under externally applied magnetic fields. Response of these tapes to neutron irradiation is examined.

SUMMARY

Post irradiation electrical characterization of two high temperature superconducting tapes (HTS) was performed. Zr-(Gd,Y)$Ba_2Cu_3O_7$ and (Dy,Y)$Ba_2Cu_3O_7$ tapes commercially available from SuperPower and American Superconductor, respectively, are part of a new generation of conductors which utilize nano-particles and correlated defect structures within the films to produce tapes capable of use under higher applied magnetic fields than earlier $YBa_2Cu_3O_7$ (YBCO) tapes. Neutron exposures between $6.54x10^{17}$ and $1.12x10^{19}$ n/cm^2 (E>0.1MeV) at 75-80°C, produced losses in critical current (I_c) in tests under applied fields up to 0.5 Tesla at 77 K. Increases in I_c loss with dose occurs gradually in the (Dy,Y)$Ba_2Cu_3O_7$ conductor, but is rapid in the Zr-(Gd,Y)$Ba_2Cu_3O_7$ with transport current unable to be measure at fluence $>6.54x10^{17}$ n/cm^2.

PROGRESS AND STATUS

Ion irradiation, 5 MeV Ni and 25 MeV Au, response of the $GdBa_2Cu_3O_7$, Zr-(Gd,Y)$Ba_2Cu_3O_7$ and (Dy,Y)$Ba_2Cu_3O_7$ tapes were previously investigated. While, predominantly within the electronic stopping regime, the ion irradiation conditions studied of these HTS tapes was within a lower electronic to nuclear stopping ratio (S_e/S_n) as compared to earlier studies. This revealed that there was a significant sensitivity of YBCO based conductors to electronic stopping effects, but also offered a promising evaluation that the rare-earth and nano-particle doped conductors may perform well under neutron irradiation.

Based on those preliminary results from ion irradiation studies, work on the $GdBa_2Cu_3O_7$ tapes produced from SuperPower was not continued. This was due to the greater sensitivity of this material to ion irradiation compared to the Dy and Zr-doped conductors. While performance was improved over conventional YBCO films, under irradiation the Gd_2O_3 nano-particles present within the $GdBa_2Cu_3O_7$ films (which in addition to stacking-fault and intergrowth gives the conductor improved in-field performance) begin to dissolve with increasing irradiation fluence.

The evaluation of the electrical properties and the corresponding microstructural evolution of the Zr-(Gd,Y)$Ba_2Cu_3O_7$ and (Dy,Y)$Ba_2Cu_3O_7$ tapes under neutron irradiation were further explored.

Experimental Procedure:

Neutron irradiation capsules for High Flux Isotope Reactor (HFIR) exposures in the hydraulic port facility utilize a square internal cross-section rabbit design loaded with internal packets containing samples, Figure 74.

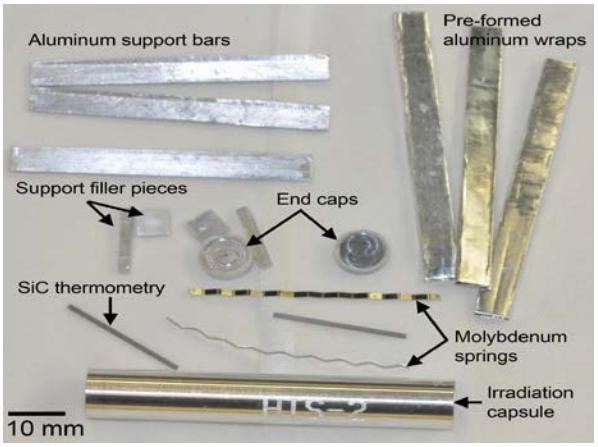

Figure 74. Components of the HTS-2 capsule containing HTS and TE samples. The HTS samples (not shown) are placed on the aluminum support bars and wrapped in aluminum sheet.

Additional samples of thermoelectric (TE) materials were also included in two of the four-irradiation capsules as part of a separately funded project. Each internal packet contains samples of one type of HTS sample or the TE materials. High purity aluminum bars provide mechanical support for the flexible HTS tapes, with the tapes and bars over-wrapped with high purity aluminum foil to form a packet. The HTS samples within the wrapped packet are placed against the internal wall of the irradiation capsule. Irradiation temperatures are estimated to be ~75-80°C. SiC temperature monitors contained within the capsules remains to be evaluated. The targeted fluence were $5x10^{17}$, 10^{18}, $5x10^{18}$ and 10^{19} n/cm^2 (E>0.1 MeV). Mo-Springs are inserted between the sample packets to hold the packets up against the internal wall of the irradiation capsules. This ensures the lowest possible irradiation temperature for the HTS materials.

The irradiations were performed during HFIR cycle 456, in October 2014. The actual fluence based on the recorded time within the core and position for the four capsules during the irradiation were $6.54x10^{17}$, $1.30x10^{18}$, $7.00x10^{18}$ and $1.12x10^{19}$ n/cm^2 (E>0.1MeV).

The aluminum-wrapped HTS samples were unloaded at the Irradiated Materials Examination and Testing facility. The packets were removed from the irradiation capsules, placed in paper tubes containing desiccant, loaded into shielded containers with additional desiccant and sealed in plastic bags. Final sample unloading from the packets was in the low-activation materials development and analysis laboratory. Due to high removable contamination levels of Sb-124 on the high dose HTS packets, produced from a degraded $BiSb_3Te_6$ thermoelectric sample in the adjacent packet, the high dose HTS packets cannot be safely disassembled until October 2015 when activity levels decay to manageable levels.

Field oriented dependence of the critical current (I_c) at 0.5 Tesla and 77 K was tested for the irradiated HTS samples as well as I_c versus field for applied fields parallel to the ab plane of the films up to 1 Tesla. Before the irradiation, all the YBCO films were patterned into a strip configuration (removing the silver "shunt" over layer in the process) with silver contact pads and a 1-mm-long bridge with a width of either 1.00 mm or 0.200 mm, using a focused-electron-beam scribing system. Prior to post-irradiation electrical testing a strip of indium was applied to the silver pads at pressed copper injection areas of the probe contact points, which limited the electrical contact resistance to between ~ 10^{-6} and 10^{-4} ohm.

Results and Discussion:

Two tapes each of the Zr-(Gd,Y)$Ba_2Cu_3O_7$ and (Dy,Y)$Ba_2Cu_3O_7$ materials (Zr-YBCO and DyBCO from herein), were tested for the $6.54x10^{17}$, $1.30x10^{18}$ and $7.00x10^{18}$ n/cm^2 (E>0.1MeV) irradiation conditions. The results for each irradiated tape were compared to the pre-irradiation characterization data. Very little difference was observed between the pre-irradiated electrical property data for the samples of a given material type. The post-irradiation data was also consistent between the two HTS samples of a given materials type for each irradiation condition. Therefore, repeatability in the experiment was found to be good with no extraneous results.

Data for the DyBCO tapes is presented in Figure 75, showing the pre- and post-irradiation angular dependence of I_c at 0.5T and 77 K and I_c as a function of applied magnetic field (ϕ=90° at 77K).

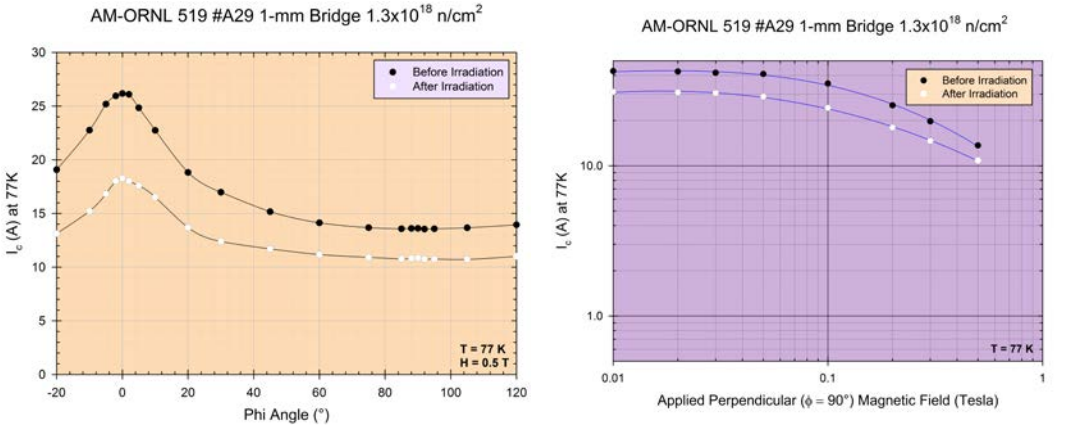

Figure 75. Pre- and post-irradiation values of I_c as a function of applied field direction and magnitude up to 0.5 Tesla, tested at 77 K for the (Dy,Y)$Ba_2Cu_3O_7$ conductor. (a) $1.30x10^{18}$ and (b) $7.00x10^{18}$ n/cm^2 (E>0.1MeV).

The DyBCO tapes showed a gradual loss in transport current with irradiation dose. While testing of the $1.12x10^{19}$ n/cm^2 dose samples could not be completed as previous discussed, transport currents are expected to be even lower and may not be able to be effectively measured. Loss in the I_c curve as a function of applied field may cross the pre-irradiation values at fields much greater than those tested, as

was observed in the samples ion irradiated in previous tests. The loss in the I_c with dose is likely attributed to defect generation within the 123-structured matrix of the film. This is most likely in the form of amorphous regions initiating at fluence lower than that of those conditions tested, with the amorphous regions growing and eventually restricting current flow. Based on the consistency in the shape of the angular dependence curves, it is not expected that a significant change has occurred in the size, shape and distribution of the nano-particle Dy_2O_3 particles within the conductor film.

The post-irradiation data for the Zr-YBCO could only be measured for the $6.5x10^{17}$ n/cm^2 irradiated material, as transport currents for the higher dose samples were below detection level of the instrumentation used. The data for the two Zr-YBCO samples from the HTS-1 capsule are not shown here, but the shape of the angular field dependence curves for the Zr-YBCO samples suggests a significant change in the distribution of the $BaZrO_3$ nano-particles within the conductor. The I_c loss near ϕ=90°, suggests the loss of c-axis nano-particle alignment within the material.

Improvements in flux pinning through irradiation-induced defect creation has been seen in YBCO through ion, proton, electron, and neutron irradiation. Increases in critical current density (J_c) have been generally measured following neutron irradiation to fluence > $1x10^{16}$ n/cm^2 (E>0.1 MeV) and peak around 0.6-$1x10^{18}$ n/cm^2. Increases in the irradiated J_c over un-irradiated values $(J_c^{irrad}/J_c^{unirr})$ are between 2 to 4 times for YBCO irradiated to $4.4x10^{21}$ n/m^2 (E>0.1 MeV) for measurements between 50 and 77 K. By comparison, increased critical current values of Nb_3Sn are approximately 1.5 times un-irradiated values following, 14 MeV neutron irradiation to $1.78x10^{17}$ n/cm^2. The decreased sensitivity of J_c is in-part due to the larger coherency length (ξ) of Nb_3Sn than YBCO (3 nm versus 1.5 nm at 0 K), which reduces the net effect of the elementary pinning force of the defects.

The lack of improvement in transport properties of the neutron irradiated conductors of this study may be due to several factors, some of which are currently being examined. However, improvements in I_c may have occurred at fluence below that which was tested. A fluence of ~ $5x10^{17}$ n/cm^2 is the lowest achievable using the HFIR hydraulic port facility without increased uncertainties related to accurate recording of dwell time within the core due to the high nominal flux (1-$2x10^{15}$ n/cm^{2}s). Other port locations can provide lower flux conditions, but increases complexity of the experiment as well as costs. The magnitude increase in J_c following irradiation is also highly sample dependent, with variations in literature data attributed to sample defect conditions prior to irradiation or to secondary phases present in the YBCO. For effective flux pinning, the defect size must be around the coherency length, which is dependent on temperature. The small coherence length in YBCO makes point defects effective at pinning of vortices. Small pre-irradiation defects may not contribute to pinning at higher test temperatures (near 77 K), while larger defects are efficient pinning sites at higher temperatures and lower fields. Therefore, effective pinning from neutron induced defects or changes to pre-existing defects may not be observed even within the lower exposure doses due to the higher post-irradiation characterization temperatures used in this study. Furthermore, the presence of non-conducting nano-particles that are intentionally added to improve in-field transport properties of the conductors may result in more rapid reduction in the viable superconducting pathway for current as radiation-induced amorphization of the conductor occurs with dose.

FUTURE PLANS

The next step in analyzing the neutron irradiated Zr-$(Gd,Y)Ba_2Cu_3O_7$ and $(Dy,Y)Ba_2Cu_3O_7$ tapes will involve microstructural characterization. The TEM specimens have been prepared by focused ion beam milling of the two HTS materials exposed to $6.5x10^{17}$ n/cm^2. The higher dose materials will also be examined. Further analysis of the ion irradiated samples from previous work is also planned for the final comparison of microstructural evolution under irradiation.

8. COMPUTATIONAL MATERIALS SCIENCE

8.1 STRENGTHENING DUE TO RADIATION INDUCED OBSTACLES IN Fe AND FERRITIC ALLOYS

Yu. N. Osetskiy (osetskiyyn@ornl.gov) and R. E. Stoller

OBJECTIVE

The purpose of this research is to understand atomic level strengthening mechanisms in materials by radiation induced localized microstructural features such as voids, gas-filled bubbles, secondary phase precipitates and oxide particles. These features act as obstacles to dislocation motion and cause radiation induced hardening and embrittlement. Currently, we are investigating the map of mechanisms depending on the obstacle type and size.

SUMMARY

Irradiation of structural alloys by neutrons and ions lead to formation of a high density of nano-scale objects such as secondary phase precipitates, voids and gas-filled bubbles. These objects are obstacles to dislocation motion and cause changes in mechanical properties. In order to predict materials behavior these obstacles must be characterized and their individual strength be estimated. The only technique that allows this at the scale of nano-meters is classical molecular dynamics (MD). In this work we modeled vacancy voids, He-filled bubbles, Cu precipitates and rigid inclusions in bcc-Fe matrix. At the current stage of the research we investigated ½<111>{110} edge dislocation. During motion this dislocation cannot change its glide plane (by cross-slip) to avoid interaction with obstacles and therefore produces a maximum amount of strengthening. The results obtained in this research will be used to improve theoretical prediction of mechanical property changes.

PROGRESS AND STATUS

We recently improved the atomic scale model for dislocation-obstacle interaction by introducing a procedure for estimating the accuracy of the calculated shear stress. For this we used the case of a single dislocation moving in a perfect crystal under the applied strain rate $\dot{\varepsilon}$ = 5x10^6 s^{-1}. The dislocation velocity depends on the applied strain rate and dislocation density and in the applied model can be estimated as: $v_D = \dot{\varepsilon}\, L_b H/b$ and varied from ~16 m/s to ~49 m/s in the smallest (~2x10^6 atoms) and largest (~6x10^6 atoms) crystals, respectively. The applied strain generates a shear deformation of the modeled crystal which in turn generates shear stress which forces a dislocation to move. In MD modeling the instantaneous stress fluctuates depending on the temperature and dislocation velocity (i.e. applied strain rate.) Figure 76 shows the variation of the instantaneous shear strain, τ, calculated every 100 time steps (the time step for motion equation integration is equal to 2fs) during the steady state motion of a ½<111>{110} edge dislocation under 5x10^{6}s^{-1} applied strain rate modeled at 300 K over 2.5 ns. One can see that its value fluctuates from <-20 MPa to almost 40 MPa. Statistical treatment resulted in the mean value $\bar{\tau}$=3.53 MPa (solid line in Figure 76) and a standard deviation σ=9.8 MPa (the values of ($\bar{\tau} \pm \sigma$) are indicated by point-dash lines in Figure 76). Here we accepted the standard deviation as providing the most accurate estimate of the uncertainty in the mean shear stress. However, in the case of dislocation-obstacle interactions the uncertainty in the shear stress estimate should be higher because this process is far from the case of equilibrium steady state dislocation motion considered in Figure 76. It is difficult to estimate this uncertainty for it depends on the temperature and applied strain rate. We cannot estimate the mean shear stress by a simple time average as in Figure 76 for the interaction process is limited in time. More important is the obstacle release stress that exists over a limited and rather short time depending on

the strain rate applied. As an example we illustrate the typical stress-strain, $\tau(\varepsilon)$, dependence obtained when modeling the interaction between a moving dislocation and a 2 nm bubble with He/Vac=0.5, Figure 77. The grey line presents the instantaneous shear stress calculated every 100 time steps. One can see that stress fluctuations are rather big and quite similar to that in Figure 76 for the steady-state dislocation motion. To extract a reasonably averaged instantaneous value of τ we used adjacent average (AA) processing of the instantaneous data. The AA processing data with 5, 10 and 20 neighboring points (AA5, AA10 and AA20) are shown by green, black and red lines in Figure 77. Data for AA20 show reasonably smooth behavior. We used this treatment to produce all of the results reported here, assuming as well that the uncertainty in estimating the shear stress values is the same as for the steady state dislocation motion at the same temperature where its lower limit is >10 MPa. Note that processing parameters (the number of neighboring points) and the shear stress uncertainty (standard deviation of the mean stress) depend upon the model strain rate and temperature; both values decrease at low temperature and $\dot{\varepsilon}$ and increase at higher temperatures and $\dot{\varepsilon}$. The maximum on the processed $\tau(\varepsilon)$ curve indicates the critical resolved shear stress (CRSS) which is the measure of the obstacle strength for a given interaction geometry.

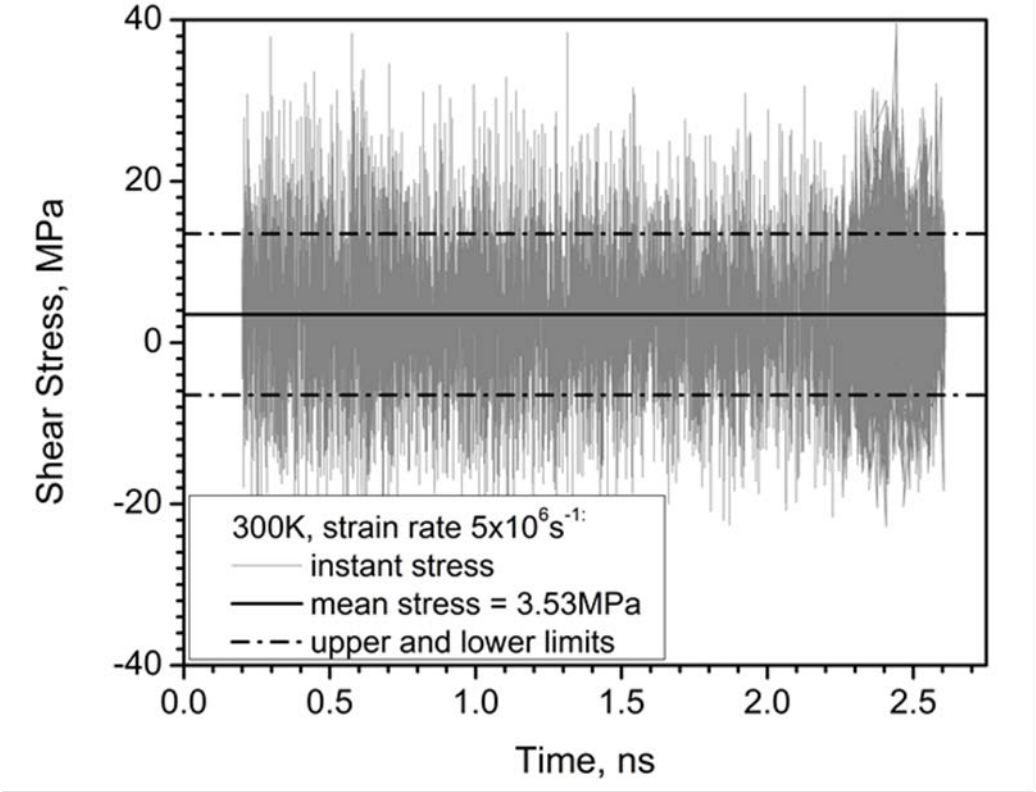

Figure 76. Modeling of steady state motion of ½<111>{110} dislocation at a strain rate of $5x10^6 s^{-1}$ at 300K: grey line - instantaneous shear stress calculated every 100 time steps ; solid black line - mean value, 3.8 MPa, estimated over 2.5 ns, point-dash lines – mean stress plus/minus standard

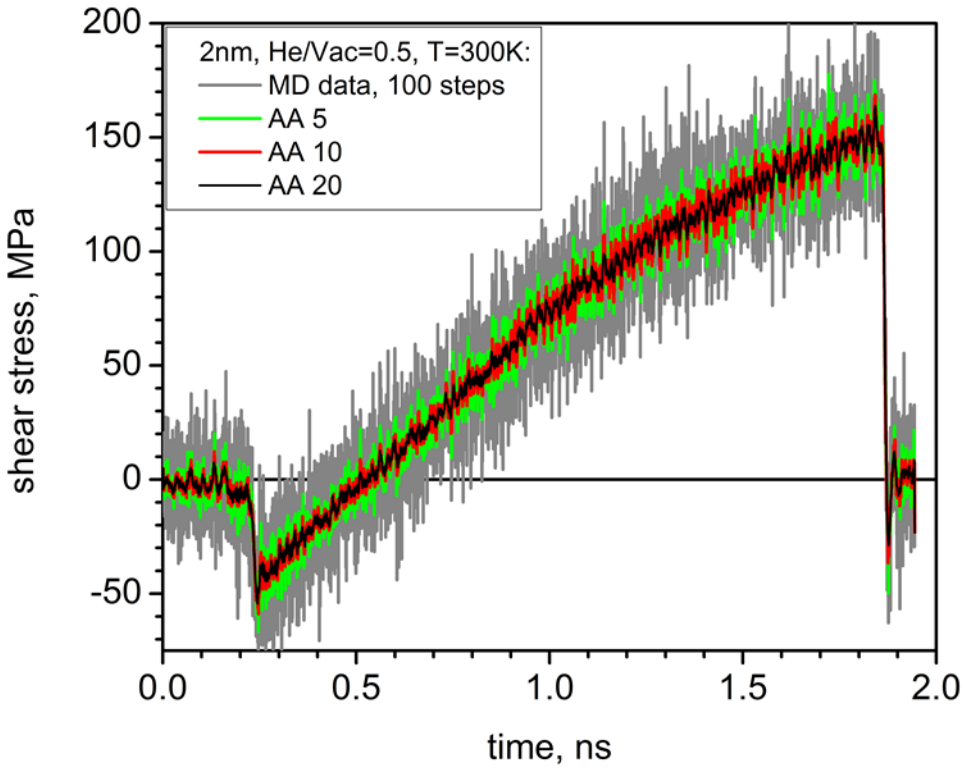

Figure 77. Stress-Strain curve observed during dislocation interaction with 2 nm bubble with He/Vac=0.5: grey line - instantaneous shear stress calculated every 100 time steps; green, red and black lines – processes by adjacent average over 5, 10 and 20 neighbor points respectively.

We now have finished modeling obstacles up to 7 nm in diameter and continue with 8 nm obstacles. This demands larger model crystals, >$8x10^6$ atoms. Unlike small obstacles, <4 nm, which show individual mechanisms with different hardness, large obstacles are strong and according to the dislocation line shape that adopts a long dipole of screw dislocations the mechanism is assumed to be the Orowan-type. However, as our modeling has demonstrated, the classical Orowan mechanism [1] i.e. with formation of a sheared dislocation loops around the obstacle is applicable only to rigid obstacles. Other obstacles demonstrate the shear mechanism with similar strength. This can be seen in Figure 78 where a comparison of CRSS is presented for different obstacles of different sizes. Rigid obstacles are found to be the strongest. The dependence of their strength is also exceptionally strong within the range studied as can be seen in Figure 79 where the comparison of atomistic modeling of rigid obstacles from 1 to 7 nm in diameter at 300 K (circles) with theoretical estimation from [2,3] (lines) is presented.

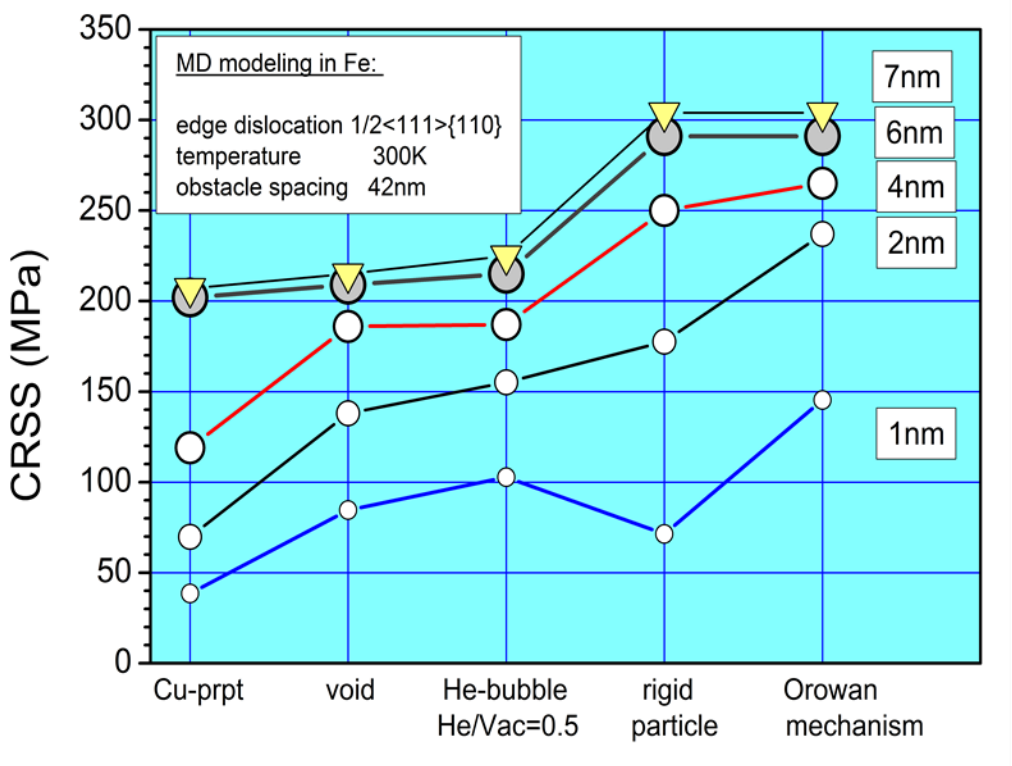

Figure 78. Critical resolved shear stress for different obstacles of different size obtained by molecular dynamics modeling at 300 K.

Our data demonstrate that obstacles a few nano-meters in diameter have individual dependence of their strength versus their size. This is especially important for the irradiation conditions for which the majority of obstacles are typically small, within a few nano-meters. Our calculations provide parameters for the prediction of mechanical property changes due to irradiation. This work was already started within the corresponding task. Within the current task we now are finalizing investigation of the interaction geometry effect for large obstacles. The main issue is if simple use of a mean defect size is appropriate for strengthening estimation. We already have some evidence that interaction between an obstacle and a dislocation gliding above and below its equator can be strongly asymmetric for some obstacles. In this case the simple use of the dispersed barrier hardening model [4] with a mean obstacle size can be inaccurate, especially for small obstacles.

FUTURE STUDIES

1. Finalize modeling of edge dislocation interaction with He-filled bubbles up to 8-10 nm diameter.
2. Extend dislocation-obstacle interaction to ½<111> screw dislocation.
3. Develop the enhanced dispersed barrier hardening model to be able to include dislocation obstacle interaction mechanisms revealed in atomic-scale modeling.
4. Extend the modeling program to dislocation-type obstacles such as dislocation loops. So far dislocation loops are treated in the same way as inclusions, however their interaction with dislocations is quite different and this must be taken into account.

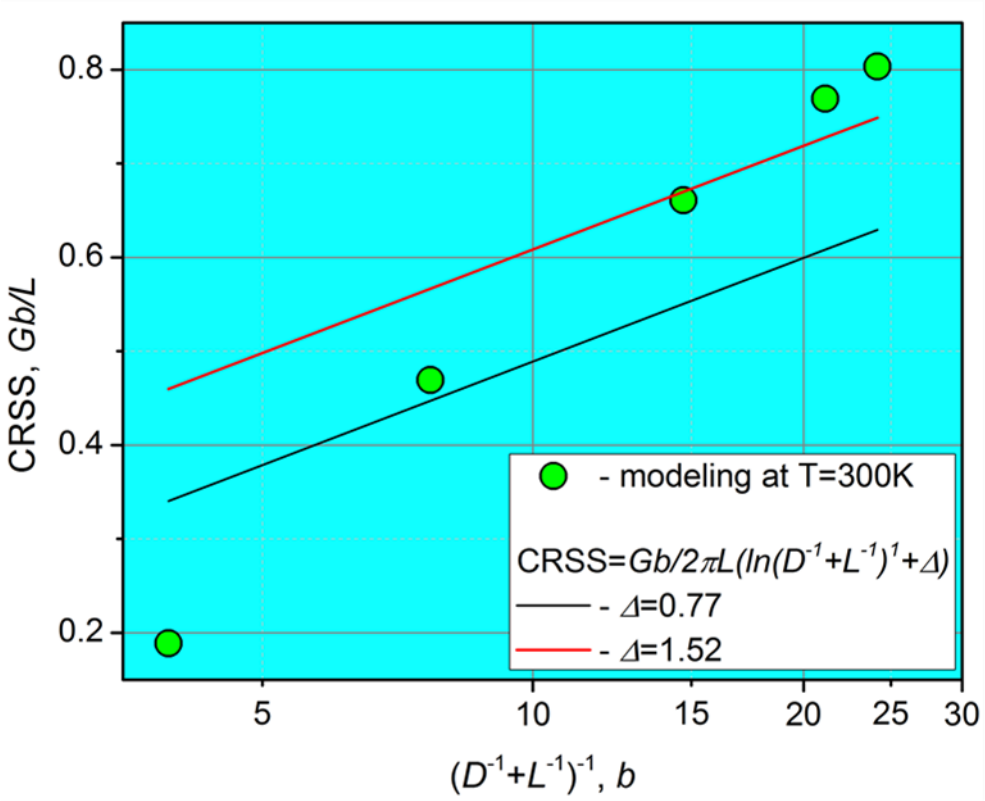

Figure 79. Critical resolved shear stress in reduced units as a function of harmonic mean of an obstacle diameter, D, and spacing between them along the dislocation line. Circle - rigid inclusions simulated in current work, lines are dependences obtained in dislocation dynamic modeling for Orowan mechanism (black line) and void (red line) in [1,2].

REFERENCES;

1. Orowan E., A type of plastic deformation new in metals, *Nature*, 1942, vol.149, p.643.
2. Bacon, D. J., Kocks, U. F., and Scattergood, R. O., 1973, *Phil. Mag.*, 28, 1241.
3. Scattergood, R. O., and Bacon, D. J., 1982, *Acta metall.*, 30, 1665.
4. Seeger A., Proc. 2nd UN Int. Conf. on Peaceful Uses of Atomic Energy (Geneva, Switzerland, September 1958), 1058, vol.6, p.250.

8.2 MOLECULAR DYNAMICS MODELING OF ATOMIC DISPLACEMENT CASCADES IN 3C-SiC

German Samolyuk, (samolyukgd@ornl.gov), Y.N. Osetsky and R.E. Stoller

OBJECTIVE

The purpose of this effort is to characterize the nature of primary radiation damage in SiC, to provide a basis for understanding the experimentally observed fluence-temperature map of the irradiated microstructure.

SUMMARY AND STATUS

Early in Fiscal Year 2015 we finalized calculations of 10 keV and 50 keV pka atom cascades in SiC using the two most popular interatomic potentials. The results were obtained for the number of stable point defects using the Tersoff/ZBL and Gao-Weber/ZBL (GW) interatomic potentials. The GW potential appears to give a more realistic description of cascade dynamics in SiC, but still has some shortcomings when the defect migration barriers are compared to the *ab initio* calculations. The results have been published in the Journal of Nuclear Materials 465 (2015) 83-88.

Additional computational resources have been used for this work through collaboration with Japan Atomic Energy Agency.

8.3 PROPERTIES OF VACANCY COMPLEXES WITH H AND He IN TUNGSTEN FROM FIRST PRINCIPLES

G.D. Samolyuk (samolyukgd@ornl.gov), Y.N. Osetsky, and R.E. Stoller

OBJECTIVE

Tungsten and its alloys are the primary candidate materials for plasma facing components in fusion reactors. The material is exposed to high-energy neutrons and high fluxes of helium and hydrogen atoms. The He and H atoms, being very mobile in the defect-free bulk material, strongly affect the microstructure evolution, mainly through changing the stability of vacancy-type defects. We are studying the properties of single vacancies and the interaction with hydrogen in W using a first principles approach (density functional method, [DFT]). We also will calculate the interaction of vacancies in complexes of up to six vacancies and their interaction with H/He atoms. The binding energies obtained will be used in mean-field type modeling of deuterium/helium implantation in tungsten for comparison with experimental observations.

SUMMARY

It was demonstrated that the formation energy of single vacancy and six vacancies clusters, the largest cluster investigated in current research, converged for model cells containing 250 atoms. This size is therefore large enough to reproduce interaction and formation energies for both H and He atoms. A single He atom is strongly attracted to a vacancy with binding energy of 4.6 eV. The di-vacancy clusters are unstable in first nearest neighbor (1NN) and second nearest neighbor (2NN) positions and weakly attract each other at third nearest neighbor (3NN) positions. The introduction of H/He stabilizes di-vacancies. The compact 6 vacancy cluster is stable with binding energy of 2 eV.

PROGRESS AND STATUS

As an initial effort we analyzed the existing scientific literature on the subject. The analysis demonstrates that there are contradictions in even such simple values as di-vacancy interaction results. Thus we started our research with the calculation of properties of the single vacancy.

All calculations have been done using the plane-wave basis set and PAW pseudo-potential for W with semi core p-states in the valence band, as is realized in the VASP package. The Perdew, Burke, and Ernzerhof exchange-correlation function was used. The Brillouin zone summations were carried out over a 4×4×4 BZ grid for the model cell containing 6x6x6 cubic unit cells (432 atoms) and the grid was increased to keep the same k-pint density in the modeling cell of smaller size. The plane wave energy cut off was 360 eV. The atomic structure was optimized until the forces to all atoms dropped below 0.001 Ry/A.

In Figure 80 the result for properties of a single vacancy as a function of model cell size is presented. The results shown in blue correspond to the case of constant lattice parameter of a perfect structure; in the second case, shown in red, the lattice parameter was recalculated to maintain constant volume per atom.

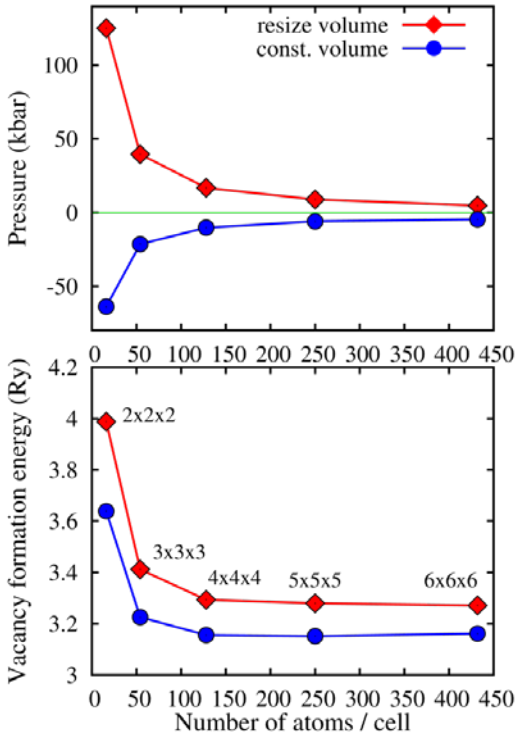

Figure 80. The total pressure and vacancy formation energy as a function of model cell size. Two types of calculated results are presented. In the first, shown by the red line with diamonds, the volume per atom was kept constant. Whereas, in the blue line with circles - the constant model cell size results are presented.

As can be seen, the binding energy has converged for the 4x4x4 model cell containing 128 atoms, however to keep pressure in the system close to zero a 5x5x5 model cell containing 250 atoms is necessary. The comparison with other available results is presented in Table 13.

.

Table 13. Single vacancy formation energy, in eV, as a function of model cell size together with previously published results.

N_{at}	Current	[1]	[2]	[3]
54	3.23	3.23		
128	3.16		3.56	3.17
250	3.15			
432	3.16			

[1] L. Ventelon, F. Willaime, C.-C. Fu, M. Heran, I. Ginoux, JNM 425 (2012) 16
[2] P. M. Derlet, D. Nguyen-Manh, and S. L. Dudarev, PRB 76 (2007) 54107
[3] D. Kato, H. Iwakiri, K. Morishita, JNM 417 (2011) 1115

The results obtained are in good agreement with results of existing DFT calculations, except for the formation energy obtained in reference [2], which is in contradiction with all other available data.

Interstitial H/He atoms occupy tetrahedral position in perfect W. The difference between energies of an interstitial in tetrahedral and octahedral positions is equal to -0.37 and -0.25 eV for H and He respectively. These energy differences are in agreement with results obtained in Ref. [4].

In the presence of a vacancy, H or He atoms occupy distorted octahedral positions, shown in Figure 81 as a grey color sphere.

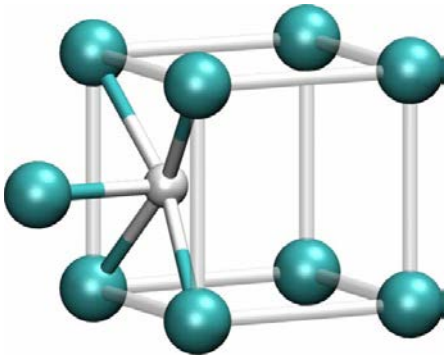

Figure 81. Distorted octahedral position occupied by H/He atom shown by grey sphere in the presence of vacancy.

While the vacancy formation energy converged in the super cell of size 128 atoms (see Figure 80), to preserve total pressure in the system close to zero we needed a system of size 452 atoms. The modeling in smaller size model cells has been done for comparison with existing results and to test the convergence. The presence of He atoms, according to our results, increases the total pressure by 1 kbar. It points out that the presence of He in one of the vacancies should lead to binding of H/He with a vacancy and increase the di-vacancy binding energy. The binding energy of one He atom with a vacancy is equal to 4.64 eV, which is in agreement with previous results, 4.5 eV obtained in the 4x4x4 modeling cell [4].

In agreement with result obtained for the smaller model cell (250 atoms), two vacancies placed in the 1NN and 2NN neighbors positions repulse each other. The binding energies are equal to -0.11 and -0.46 eV respectively (see Table 14). The interaction between vacancies in 3NN neighbor positions is attractive and the binding energy is equal to 0.05 eV.

The presence of a H atom changes 1NN and 2NN di-vacancy interactions to attractive, with binding energy equal to 1.51 and 1.42 eV of 1NN and 1NN respectively, Table 15.

Table 14. Di-vacancy binding energy in eV.

N_{at}	432	128	54 [1]	128 [2]	128 [3]
1NN	-0.11	-0.16	-0.03	0.41	-0.16
2NN	-0.46	-0.48	-0.47	0.19	-0.47
3NN	0.05				0.13

Table 15. Di-vacancy binding energy in presence of H atom in one of the vacancies, in eV.

N_{at}	432	128	128 [3]
1NN	1.51	1.30	1.80
2NN	1.42	1.38	2.15

In the presence of a He atom the di-vacancy binding energy changes to 0.13 eV, i.e. the interaction is slightly attractive.

Similar to other materials, in tungsten the large size vacancy clusters started to be stable. Thus, the binding energy for 6 vacancies, shown in Figure 82, is equal to 2.02 eV in 6x6x6 model cell (1.98 in 5x5x5 and 1.89 eV in 4x4x4).

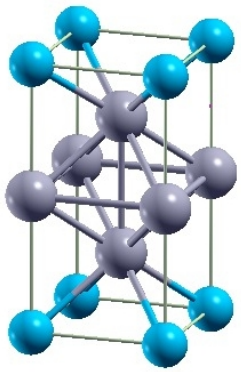

Figure 82. Six vacancy cluster.

FUTURE PLANS

We plan to extend our formation and binding energy DFT calculations to vacancy clusters containing 3, 4 and 5 vacancies. Also the binding energies of hydrogen with these clusters will be investigated.

9. INTERNATIONAL COLLABORATIONS

9.1 US-JAPAN COLLABORATION ON RAFM STEEL

Y. Katoh (katohy@ornl.gov), M. Ando (JAEA), H Sakasegawa (JAEA)

OBJECTIVE

This collaboration between the Department of Energy (DOE) and the Japan Atomic Energy Agency (JAEA) jointly pursues activities using the advanced capabilities for materials irradiation and post-irradiated examination at Oak Ridge National Laboratory, especially the High Flux Isotope Reactor (HFIR). The focus is on ferritic steels and other advanced materials, especially the development of the material database for the design of facilities beyond ITER. The goals include achieving DEMO-relevant performance data on reduced activation ferritic/martensitic steels neutron irradiated in HFIR to high levels of displacement damage (>30 dpa).

SUMMARY

The DOE-JAEA collaboration continues to make steady progress in building the materials data base for the reduced activation ferritic martensitic (RAFM) F82H steel, with irradiations to displacement damage levels of 80 dpa. The goal of this project is to accumulate the principal irradiation property data for F82H, contributing to the materials data base for the blanket structural design of a fusion DEMO reactor.

PROGRESS AND STATUS

This DOE-JAEA Project is the US-Japan long-running collaboration now in its 32nd year. The objective of this project is to perform irradiation and post-irradiation examination (PIE) of first wall and blanket structural materials for fusion reactors. Irradiation experiments for exposures up to 20 dpa were started for the RAFM steel and several BCC alloys in the HFIR Phase 3 program (1995-2000). In the Phase 4-5 programs (2000-2009), three main tasks were conducted: (1) To improve the irradiation resistance of RAFM, especially the fracture toughness, (2) To obtain data for high-dose irradiated RAFM and oxide dispersion strengthened steels, up to 80 dpa, and (3) To examine the effect of helium on mechanical properties and microstructures using boron and/or nickel-doped RAFM and Ni/Al coating techniques. Four HFIR target capsules (JP26, 27, 28 and 29), one RB capsule (RB15J) and several rabbits were irradiated in these Phases. Primary PIE for JP26 and JP27 capsules is almost complete. For RB15J capsule, some PIE remains. Irradiation of the high-dose JP28&29 capsules was completed in 2013. In the Phase 6 (2009-2014) program two additional target capsules (JP30&31) were irradiated to obtain the irradiation effects on joined sections of RAFM (TIG weldments, EB weldments and HIP joints). Several high-dose rabbit capsules (containing RAFM and SiC/SiC composites) were also irradiated. Figure 83 shows the current status of data obtained and the planned PIE for irradiated F82H base metal and several weldments (including results from irradiations in the earlier FFTF/MOTA program and in Japanese research reactors).

Tensile tests (base metal) for JP28 and JP29 capsule specimens were performed and showed that irradiation hardening and embrittlement occurred with increasing dose, though they had been expected to be saturated around 20 dpa, based on past research. Additionally, a new RB capsule for HFIR (RB19J) in the post-phase 6 program is being prepared with other collaborating programs. The objectives of the irradiation are evaluation of the impact of stress constraint factors on fracture behavior of irradiated RAFM using notched tensile specimens and bend bar type toughness specimens with different a/W, and demonstration of small specimen toughness evaluation based on Weibull stress concept.

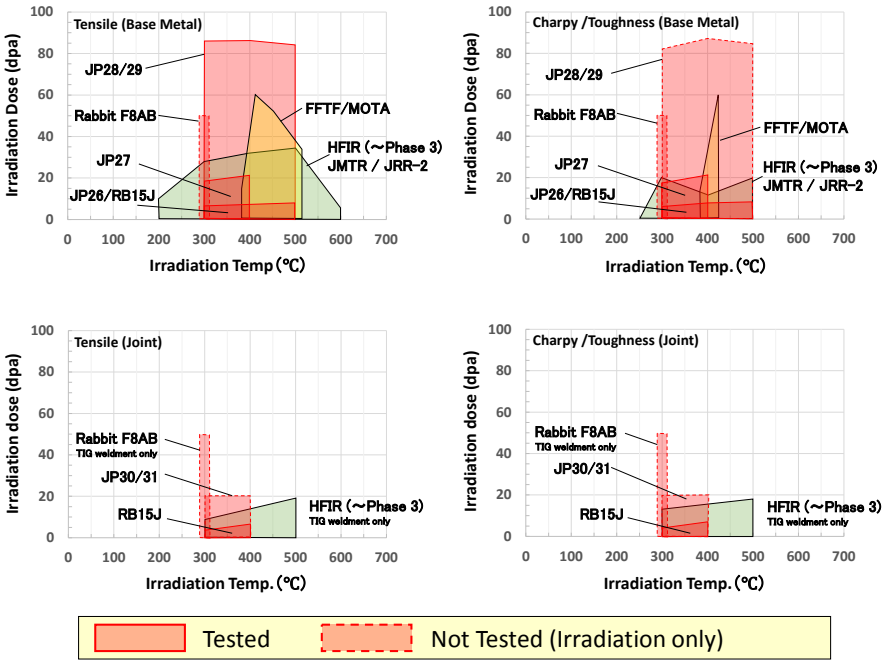

Figure 83. Status of accumulated data for F82H-IEA irradiated in several fission reactors.

FUTURE PLANS

The main PIE on specimens from target capsules (JP28, 29, 30 and 31) and rabbit capsules (F8AB and F11AB) from phase 4-6 programs will continue. Completion of the experiment fabrication and beginning of irradiation of RB19J will occur in Fiscal Year 2016.

9.2 US-JAPAN PHENIX COLLABORATION

Y. Katoh, (katohy@ornl.gov), A.S. Sabau, L.M. Garrison, X. Hu , Y. Ueda (Osaka University) and K. Tokunaga (Kyushu University)

OBJECTIVE

The PHENIX Project on the Technological Assessment of Plasma Facing Components for DEMO Reactors is the current US/Japan Fusion Research Collaboration Project that started in April 2013. The goal of the project is to evaluate the following critical issues for plasma-facing components under divertor conditions of fusion reactors: (1) heat transfer, (2) mechanical properties, (3) neutron irradiation effects, and (4) tritium retention and permeation. The project participants are Oak Ridge National Laboratory (ORNL), Idaho National Laboratory, Sandia National Laboratory, Georgia Institute of Technology, National Institute for Fusion Science of Japan, and various Japanese universities. The ORNL participates in Task 1 - high heat flux testing, Task 2 - neutron irradiation effects, and neutron irradiation in High Flux Isotope Reactor (HFIR) in support of all research tasks.

SUMMARY

In Fiscal Year (FY) 2015, high-heat flux testing (HHFT) of five W-F82H specimens, supplied by the Japanese collaborators in the PHENIX program, was successfully conducted at ORNL in collaboration with Dr. K. Tokunaga of Kyushu University. Other efforts focused on: (1) achieving a high-thermal gradient through the specimen while enhancing the measurement accuracy of the specimen temperature, and (2) developing a model for the thermo-mechanical simulation of the HHFT. Specimens of tungsten materials that had been irradiated to low dose levels in HFIR were tested for tensile properties, micro-hardness, and microstructures. In addition, the effects of thermal annealing of neutron irradiated tungsten were examined by micro-hardness and positron annihilation spectroscopy. In preparation for the new irradiation campaigns, a set of rabbit capsules were constructed for irradiation in HFIR in FY2015 and design work for a new large HFIR-RB* capsule was initiated.

PROGRESS AND STATUS

PHENIX Task 1. High heat flux testing of W-based specimens:

In order to attain a high thermal gradient through the W/F82H specimens, new bolting holders were fabricated from Ta10W. The specimen was mounted directly onto a Cu cooling rod to attain the lowest temperature on the back surface of the specimen and enable a high thermal gradient in the specimen.

Several high-heat flux experiments were conducted as part of the PHENIX program, with the laminate samples exposed to high-heat fluxes to give a desired maximum temperature, measured with thermocouples inserted between the back surface of the specimen and top surface of the supporting Cu rod. Details and results were reported in Section 6.7 of this report.

In order to understand the deformation and residual stresses in samples tested under high-heat flux, a coupled thermal and mechanical model was developed. Inelastic properties, including hardening properties, were obtained from open literature for F82H steel and Cu materials. Thermomechanical models for the simulations of tests were implemented in the ABAQUS™ software and numerical simulation results were conducted taking into account the actual high-heat flux and high-temperature cycles. The following observations can be made with respect to the stress and deformation results:

- At high temperatures, the specimens bulge *downward* at its center, resting on the clamp at its outer edges.
- At room temperature, before clamp removal, the specimens bulged *upward* in its center.

Predicted residual stresses after cooling are higher for the 6 mm than those for the 10 mm specimens. The maximum stress was found to occur in the steel, at the steel-W interface. The maximum stress was located at the edge of the steel and within the steel for the 6 mm and 10 mm specimens, respectively.

PHENIX Task 2. Effects of neutron irradiation:

Previously, miniature tensile (Type SS-J) specimens of tungsten, primary monocrystalline materials, were tensile tested following neutron irradiation in HFIR up to ~0.1 dpa at nominally 90, 400, and 750°C. Tensile testing continued with materials up to ~1 dpa at the same three irradiation temperatures. Testing at room temperature indicated the completely brittle fracture behavior of all the irradiated materials. Irradiated tungsten tested at 300 and 500°C was ductile after low dose irradiation, but at 0.9 and 0.7 dpa, respectively, fracture behavior was brittle. Transmission electron microscopy and atom probe tomography examinations have revealed that the tungsten transmutation products of rhenium and osmium form clusters at ~0.2 dpa which transition to distinct needles and platelets by ~3 dpa at 750°C irradiation temperature.

An additional experiment was initiated in FY2014 to determine the defect annealing processes in neutron-irradiated tungsten as a function of temperature, using micro-hardness measurements and positron annihilation spectroscopy for characterization. The initial experiment demonstrated that the positron technique provides useful information on vacancies and their clusters. The work continued in FY2015 with TEM observation of defect microstructures after specific annealing steps to understand the recovery process as well as atomistic modeling of the defect behaviors. The PHENIX assignees Dr. Makoto Fukuda and Prof. Kiyohiro Yabuuchi collaborated on these experiments.

Additional irradiation vehicles were planned for this collaboration's first performance period. Two rabbits containing a few dozen circular disc specimens with 6 mm diameter and 0.5 or 1 mm thickness were irradiated at nominally 800 and 1100°C to neutron fluence of ~2×10^{25} n/m^2 (>0.1 MeV). The irradiated specimens consist of a range of materials which includes pure and single crystal tungsten, potassium doped tungsten as well as tungsten 3% rhenium alloys with potassium and lanthanum doped versions. The specimens may be utilized for thermal conductivity measurement, equibiaxial flexural testing, positron annihilation spectroscopy, hydrogen isotope retention and permeation studies, hardness determination, high heat flux testing with the plasma arc lamp, and microstructural examination.

In addition to the rabbit capsules, a full-length capsule for insertion in the HFIR RB* facility is planned. This capsule, designated RB-19J Experiment, will accommodate a large number of specimens in multiple separate temperature zones, each of which is actively temperature controlled. Most importantly, the large diameter of the RB* capsules allows use of the thermal neutron shielding material surrounding the internals, to minimize undesirable nuclear transmutation of tungsten during irradiation. In FY2014 the design work completed selection of shielding material and achieved major progress in conceptual design of the capsule. In FY2015 the design was finalized and includes three temperature zones for PHENIX collaboration materials: nominally 500, 800 and 1200°C. The samples to be included in RB-19J were fabricated, a total of approximately 1400 specimens including miniature tensile bars, miniature bend bars, and 10, 6 and 3 mm discs. Capsule assembly and insertion into HFIR is planned for early 2016.

FUTURE PLANS

All technical tasks will continue through FY2019. The ORNL will contribute to the project by providing project management, participating in personnel exchanges and workshops, and publishing and presenting the results, in addition to the continuing research jointly agreed to for FY2016.

10. MATERIALS ENGINEERING SUPPORTING THE FNSF STUDY

A.F. Rowcliffe (art.rowcliffe@gmail.com)

OBJECTIVE

The primary objective of this task is to define a framework which will enable the development of a credible roadmap for the development and performance validation of power plant-relevant materials for the Fusion Nuclear Science Facility (FNSF) in terms of radiation damage tolerance, reduced activation characteristics, operating temperature range, chemical compatibility, plasma-facing performance and component specific fabrication methods.

SUMMARY

Information on materials properties and behavior in terms of radiation damage tolerance, mechanical behavior, processing and fabrication, and coolant compatibility issues is being provided to facilitate the process of identifying potential solutions to the definitions of materials for the power core components, tritium extraction systems and for lifetime components such as the vacuum vessel, structural ring and neutron shields. Feedback to the fusion materials community is provided in terms of component-specific issues such as temperature and neutron flux gradients, coolant temperatures and transmutation rates producing helium and hydrogen. This information provides guidance for the development of materials based on design requirements.

PROGRESS AND STATUS

Evaluation of FNSF materials issues and alloy selections for power core and lifetime components was provided as input to a series of FNSF position papers:

> M. Abdou, N. Morley, S. Smolentsev, A. Ying, S. Malang, A. Rowcliffe, M. Ulrickson, "Blanket/FW Challenges and Required R&D on the Pathway to a DEMO" Fusion Engineering and Design, 100 (2015) 2–43
>
> L. El-Guebaly, S. Malang, A. Rowcliffe, L. Waganer, "Blanket/FW Materials Testing Strategy for FNSF and its Breeding Potential," Fusion Science and Technology, 68 (2015) 251-258
>
> C. Kessel, J. Blanchard, A. Davis, L. El Guebaly, N. Ghoneim, P. Humrickhouse, B. Merrill, N. Morley, G. Nelson, M. Rensink, T. Ronglien, A. Rowcliffe, S. Smolentsev, L. Snead, M. Tillack, P. Titus, L. Waganer, A. Ying, K. Young, Y. Zhai. "The Fusion Nuclear Science Facility, the Critical Step in the Pathway to Fusion Energy", Fusion Science and Technology 68 (2015) 225-236
>
> M.S. Tillack, P.W. Humrickhouse, S. Malang, A. Rowcliffe, "The Use of Water in a Fusion Power Core", Fusion Engineering and Design, 91 (2015) 52-59.

In addition, the requirements for blanket materials development to sustain the proposed ~30 year FNSF operations program were examined. Beginning with a low performance DCLL blanket, operating temperatures and neutron dose conditions are progressively advanced in a series of operational phases leading towards a blanket operating under DEMO-relevant conditions. Beginning with a front-runner structural material typified by the Code-qualified Eurofer first generation reduced activation ferritic martensitic steel (Gen-I RAFM), this scenario requires the phased development of increasingly higher performance structural materials such as the Gen-II RAFMs and oxide dispersion strengthened (nano-

structured) oxide dispersion strengthened (ODS(ns)) alloys, (Table 16). The Gen-I RAF forms the basis for the fabrication and joining technology development to support both the pre-FNSF non-fusion testing program and the construction of the first set of low-performance FNSF blankets for the first 10 years of operation (Phases 1-4); at this point, the Gen-1 blankets will approach the currently perceived lifetime neutron dose limit of ~20 dpa. Full scale programs for the advanced Gen II RAFMS and ODS (ns) alloys will need to be in place at the beginning of the ~20 years FNSF Research and Development and construction stages to facilitate insertion of test blanket modules beginning with Phase 4 operation and the deployment of higher performance blankets for Phase 5 operations. A minimum 20-year timeframe will be required to accommodate the advancement of the these materials to commercialization and code qualification, development of blanket fabrication technologies, evaluation in non-nuclear integrated testing programs, and 14 MeV neutron testing in DONES/IFMIF to validate irradiation performance.

Table 16. Evolution of DCLL Blanket Operating Conditions by FNSF Operating Phase.

Plasma	He/H	DD	DT	DT	DT	DT	DT
Phase	1	2	3	4	5	6	7
Phase time, yr	1.5	2-3	3	5	5	7	7
Peak dpa			4-7	19	26	37	37
FW/B Structure	Gen-1 RAFM	Gen-1 RAFM	Gen-1 RAFM	Gen-1 RAFM	Gen-II RAFM	Gen-II RAFM/ ODS(ns)	Gen-II RAFM/ ODS(ns)
T_{RAFM}^{max}	~350-400C	~350-400C	~385-425C	~400-450C	~450-500C	~500-550C	~500-550C
T_{LiPb}^{max}	~450C	~450C	~450C	~500C	~550C	> 600C	> 600C

Exploration of fundamental radiation effects in FM steels and ODS alloys has led to the formulation of a credible approach to developing alloys with increased radiation damage tolerance, based on creating microstructures with very high number densities of stable particle dispersions for the efficient accommodation of point defects and helium. Table 17 provides a set of suggested operating temperatures, microstructural sink strength objectives and goals for dpa and helium generation limits for the potential blanket structural materials. These will be needed to meet the proposed objectives of the phased FNSF blanket testing program.

Table 17. Suggested Temperature/Dose Performance Goals for FNSF FW/Blanket Structural Alloys.

ALLOY	OPERATING TEMPERATURE RANGE (^{O}C)	INITIAL SINK STRENGTH (m^{-2})	DAMAGE LIMIT		FNSF OPERATION	
			dpa	He (appm)	Phase	Peak dpa
Gen 1 RAFM	385-500	~3 x 10^{14}	~20	~200	1-2 3 4	<1 6 19
GEN II RAFM	385-600	~2 x 10^{15}	~50	~500	5	26
ODS (NS)	385-650	~5 x 10^{16}	~65	~650	6	37

FUTURE PLANS

Assessment of FNSF-relevant component materials issues will continue with emphasis on:

- definition of operating temperature windows for FW/B materials for each phase of FNSF operation based on more detailed analysis of thermo-mechanical loading corrosion/mass loss and neutronic conditions,
- recommendation of alloys for the structural ring based on more detailed analysis of neutron flux/spectrum, operating temperature and thermal-mechanical requirements, and
- identification of the timeframe for developing 14 MeV neutron irradiation data to address scientific proof-of-principle issues for radiation damage tolerance and engineering design for FNSF.

11. HFIR IRRADIATION PROGRAM

11.1 ARCHIVAL SAMPLES FOR THE FUSION MATERIALS COMMUNITY

Xunxiang Hu, (hux1@ornl.gov)

This project contributes to fusion materials research by testing and shipping Oak Ridge National Laboratory archival samples to other Fusion Materials community members. Four tasks are currently included.

Shipment of specimens irradiated in JP28-31 to PNNL for PIE (PNNL/UCSB-Kurtz/Odette):

The objective of the project proposed by PNNL/UCSB is to perform detailed microstructural characterization of in situ He implantation samples to answer three fundamental questions: 1) what are the basic interacting mechanisms controlling the transport of He and displacement induced defects, their fate and consequences; 2) how are the resulting cavity and other defect evolutions influenced by the starting microstructure and irradiation variables, including, displacements per atom (dpa), dpa rate, He/dpa ratio and irradiation temperature; and, 3) how can the detrimental effects of He-dpa synergisms be mitigated and managed by designing microstructures more resistant to these effects?

The PIE of neutron-irradiated Bulk Metallic Glass (BMG) and High Entropy Alloys (HEA) (UTK-Zinkle):

The key objective of this work is to examine the microstructural and mechanical property changes produced by neutron irradiation of BMG and HEA, compared to conventional alloys, providing insight into the potential of these classes of materials for high temperature fusion structural applications.

Micro-Pillar compression of neutron-irradiated W (UCLA- Ghoniem):

The objective of this project is to exam the mechanical deformation of irradiated tungsten and iron (or steel) micro-pillars using a coordinated modeling and experimental method. Compression and indentation tests require small material volumes, are relatively inexpensive for irradiated materials, and can be used as screening tests during the expensive phase of material development evaluating neutron damage effects. Discrete Dislocation Dynamics will be developed to directly compare with the experiments to provide insight into the physical mechanisms that govern plastic deformation and fracture phenomena.

He-Point defect interactions in neutron-irradiated W and Fe (UTK-Wirth):

The objective of this project is to expanding the current fundamental understanding of He-point defect/defect-cluster interactions in neutron irradiated W and Fe. Positron annihilation spectroscopy will be used to characterize the initial microstructure of as-irradiated samples, focusing on the information on vacancy clusters. This will be followed by He implantation and thermal desorption measurements. The experimental results will be compared to similar He ion implantation and thermal desorption of non-irradiated specimens. The experimental measurements will provide data to validate the multiscale models of helium-defect interactions, thermal desorption and gas bubble nucleation in the fusion neutron environment.

The current status of these projects is listed in Table 18.

Table 18. Status of Testing and Shipment of Archival Samples for FUSMAT Community (09/30/2015).

Projects	**Tasks and Progress**										
	Disassembly		**Sorting**		**Analysis & Planning**		**Packaging**		**Shipping**		
PNNL/UCSB	100%		100%		100%		15%		15%		
Shipment JP28-31 irradiated specimens to PNNL	A meeting with PNNL and UCSB colleagues was held on July 17. 10 out of the 92 specimens selected as priority. These 10 specimens have been shipped to PNNL.										
	LAMDA Delivery	**Dimensions and Mass Measurement**	**Hardness**	**Tensile Testing**	**Electrical Resistivity**	**Dynamic Young's Modulus**	**Shear Modulus**	**Nano-indentation Hardness**	**Fracture Toughness**	**TEM prep.**	**TEM**
UTK (Zinkle)	100%								50%	0%	0%
PIE of BMG* and HEA#	18 HEA and 8 BMG	100%	100%	100%	100%	100%	100%	100%	The other PIE is underway.		
* BMG-Bulk Metallic Glass; # HEA-High Entropy Alloy											
	Planning		**LAMDA Delivery**		**Cleaning**		**FIB**		**Nano-indentation**		**Disposal**
UCLA (Ghoniem)	100%		100%		50%		20%		8%		0%
Micro-pillar compression of neutron-irradiated W	Six (100) and three (110) single crystal W irradiated at various T and doses selected. Work package approved.		Samples of interest have been stored in LAMDA.		Polishing of W is being conducted.		500 nm and 1 um diameter micropillars of unirradiated W have been completed.		10-micron diameter flat XP conical diamond punch delivered. Training on nano-indentation system is being conducted.		Samples after tests will be stored in LAMDA.
	LAMDA Delivery	**Cleaning**	**PAS★**		**He Implantation**		**TDS⌘**		**Disposal**		
UTK (Wirth)	65%	20%	30%		50%		50%		5%		
He-point defect interaction in neutron-irradiated W and Fe	W samples of interest are in LAMDA.	Polishing of W is being conducted.	PAS completed on 1W05, 1W25 and unirradiated single crystal W (110). PAS annealing study of 1W05 and 1W25 at 400 to 1300°C. More PAS planned on additional irradiated samples.		Helium ion gun is being tested. The feed gas lines being modified to enable use of He-4, He-3, and D-2.		New heater working well. Temperature control stable. System helium background is high, more tests needed.		Tested samples will be stored in LAMDA.		
★PAS-Positron Annihilation Spectroscopy; ⌘TDS-Thermal Desorption Spectrometry											

11.2 HFIR IRRADIATION EXPERIMENTS

Y. Katoh (katohy@ornl.gov), J.L. McDuffee, C. Bryan, J.P. Robertson

SUMMARY

Neutron irradiation experiments were performed in support of the research and development of fusion reactor materials using various materials irradiation facilities in the High Flux Isotope Reactor (HFIR).

During Fiscal Year (FY) 2015, 11 target zone rabbit capsules completed HFIR irradiation, achieving the target neutron fluence. Those capsules are listed in Table 19 along with condensed information on material, specimen type, temperature, fluence, and period of irradiation. At the end of FY2015, 25 target zone rabbit capsules are continuing irradiation in HFIR toward their target neutron fluence. Those capsules are listed in Table 20 along with the information on materials, specimen types, and irradiation parameters. Included in these two tables are the 13 target zone rabbit capsules that started irradiation in HFIR during FY2015.

The HFIR reactor operated for six cycles in FY2015, cycles 456 to 461.

Table 19. Fusion materials program capsules that completed HFIR irradiation in FY2015. These were all target zone rabbit capsules.

Experiment Designation	Primary Materials	Specimen Types*	Irradiation Temperature (°C)	Target Fluence $x10^{25}$	Number of Reactor Cycles	HFIR Cycles Start – End		
L03046	Hi-Nicalon type s	Bend Bar	300	1000	48	409	-	456
JCR11-03	SiC/SiC	Mini bend bars	950	200	15	447	-	461
JCR11-04	SiC/SiC	Mini bend bars	950	30	15	447	-	461
JCR11-11	SiC/SiC	Mini-composites	950	30	14	448	-	461
F13A5	F82H	SSJ	300	15	9	451	-	459
F13B4	F82H	SSJ	300	15	9	451	-	459
PXW2	Tungsten	TD6	800	2	1	458	-	458
PXW5	Tungsten	TD6	1100	2	1	458	-	458
IMR1	Fe	TD1	200	2	1	460	-	460
IMR2	AIN, Si_3N_4, TiC, TiN, SiO_2	TD	200	2	1	460	-	460
IMR3	AIN, TiC, YAG, SiC, Si	MD	200	2	1	460		460

*SSJ = Tensile, TD = Thermal diffusivity disk, MD = Multipurpose disk. Some experiments also contain TEM disks, other special purpose specimens, and monitors occupying small spaces.

Table 20. HFIR fusion materials program rabbit capsules continuing irradiation beyond FY2015.

Experiment Designation	Primary Materials	Specimen Types*	Irradiation Temperature (°C)	Target Fluence $x10^{25}$	Number of Reactor Cycles	HFIR Cycles Start – End		
L03067	Hi-Nicalon type S	Bend Bar	800	50	80	405	-	484
L03068	Hi-Nicalon type S	Bend Bar	800	50	100	405	-	504
L03069	Hi-Nicalon type S	Bend Bar	800	50	100	405	-	504
L03074	Hi-Nicalon type S	Bend Bar	800	100	72	402	-	473
L03078	Morton CVD/SiC	Bend Bar	300	100	72	405	-	476
L03079	Morton CVD/SiC	Bend Bar	300	100	72	405	-	476
L03080	Morton CVD/SiC	Bend Bar	300	100	72	405	-	476
L03081	Morton CVD/SiC	Bend Bar	300	100	72	406	-	477
L03082	Morton CVD/SiC	Bend Bar	300	100	72	406	-	477
JCR11-01	SiC/SiC	Mini bend bars	950	200	25	445	-	469
JCR11-05	SiC/SiC	Mini bend bars	950	50	24	444	-	467
JCR11-07	SiC/SiC	Mini bend bars	950	100	50	444	-	493
JCR11-08	SiC/SiC	Mini bend bars	950	200	50	444	-	493
JCR11-12	SiC/SiC	Mini-composites	950	100	34	448	-	481
SCJ2-11	SiC Joint	16x6SQ-xD	500	20	10	453	-	462
F13A6	F82H	SSJ	300	30	18	451	-	468
F13B5	F82H	SSJ	300	30	18	451	-	468
SCF6	SiC/SiC	BB	600	10	6	457	-	462
SCF7	SiC/SiC	BB	600	30	14	457	-	470
SCF8	SiC/SiC	BB	600	100	45	457	-	501
SCF9	SiC/SiC	BB	600	200	90	457	-	546
SCF10	SiC/SiC	BB	950	10	5	458	-	462
SCF11	SiC/SiC	BB	950	30	14	458	-	471
SCF12	SiC/SiC	BB	950	100	45	458	-	502
IMR5	Fe	TD1	200	2	5	460	-	464

*T/SSJ = Tensile, BB = Bend Bar, Mini-comp. = Single Tow Composite, SQ-xD = Square with torsional hourglass joint, TD = Thermal diffusivity disk. Some experiments also contain TEM disks, other special purpose specimens, and monitors occupying small spaces.

11.3 DESIGN AND FABRICATION OF THE MFE-RB-19J IRRADIATION VEHICLE

J.L. McDuffee (mcduffeej@ornl.gov), J.W. Geringer

OBJECTIVE

The Department of Energy Fusion Energy Program, in collaboration with international partners PHENIX and Japan Atomic Energy Agency, is building a new materials irradiation experiment for the High Flux Isotope Reactor (HFIR) RB* position to irradiate tungsten and ferritic steel specimens in a thermal neutron-shielded environment. This experiment has been identified as the most critical mission for blanket structural materials research and will make a large contribution to the understanding of effects of irradiation on tungsten and the future direction of plasma facing component development.

SUMMARY

This experiment requires a thermal neutron shield to modify the fast/thermal neutron ratio over the life of the experiment. Previous experiments used an external Eu_2O_3 shield, but that design is no longer feasible due to both fabrication difficulties with the Eu_2O_3 inserts and HFIR management's decision not to allow the replacement of the RB* liners. Therefore, a new design has been established that uses a gadolinium metal cylinder encased between an inner aluminum sleeve and the outer experiment tube. During normal operation, differential thermal expansion will press the aluminum sleeve and gadolinium shield against the outer tube, minimizing gaps between the parts and the temperature difference across those gaps. Because HFIR missions allow only minor reductions in the reactor cycle length (nominally 25 days), the current irradiation plan for the experiment is to operate for three cycles in Fiscal Year (FY) 2016 and three cycles in FY2017, thereby splitting the "lost" days due to the presence of the neutron shield over two fiscal years.

There are four temperature zones/subcapsules in the irradiation vehicle: designed for 500°C, 1200°C, 800°C, and 250°C. The tungsten specimens occupy the three high temperature zones, and the ferritic steel specimens fill the low temperature zone. Helium gas flows serially through all four subcapsules from the top to the bottom, and then exits the inner subcapsule at the bottom of the lowest subcapsule. At that point, either argon or helium gas is inserted just below and outside the subcapsule holder for each temperature zone to modify the effective thermal conductivity of the gas gap between the subcapsule holder and the outer tube.

PROGRESS AND STATUS

Figure 84 shows the design loading of the 500°C subcapsule. All three high temperature capsules are similar in design. Figure 85 shows the design loading of the 250°C subcapsule. This low temperature subcapsule is divided into three distinct sections with different specimen types.

The original design concept called for controlling temperature with a mixture of neon and helium fill gas. However, due to a worldwide shortage, the price of neon gas has increased substantially over the past few months from about $2500 per bottle to as much as $36,000 per bottle. Even at the current price of $19,000 per bottle, the use of neon is cost-prohibitive and the design team decided to re-design using an argon-helium mixture. Figure 86 shows the overall temperature results based on an argon-helium mixture. The use of argon may require additional modifications to the design in the future to minimize personnel dose rates during operation due to argon activation in the effluent gas.

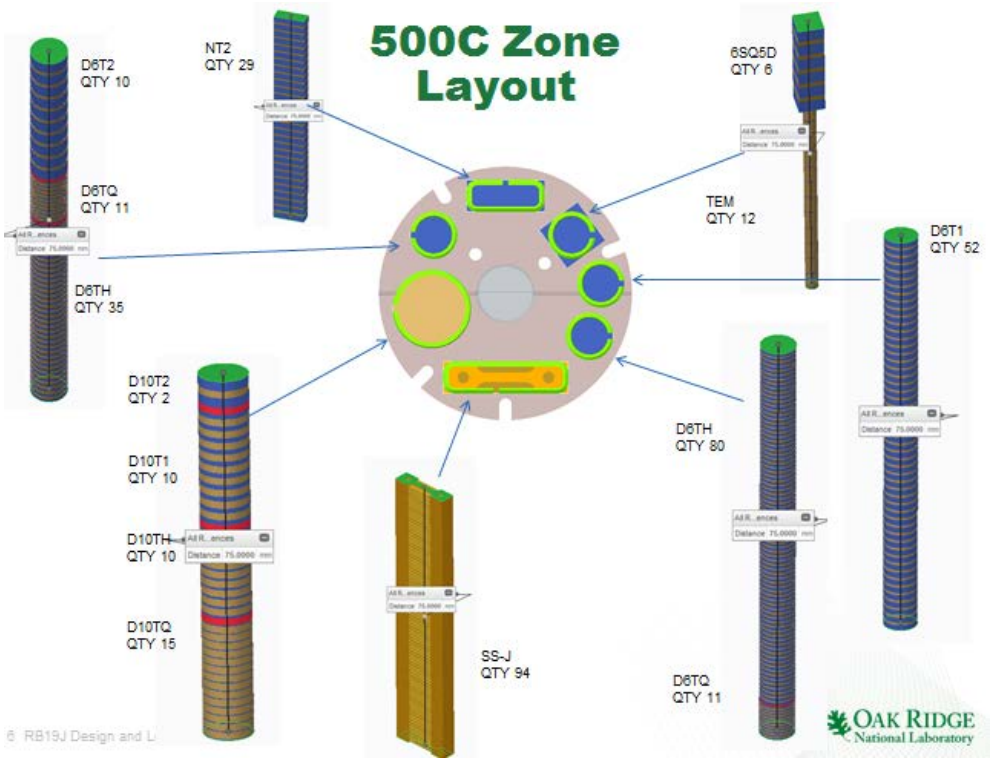

Figure 84. Specimen Design Layout for the 500°C Subcapsule. Design layouts for the 1200°C and 800°C subcapsules are similar.

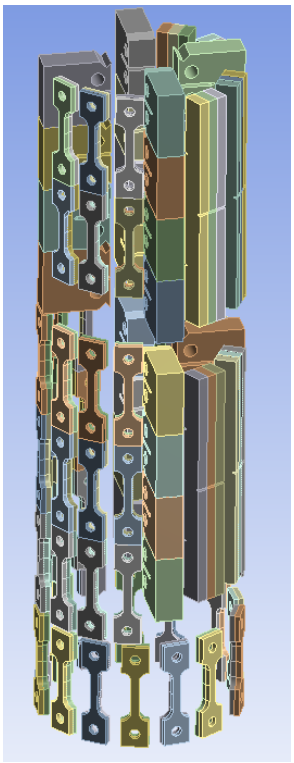

Figure 85. Specimen Design Layout for the 250°C Subcapsule.

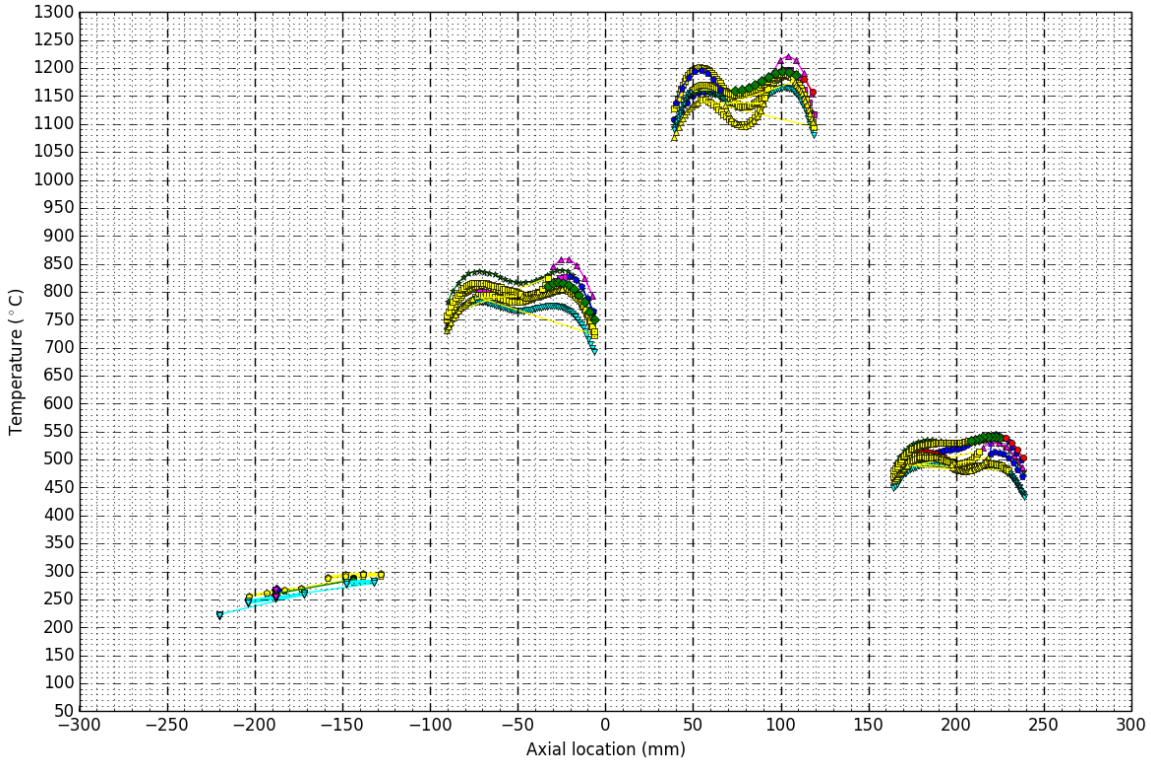

Figure 86. Current Temperature Analysis Results for the HFIR MFE-RB-19J Irradiation Capsule.

The first set of drawings, comprising the outer tube and gadolinium shield components are under technical review at HFIR and are out for quotes from fabrication shops. The initial set of drawings should be signed in October, with a second set describing the internal holders and specimens coming shortly thereafter. The design team is currently experiencing some difficulty finding a shop to agree to accept the work due to the very tight tolerances required for the shield design.

FUTURE PLANS

The FY2016 plan is to complete the design drawings, manufacture all parts, and start fabrication in winter of 2016. In order to get three cycles completed in FY2016, operations must begin in Cycle 465, which starts in March 2016. This may require that the experiment be delivered to HFIR as early as February 2016.

11.4 NEW HFIR RABBIT CAPSULE CAMPAIGNS

C. M. Petrie (petriecm@ornl.gov), J. L. McDuffee, R. H. Howard, and T. Toyama (Tohoku Univ.)

OBJECTIVE

Three High Flux Isotope Reactor (HFIR) irradiation experiments on materials with potential for fusion applications are currently underway. The Bulk Metallic Glass (BMG) (e.g. $Zr_{52.5}Cu_{17.9}Ni_{14.6}Al_{10}Ti_5$) are being considered for nuclear applications due to their possible radiation tolerance resulting from their amorphous structure. Similarly, High Entropy Alloys (HEAs) (e.g. $Fe_{27}Ni_{28}Mn_{27}Cr_{18}$) have attracted increased attention for their potential self-healing capabilities during irradiation due to severe lattice distortions and atomic-level stress in these alloys. The Institute for Materials Research (IMR) of Tohoku University in Japan is collaborating with Oak Ridge National Laboratory to characterize the irradiation tolerance of advanced ceramics. The objective of these irradiation experiments is to irradiate BMG, HEA, and various IMR ceramic materials in the HFIR at high temperatures in order to experimentally determine the radiation resistance of these materials and their potential suitability for use in fusion applications.

SUMMARY

The HFIR rabbit irradiation capsules have been designed to achieve the desired specimen temperatures for the BMG, HEA, and IMR irradiation campaigns. The BMG specimens in the form of bend bars, Charpy bars, and TEM discs will be irradiated up to 0.1 dpa in a hydraulic tube facility in the HFIR at a temperature of 200°C. The HEA tensile specimens and TEM discs will be irradiated up to 1 dpa in the hydraulic tube facility at 500°C. The collaborative program with IMR has irradiated 4 rabbits containing iron, quartz, single crystal silicon, Si_3N_4, AlN, TiC, TiN, YAG, and SiC specimens in the form of discs (for various characterizations such as strength, thermal properties, electrical properties, etc.) at 200°C for up to 10 dpa. An additional seven capsules containing some of these IMR materials as well as TiB_2, ZrB_2, glassy carbon, and MAX phase Ti_3SiC_2, Ti_3AlC_2, and Ti_2AlC specimens will be irradiated at temperatures of 200, 600, and 1000°C for doses ranging from 2 to 10 dpa. All capsule designs are complete and the capsules will be fabricated and delivered to the HFIR in Fiscal Year (FY) 2016.

PROGRESS AND STATUS

Each capsule design includes technically reviewed assembly and detail drawings as well as approved safety calculations to ensure that the capsules cannot fail under worst case reactor conditions. Approved drawings have been signed and issued for all capsules. Capsule parts have been fabricated to the appropriate drawings for the BMG and HEA capsules. For the seven remaining IMR capsules, all parts have been fabricated except for the specimen holders, which are currently being fabricated. Approved safety calculations exist for the BMG and HEA capsules and a draft calculation is in the final stage of review for the remaining IMR capsules.

In addition to thermal safety calculations, independently reviewed design and analysis calculations have been completed for all experiments to predict capsule component temperatures during normal operating conditions. Figure 87 shows temperature contours for the BMG Charpy bars (outside specimens), bend bars (inside specimens), and TEM discs (top discs), the HEA tensile specimens and TEM discs, and the IMR disc specimens. These design temperatures will be validated using peak irradiation temperatures determined from post-irradiation dilatometry measurements of silicon carbide temperature monitors.

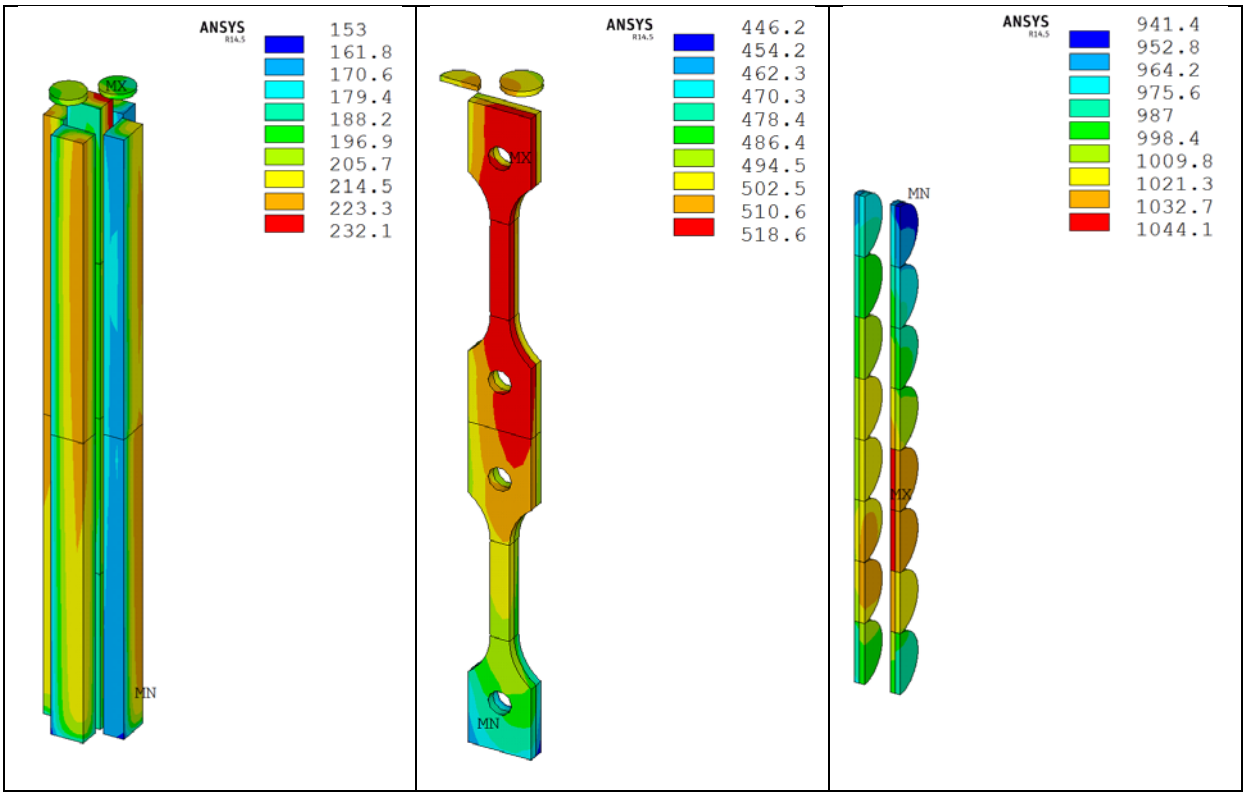

Figure 87. Predicted specimen temperature contours for the 200°C BMG rabbit (left), 500°C HEA rabbit (center, with ½-symmetry), and 1000°C IMR rabbit (right, with ½-symmetry).

FUTURE PLANS

In FY2016, the BMG, HEA, and seven remaining IMR capsules will be assembled, welded, and tested using non-destructive evaluation (i.e. hydrostatic pressurization and helium leak testing) before being delivered with appropriate quality assurance documentation to the HFIR for reactor insertion. Most irradiations will be completed in FY2016 except for some longer duration (five cycles, or ~10 dpa) rabbits that will complete irradiation in early FY2017.

12. NEW AND UPGRADED TESTING CAPABILITIES IN LAMDA AND IMET

K.G. Field (fieldkg@ornl.gov), P.D. Edmondson, C.M. Parish, K. Linton, X. Hu

SUMMARY

The Oak Ridge National Laboratory (ORNL) is home to two main facilities, the Low Activation Materials Development and Analysis (LAMDA) facility and the Irradiated Materials Examination and Testing (IMET) hot-cell facility, for performing systematic studies of the effects of neutron and/or ion irradiation on candidate materials for fusion and fission reactor applications. Typical post-irradiation examination activities utilize both the IMET and LAMDA facility to conduct mechanical and physical property measurements and microstructural characterization. The unique set of capabilities in these facilities is shared by the Fusion Materials Program and other programs and is a keystone capability for irradiated materials research at ORNL. The equipment and capabilities are upgraded or added to keep these facilities at the forefront of irradiated materials research; the following briefly highlights Fiscal Year 2015 activities of this continuous improvement effort.

LAMDA - LOW ACTIVATION MATERIALS DEVELOPMENT AND ANALYSIS FACILITY

The LAMDA facility was established for materials science evaluation of irradiated materials that have low radiological threat (<100 mR/hr at 30 cm). The facility is multipurpose, with an area for possible radiological contamination work (otherwise known as the C-zone) and an area for "clean work" or work to be conducted on samples with limited to no threat of removable radioactive contamination. Both of these zones allow work without the need for remote manipulation, which greatly expands the range of studies that can be conducted. The C-zone is home to much of the mechanical testing equipment, including load frames and micro-hardness testers, as well as physical and thermo-physical analysis equipment. These include differential scanning calorimeters and Thermogravimetric Analysis units. Advanced optical and electron microscopy systems are housed within the clean zone; these have seen significant recent upgrades and installation of new, state-of-the-art equipment to facilitate high-end, science based investigations of irradiated material.

The most significant upgrade in the C-zone component of LAMDA is the installation of a Positron Annihilation Spectroscopy (PAS), which is a powerful tool to characterize the vacancy defects in materials, thus expanding the microstructure characterization capability for fusion materials research. In parallel to the PAS installation, a thermal desorption system coupled with an in situ 20 keV ion gun has been constructed and is being calibrated and tested in LAMDA. The thermal desorption system is dedicated to investigating the gas-defect behavior in plasma facing materials and structural materials used in fusion reactors. More details about these two systems can be found in Section 6.4 of this report.

Several improvements have been made for preparation of electron microscopy samples including the installation of a Fischione 1020 Plasma Cleaner and a Fischione 1040 Nano-Mill. The plasma cleaner has been certified for radiological use and provides cleaning of TEM and scanning electron microscopy (SEM) samples. This prevents or eliminates artifacts induced during sample preparation. The Fischione 1040 Nano-Mill is a low-energy Ar ion mill that enables the gentle polishing of focused-ion beam (FIB) samples prepared from one of LAMDA's three operational FEI dual beam FIBs. The FIB sample preparation for TEM is known to have the potential to induce damage and artifacts in the sample; the Nano-Mill can remove a significant portion of these defects, enhancing the accuracy of TEM-based investigations of irradiated materials.

The LAMDA's FEI Versa 3D dual beam SEM FIB, shown in Figure 88, has been recently upgraded with analytical equipment to provide detailed microstructural investigations including grain orientation and phase analysis. An Oxford 150 mm^2 X-Max^N Electron Dispersive Spectrometry (EDS) Si drift detector (SDD) has been installed to allow chemical detection during SEM based investigations. In parallel to this installation, an Oxford NordlysMax^2 electron backscatter diffraction (EBSD) detector and corresponding support systems have been installed. The SEM-based EBSD allows grain orientation, morphology and local grain misorientation (among many other properties) to be determined. Coupling EBSD and EDS with the SEM-FIB capabilities of the FEI Versa enables selective manufacture of samples from site-specific-regions such as specific grain orientations or phases for transmission electron based microscopy investigations.

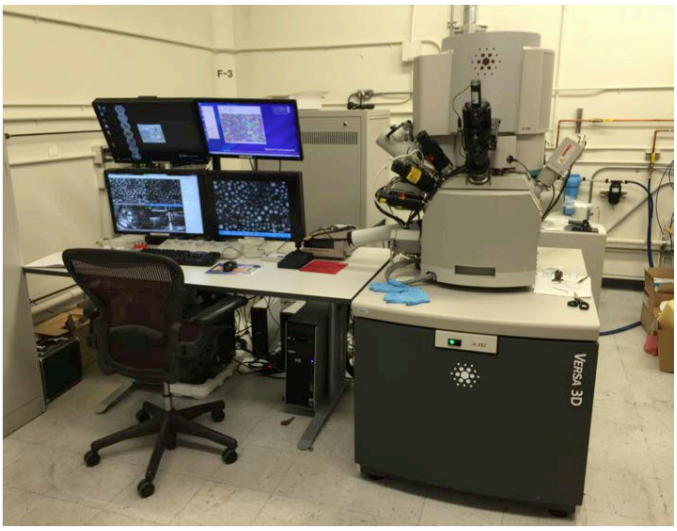

Figure 88. The FEI Versa 3D FIB-SEM with new EBSD system in LAMDA.

The most recent, and most significant, increase in capabilities in LAMDA is the FEI "Talos" F200X scanning transmission electron microscope (STEM). The F200X is an advanced analytical STEM optimized for high-speed, high-sensitivity, high-resolution elemental analysis. This is achieved by coupling a high-brightness field-emission cathode with stable, high-resolution electron optics and a large-area, four-sector EDS-SDD detector, providing the best analytical performance in a commercially available system. The instrument is shown in Figure 89, and an example of atomic-resolution X-ray mapping capability in Figure 90 (region in a neutron-irradiated high-temperature superconductor). The instrument is intended primarily for the analysis of neutron-irradiated specimens but will also be used for non-radiological sample analysis including ion irradiated specimens.

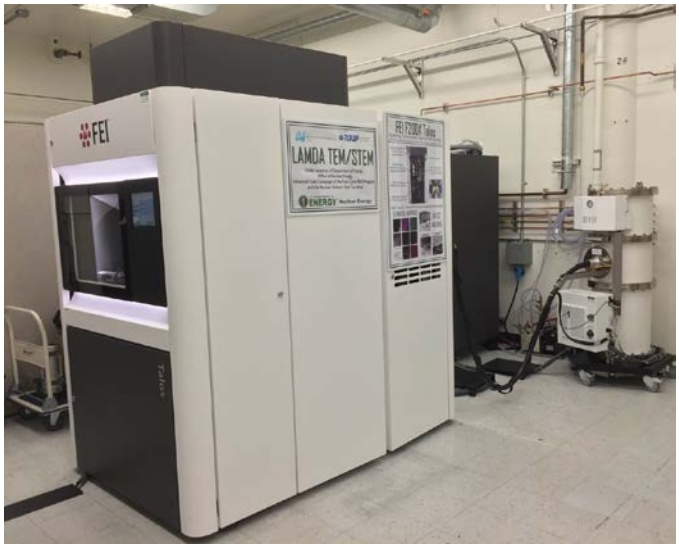

Figure 89. The FEI "Talos" F200X S/TEM installed and operational in LAMDA.

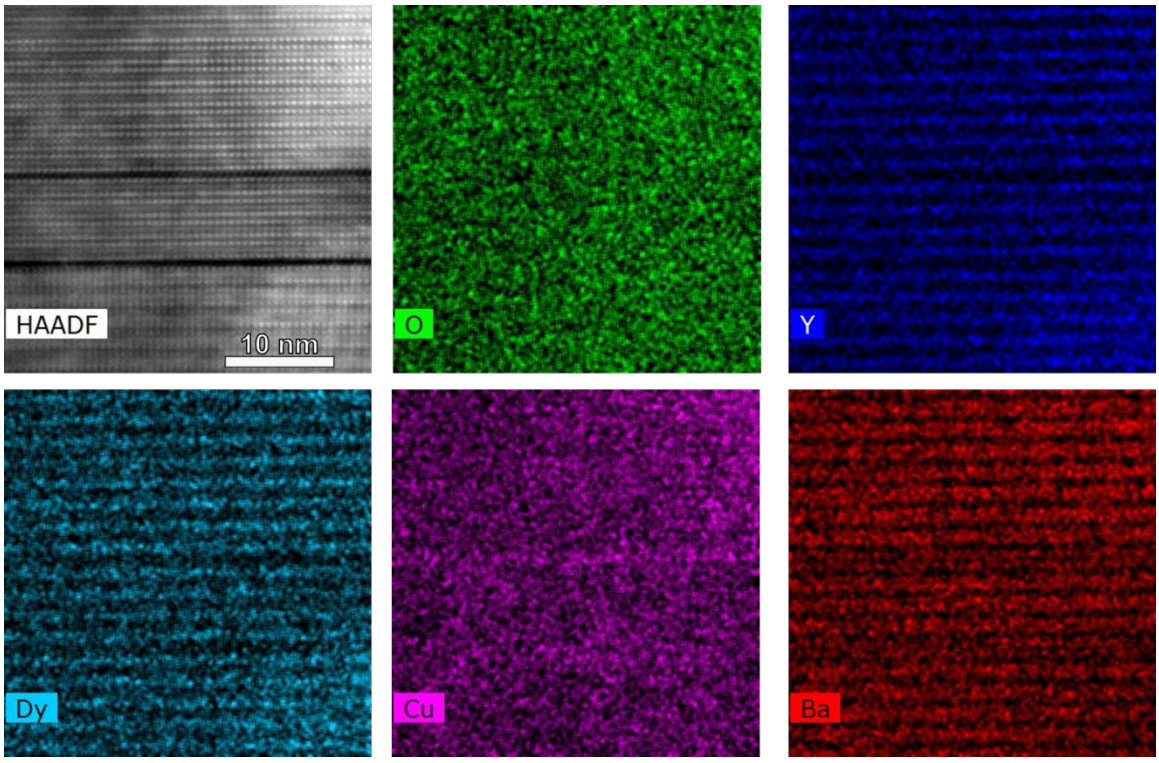

Figure 90. Elemental maps at atomic resolution in neutron-irradiated high-temperature superconductor taken on the new FEI "Talos" F200X i in LAMDA. HAADF: High-angle annular dark-field image mode.

IMET - IRRADIATED MATERIALS EXAMINATION AND TESTING LABORATORY

The IMET is the facility used for materials science evaluations of irradiated materials with high radiological threat. This Class III nuclear facility includes a series of hot cells with remote manipulation. An example image of one of these cells in use is shown in Figure 91. The hot cells at IMET contain the primary mechanical testing and examination equipment for highly irradiated structural alloys and ceramics. The six interconnected steel-lined hot cells contain 320 square feet of workspace and are maintained for low alpha contamination to allow transfer of specimens to other radiological laboratories, such as LAMDA, after testing or sorting. Functions that can be performed include capsule disassembly, laser profilometry, optical microscopic examination, grinding, polishing, welding, shearing, machining, sawing, photography, and video examination. Mechanical systems are available for tensile, creep, Charpy impact, fracture toughness, and fatigue testing.

Figure 91. HFIR irradiation capsule disassembly by remote manipulation in the IMET Hot Cells in ORNL Building 3025E.

The increasing need for high temperature mechanical testing has led to the procurement of a specialized load frame and furnace assembly for installation in the IMET facility. Purchase orders were placed in FY2015 for a new high temperature, high vacuum test frame to be installed in FY2016. The Instron Model 5967 Electromechanical Test Frame with a 30 kN load capacity was delivered to Oxy-Gon Industries, Inc. in August of 2015. Oxy-Gon will design, manufacture, and mount a custom vacuum furnace on the Instron frame for delivery and insertion in Cell 1 of IMET. The vacuum furnace will provide a maximum temperature of 1200°C, ultimate vacuum of $1x10^{-7}$ Torr, and the capability of mechanical testing in an inert environment. Multiple specimen viewports will provide sightlines for an optical extensometer, allowing detailed mechanical testing such as the use of digital image correlation techniques. Samples tested using this new system then can be transferred to LAMDA for microstructural investigations to establish structure-property relationships for irradiated materials.

13. PUBLICATION AND PRESENTATION RECORD

13.1 PAPERS PUBLISHED IN FY2015

(*Alphabetical by first ORNL author*)

Y. Katoh, "Radiation Effects," chapter in book *Ceramic Matrix Composites: Materials, Modeling and Technology*. N. P. Bansal and J. Lamon, published by Wiley: 389-404. (2014)

Yutai Katoh, Takashi Nozawa, Chunghao Shih, Kazumi Ozawa, Takaaki Koyanagi, Wally Porter, Lance L. Snead, "High-dose neutron irradiation of Hi-Nicalon Type S silicon carbide composites. Part 2: Mechanical and physical properties", *Journal of Nuclear Materials*, 462 (2015) 450-457

C.H. Henager, B.N. Nguyen, R.J. Kurtz, T.J. Roosendaal, B.A. Borlaug, M. Ferraris, A. Ventrella, Y. Katoh, "Modeling and Testing Miniature Torsion Specimens for SiC Joining Development for Fusion." *Journal of Nuclear Materials* 466 (2015) 253-268

Y.N. Osetsky and R.E. Stoller, "Atomic-scale Mechanisms of Helium Bubble Hardening in Iron", *Journal of Nuclear Materials*, 465 (2015) 448-454

Alejandro G. Perez-Bergquist, Takashi Nozawa, Chunghao Shih, Keith J. Leonard, Lance L. Snead, Yutai Katoh, "High dose neutron irradiation of Hi-Nicalon Type S silicon carbide composites, Part 1: Microstructural evaluations", *Journal of Nuclear Materials* 462 (2015) 443-449

B.A. Pint, S. Dryepondt, K. A. Unocic and D. T. Hoelzer, "Development of ODS FeCrAl for Compatibility in Fusion and Fission Applications," *JOM* 66 (2014) 2458-2466

M. Abdou, N. Morley, S. Smolentsev, A. Ying, S. Malang, A. Rowcliffe, M. Ulrickson, "Blanket/FW Challenges and Required R&D on the Pathway to a DEMO" *Fusion Engineering and Design*, 100 (2015) 2–43

L. El-Guebaly, S. Malang, A. Rowcliffe, L. Waganer, "Blanket/FW Materials Testing Strategy for FNSF and its Breeding Potential," *Fusion Science and Technology*, 68 (2015) 251-258

C. Kessel, J. Blanchard, A. Davis, L. El Guebaly, N. Ghoneim, P. Humrickhouse, B. Merrill, N. Morley, G. Nelson, M. Rensink, T. Ronglien, A. Rowcliffe, S. Smolentsev, L. Snead, M. Tillack, P. Titus, L. Waganer, A. Ying, K. Young, Y. Zhai. "The Fusion Nuclear Science Facility, the Critical Step in the Pathway to Fusion Energy", *Fusion Science and Technology* 68 (2015) 225-236

M.S. Tillack, P.W. Humrickhouse, S. Malang, A. Rowcliffe, "The Use of Water in a Fusion Power Core", *Fusion Engineering and Design*, 91 (2015) 52-59

A.S. Sabau, E.K. Ohriner, J.O. Kiggans, D.C. Harper, L.L. Snead, and C.R. Schaich, "Facility for high heat flux testing of irradiated fusion materials and components using infrared plasma arc lamps," *Physica Scripta*, T159, 014007 (4pp), doi:10.1088/0031-8949/2014/T159/01400, 2014

A.S. Sabau, E.K. Ohriner, J.O. Kiggans, C.R. Schaich, Y. Ueda, D.C. Harper, Y. Katoh, and L.L. Snead, "High-Heat Flux Testing of Irradiated Tungsten based Materials for Fusion Applications using Infrared Plasma Arc Lamps," *Fusion Science and Technology*, 66 (2014) 394-404

G.D. Samolyuk, Y.N. Osetsky, R.E. Stoller, “Molecular dynamics modeling of atomic displacement cascades in 3C-SiC: Comparison of interatomic potentials”, Journal *of Nuclear Materials* 465 (2015) 83-88

T. Hirose, T, Nozawa, R.E. Stoller, D. Hamaguchi, H. Sakasegawa, H. Tanigawa, M. Enoeda, Y. Katoh, L.L. Snead, "Physical properties of F82H for fusion blanket design," *Fusion Engineering and Design* 89 (2014) 1595-1599

K. A. Unocic, D. T. Hoelzer and B. A. Pint, “The Microstructure and Environmental Resistance of Low-Cr ODS FeCrAl,” *Materials at High Temperature*, 32 (2015) 123-132

X. Yu, B. Mazumder, M. K. Miller, S. A. David, and Z. Feng, “Stability of Y–Ti–O Precipitates in Friction Stir Welded Nanostructured Ferritic Alloys”, *Science and Technology of Welding and Joining* 20 (2015) 236-241

13.2 GRADUATE THESES SUCCESSFULLY DEFENDED

D.W. Clark, "Ion Irradiation Characterization Studies of MAX Phase Ceramics", MS thesis, Department of Nuclear Engineering, University of Tennessee, July 2015

13.3 PAPERS SUBMITTED IN FY 2015

(Currently Awaiting Publication)

C. Ang, et al., "Anisotropic swelling and microcracking of neutron irradiated Ti_3AlC_2-$Ti_5Al_2C_3$ materials", submitted to *Scripta Materialia*

Anne A. Campbell, Wallace D. Porter, Yutai Katoh, Lance L. Snead, "Method for Analyzing Passive Silicon Carbide Thermometry with a Continuous Dilatometer to Determine Irradiation Temperature" Submitted to *Journal of Nuclear Technology*

L.M. Garrison and G.L. Kulcinski. "The Effects of Tungsten's Pre-Irradiation Surface Condition on Helium-Irradiated Morphology." Submitted to *Journal of Nuclear Materials,* April, 2015

L.M. Garrison, G.L. Kulcinski, and H.M. Meyer III. "The Response of ZrB_2 to Simulated Plasma-Facing Material Conditions of He Irradiation at High Temperature." Submitted to *Journal of Nuclear Materials*, May, 2015

D. T. Hoelzer, K.A. Unocic and D. Shin, "Development of ODS FeCrAl Ferritic Alloys for Fusion Reactor Applications: Comparison of Computational and Experimental Studies," submitted to *Journal of Materials Science*

N.A.P. Kiran Kumar, K.J. Leonard, G.E. Jellison and L.L. Snead, "High Dose Neutron Irradiation Performance of Dielectric Mirrors," submitted to *Fusion Science and Technology*

Takaaki Koyanagi, James O. Kiggans, Chad M. Parish, Chinthaka M. Silva, Yutai Katoh, "Silicon Carbide Joints Formed by Pressureless Transient Eutectic-Phase Process ", submitted to *Journal of the American Ceramics Society*

A.A. Gapud, N.T. Greenwood, J.A. Alexander, A. Khan, K.J. Leonard, T. Aytug, F.A. List, M.W. Rupich and Y. Zhang, "Irradiation response of commercial, high-Tc superconducting tapes: electromagnetic transport properties", accepted for publication in *Journal of Nuclear Materials*

Y.N. Osetsky and R.E. Stoller, "Atomic-scale Mechanisms of Helium Bubble Hardening in Iron," submitted to *Journal of Nuclear Material*

13.4 PRESENTATIONS IN FY2015

(*Only includes OFES-funded ORNL Presenting Authors*)

Presentations at NuMat 2014 – the Nuclear Materials Conference, October 27-30, 2014, Clearwater Beach, FL

D. T. Hoelzer, K.A. Unocic and B. A. Pint, "*Development of ODS FeCrAl Ferritic Alloys for Fusion Reactor Applications*"

Yutai Katoh, Chunghao Shih, Chad Parish, Lance Snead, Steve Zinkle, Takeshi Toyama (Tohoku U.), Tatsuo Shikama (Tohoku U.), "*Effects of Neutron Irradiation on Commercial MAX-phase Ceramics*"

L. Tan, K.G. Field, L.L. Snead, G.S. Was (U. Michigan), "*Stability of MX precipitates in ferritic alloys under Fe2+ ion and neutron irradiations*"

Presentations at the 21st Topical Meeting on Technology of Fusion Energy (TOFE), American Nuclear Society, 9-13 Nov., 2014, Anaheim, CA

C.H. Charry, S.I. Abdel-Khalik, M. Yoda, A.S. Sabau, and L.L. Snead, "*Evaluation of Cooling Conditions for a High Heat Flux Testing Facility based on Plasma-Arc Lamps*"

L. Garrison and G. Kulcinski (U. Wisconsin), "*Tungsten Exposed to Multiple Energy Helium Implantation*"

Y. Katoh, L.L. Snead, C. Parish, L.M. Garrison, S.J. Zinkle, T. Shikama (Tohoku U.), "*Promises and Challenges for High Temperature Ceramics and Composites as Fusion In-vessel Component Materials*"

N.A.P. Kiran Kumar, K.J. Leonard, G.E. Jellison and L.L. Snead, "*Effects of Neutron Irradiation on Microstructures and Optical Performance of Multi-layered Dielectric Mirror*"

A.S. Sabau, K. Tokunaga, J.O. Kiggans, C.R. Schaich, E.K. Ohriner, D.C. Harper, Y. Ueda, , and L.L. Snead, *"High-heat flux Facility for High-Throughput Screening of Irradiated Materials for Fusion Applications using Infrared Plasma Arc Lamps"*

A.S. Sabau, K. Tokunaga, Y. Ueda, L.L. Snead, and Y. Katoh, *"Thermo-mechanical Effects during High-Heat Flux Testing of Plasma Facing Material Specimens using Infrared Plasma Arc Lamps"*

L. Snead, L. Garrison, T.S. Byun, M. Rieth (KIT), "*Irradiation Effects in Tungsten and Implications for Design Application beyond ITER*"

Presentations at the 39th International Conference and Expo on Advanced Ceramics and Composites, Daytona Beach, FL, January 25-30, 2015

T. Koyanagi, J.O. Kiggans, Y. Katoh, "*Silicon Carbide Joints Formed by Pressureless Transient Eutectic-Phase Process*"

Y. Katoh, T. Koyanagi, J.O. Kiggans, "*Evaluating Ceramic Joints in Annular Geometries: Preliminary Test Design and Analysis*"

C. H. Henager, B. Nguyen, R. Kurtz, T. Roosendaal, B. Borlaugz, M. Ferraris, A. Ventrella, Y. Katoh, "*Joining SiC for Nuclear Applications: Modeling Miniature Torsion Tests with Experimental Validation*"

S. T. Gonczy, Y. Katoh, M. Ferraris, "*The ASTM C28 Test Standard for the Torsional Shear Strength of Adhesive Bonds for Advanced Ceramics*"

Y. Katoh, T. Koyanagi, L. L. Snead, T. Hinoki, "*Irradiation Creep of Silicon Carbide in Medium-to-High Dose Regime*"

M. G. Jenkins, S. T. Gonczy, Y. Katoh, "*Composition, Structure, Manufacture, and Properties of SiC-SiC CMCS for Nuclear Applications: ASME BPVC Section III*"

Y. Katoh, L. L. Snead, C. H. Henager, "*Silicon Carbide Composite Research in U.S. Fusion Materials Program*"

Presentations at TMS2015 – 144th Annual Meeting and Exhibition (March 15-19, Orlando, FL)

J. Brechtl, A.G. Perez-Bergquist, H. Bei, N.A.P. Kiran Kumar and S.J. Zinkle, "*Neutron and Ion Irradiation of Zr52.5Cu17.9Ni14.6Al10Ti5 Bulk Metallic Glass*"

D.W. Clark, S.J. Zinkle, C.M. Parish, D. Tallman, N.A.P. Kiran Kumar, C. Li, "*Ion Irradiation Characterization Studies of MAX Phase Ceramics*" This received the *Best Oral Paper* award for this symposium

C. Li, N.A.P. Kiran Kumar, H. Bei, M.C. Troparevsky, B.D. Wirth, G.M. Stocks and S.J. Zinkle, "*Evaluation of Radiation Effects in FeMnNiCr High Entropy Alloy*"

Y. Osetskiy and R. Stoller "*Strengthening Mechanisms Due to Hard Obstacles in Ferritic Alloys*"

S. J. Pawel, "*Fundamentals of Liquid Metal Corrosion and Techniques for Assessment of Compatibility*"

W. Tang, G. Chen, J. Chen, X. Yu, D. A. Frederick, Z. Feng, "*Heat Input and Post Weld Heat Treatment Effects on RAFM Steel Friction Stir Welds*"

Other Presentations

L. Garrison and G. Kulcinski (U. Wisconsin) "*The Impact of Pre-Irradiation Surface Roughness on Helium-Irradiated Morphology of Tungsten*" presented at Materials Science and Technology Conference. October 13, 2014. Pittsburgh, PA

Roger E. Stoller, "*Possibilities for Radiation Damage Resistance: Perspectives from Atomistic and Mesoscale Modeling*", presented at the 24th International Toki Conference: Expanding Horizons of Plasma and Fusion Science though Cross-Fertilization, November 2-4, 2014, Toki-City, JAPAN

Y. Osetskiy and R. Stoller, "*Strengthening Mechanisms Due to Inclusion Obstacles in Ferritic Alloys*" Presented at the MRS Spring Meeting, San Francisco, May 2015

L.M. Garrison, L.L. Snead, N.A.P. Kiran Kumar, T.S. Byun, M.R. McAlister, and W.D. Lewis. "*Mechanical Properties of Neutron-Irradiated Tungsten*" Oral presentation at 15th International Conference on Plasma-Facing Materials and Components for Fusion Applications, Aix-en-Provence, France, 18-22 May 2015

A.S. Sabau, K. Tokunaga, J.O. Kiggans, J.J. Henry, S. Gorti, E.K. Ohriner, C.R. Schaich, D.C. Harper, and L.L. Snead, "*Residual Stresses during High Heat Flux Testing of Tungsten Coated Steel using Plasma-Arc Lamps*." Poster presentation at 15th International Conference on Plasma-Facing Materials and Components for Fusion Applications, Aix-en-Provence, France, 18-22 May 2015

Xunxiang Hu, "*Multiscale Investigation of Gas Behavior in Structural Materials in Fusion and Fission Energy Environments: A Combined Experimental and Modeling Approach*." Presented at:

- Southwestern Institute of Physics, Chengdu, China, June 18, 2015
- University of Science and Technology of China, Hefei, China, June 23, 2015
- Institute of Plasma Physics, Chinese Academy of Science, Hefei, China, June 24, 2015
- University of Science and Technology of Beijing, Beijing, China, June 26, 2015

T. Koyanagi, J.O. Kiggans, J.M. Pryor, Y. Katoh, "*Specimen Size Effect on Torsional Shear Strength of SiC Hourglass Joints*." Presented at the 11th International Conference on Ceramic Materials and Components for Energy and Environmental Applications (CMCEE-11), Vancouver, Canada, June 14-19, 2015

Y. Katoh, T. Koyanagi, L. Snead, T. Hinoki, C. H. Henager, M. Ferraris, H. E. Khalifa, C. A. Lewinsohn, S. Grasso, "*Effects of Neutron Irradiation on Ceramic Joints for Silicon Carbide-Based Nuclear Structures and Fuels*." Presented at the 11th International Conference on Ceramic Materials and Components for Energy and Environmental Applications (CMCEE-11), Vancouver, Canada, June 14-19, 2015

C. M. Parish, N. A. P. Kiran Kumar, L. L. Snead, P. D. Edmondson, K. G. Field, C. Silva, A. M. Williams, K. Linton, and K. J. Leonard, "*LAMDA: Irradiated-Materials Microscopy at Oak Ridge National Laboratory*," Presented at Microscopy and Microanalysis 2015, Portland, OR, August 4, 2015

Chad M. Parish, "*Under the microscope: what insight can the newest analytical tools yield about radiation effects in materials?*" Seminar at University of California, San Diego, September 24, 2015

Chad M. Parish, "*An overview of fusion structural materials and PMI-materials work at Oak Ridge National Laboratory*", Seminar at General Atomics, DIII-D, September 25 2015